TOWARD A QUANTITATIVE UNDERSTANDING OF THE SHAPE-CONTROLLED SYNTHESIS OF COLLOIDAL NOBLE-METAL NANOCRYSTALS

A Dissertation
Presented to
The Academic Faculty

by

Hsin-Chieh Peng

In Partial Fulfillment
of the Requirements for the Degree
of Doctor of Philosophy in the
School of Chemistry and Biochemistry

Georgia Institute of Technology
December, 2015

TOWARD A QUANTITATIVE UNDERSTANDING OF THE SHAPE-CONTROLLED SYNTHESIS OF COLLOIDAL NOBLE-METAL NANOCRYSTALS

Approved by:

Dr. Younan Xia, Advisor
Department of Biomedical Engineering
Georgia Institute of Technology

Dr. Angus P. Wilkinson
School of Chemistry and Biochemistry
Georgia Institute of Technology

Dr. Joseph P. Sadighi
School of Chemistry and Biochemistry
Georgia Institute of Technology

Dr. Z. John Zhang
School of Chemistry and Biochemistry
Georgia Institute of Technology

Dr. Christopher W. Jones
School of Chemical and Biomolecular Engineering
Georgia Institute of Technology

Date Approved: October 19, 2015

Dedicated to my loving parents for their love, endless support, and encouragement.

ACKNOWLEDGEMENT

Although only my name appears on the cover of this dissertation, a great many people have contributed to its production. My doctoral dissertation research is dedicated to all those people who have inspired me, interacted, collaborated, and shared with me personally and professionally. It is because of them, my graduate school experience has been so positive that I will cherish forever. First and foremost, I would like to express my deepest gratitude to my advisor, Professor Younan Xia, who has guided me throughout my thesis work with his patience, enthusiasm, and knowledge. He provided insightful discussion and stimulated my critical thinking, as well as greatly improved my scientific writing skills. I would also like to extend my gratitude to Professors Christopher Jones, Joseph Sadighi, Angus Wilkinson, and John Zhang, for serving on my dissertation committee. Thank you for being supportive during my journey toward a PhD degree.

My grateful thanks go to Dr. Shuifen Xie, who generously shared many useful hands-on experiences when I was new to the group. I appreciate the input of Professor Jingyue Liu, who performed HRTEM for some of my projects. I am grateful for the support brought by many people at Georgia Tech: Professor Dong Qin, Dr. Lei Zhang, Dr. Xiaohu Xia, Dr. Dehui Wan, Jinho Park, Dr. Sang-Il Choi, Dr. Cun Zhu, Dr. Yi Wang, Aleksey Ruditskiy, and Walter Henderson, who have helped me immensely and made my dissertation work possible. Friends outside of chemistry have never failed to provide support and encouragement, along with many fun and delightful interactions. Special thanks go to Shih-Yu Huang for patiently tutoring me on the programming language.

Although this dissertation is dedicated to them, they are worth mentioning again: My sincerest thanks to my parents, Wu-Shun Peng and Wen-Chen Liu, for their boundless faith in me and unconditional support. At last, I would like to thank my wife, Wei-Ting Huang, and my son, Liam, for making my life meaningful.

TABLE OF CONTENTS

LIST OF TABLES

LIST OF FIGURES

Page

LIST OF SYMBOLS AND ABBREVIATIONS

AA	ascorbic acid
CA	citric acid
ccp	cubic-close packing
D	diffusion coefficient
DEG	diethylene glycol
DFT	density functional theory
E_a	activation energy
E_{diff}	potential energy barrier to diffusion
EG	ethylene glycol
ε	bond strength
fcc	face-centered cubic
f_{dep}	deposition probability
f_{des}	desorption probability
f_{dif}	diffusion probability
γ	specific surface free energy

h_i	the distance to the center for the i^{th} facet
HAADF	high-angle annular dark-field
HCHO	Formaldehyde
HCl	hydrochloric acid
hcp	hexagonal close packing
HRTEM	high-resolution transmission electron microscopy
ICP-MS	inductively-coupled plasma mass spectroscopy
KBr	potassium bromide
KCl	potassium chloride
KI	potassium iodide
LSPR	localized surface plasmon resonance
N	total number of drops added into the solution
NaBr	sodium bromide
Na_2PdCl_4	sodium tetrachloropalladate(II)
N_B	the number of broken bonds per surface unit cell
n_0	the number of the precursor ions in each drop
n_{low}	the lower limit of a steady state

n_t	instantaneous number of the precursor ions
n_{up}	the upper limit of a steady state
ORR	oxygen reduction reaction
PVP	poly(vinyl pyrrolidone)
R	ideal gas constant
r_0	initial reduction rate
ρ_A	the number of surface atoms per unit area
RNA	ribonucleic acid
SERS	surface-enhanced Raman scattering
STM	scanning tunneling microscopy
TEG	triethylene glycol
TEM	transmission electron microscopy
τ	the duration of time between adjacent drops
UV-vis	ultraviolet-visible
$V_{deposition}$	atom deposition rate
$V_{diffusion}$	surface diffusion rate
XPS	X-ray photoelectron spectroscopy

SUMMARY

Colloidal nanocrystals are of critical importance to a variety of fundamental studies and technological applications. The shape of a nanocrystal determines not only its physicochemical properties but also its relevance for a given application. This dissertation is focused on the development of a quantitative analysis of the thermodynamic and kinetic factors responsible for the mechanisms and pathways during the nucleation and growth of noble-metal nanocrystals. With the chemisorption of Br^- ions on Pd{100} facets as an example, I demonstrate the capability of quantitatively analyzing the coverage density of this capping agent using a combination of inductively coupled plasma mass spectrometry and X-ray photoelectron spectroscopy. I further apply the collision model that has long been established in surface science to seed-mediated growth of cubic seeds with or without chemisorbed Br^- ions on their side facets in an effort to account for the deposition probability of atoms on the surface of a seed and thus its growth pattern in the presence or absence of surface capping. In a third project, with the polyol synthesis of Pd nanocrystals as an example, I demonstrate that the kinetic parameters, including rate constant and activation energy of a reaction can be derived from spectroscopic measurement and then used to calculate the initial reduction rate and further confirm that this parameter can be a quantitative knob for controlling the internal structure of a nanocrystal. Finally, the symmetry breaking phenomenon involved in the seed-mediated growth of Pd nanocrystals was investigated by quantitatively correlating the growth modes (symmetric *vs.* asymmetric) with the reaction kinetics simulated based on experimental parameters. The quantitative understanding achieved in this dissertation lays the foundation for the rational design and deterministic synthesis of nanocrystals with desired and controlled structures, shapes, and related properties.

CHAPTER 1

INTRODUCTION

1.1 Colloidal Noble-Metal Nanocrystals

Noble metals are central to the development of modern science and technology. Many of them have already found extensive use in applications that range from catalysis [1−4] to electronics [5−8], photonics [9−12], information storage [13−15], energy conversion/storage [16−18], environmental protection [19, 20], and medicine [21−24]. Most of these applications require the use of metals in a finely divided state, preferably in the form of nanocrystals with at least one dimension in the range of 1−100 nm. Although controlling the geometric shape taken by a metal nanocrystal may initially seem like a scientific curiosity, its implication goes far beyond aesthetic appeal. The shape not only controls its physicochemical properties but also determines its relevance and merit for the aforementioned applications [25−27].

A fascinating example can be found in localized surface plasmon resonance (LSPR) [28−31], an optical phenomenon arising from the collective oscillation of free electrons in a nanocrystal made of a metal such as Au or Ag in response to the oscillating electric field of the incident light. Under resonance, the incident light can be effectively absorbed and converted to photons (scattering, at the same frequency but into all different directions) or phonons (absorption or photothermal conversion, to excite the vibrational modes of the crystal lattice). The number of resonance peaks, their wavelengths, and the ratio between scattering and absorption cross sections are all dependent on the geometric shape of the nanocrystal because this particular parameter determines how the polarization of free electrons occurs and how the charges are distributed on the surface. For Au nanospheres of 50 nm in diameter, the LSPR is dominated by a strong peak at ~525 nm, giving their aqueous suspension (equivalent to the conventional Au colloids) a

striking ruby red color as the green light is largely absorbed by the nanospheres and non-radioactively converted into heat [32]. For Au nanorods with dimensions of 10×50 nm^2 (width×length), on the other hand, there are two LSPR peaks. The peak associated with the oscillation of free electrons along the short axis is positioned at ~540 nm while the mode along the long axis is peaked at ~825 nm, giving their aqueous suspension a light brown color [33−35]. In addition to LSPR, the merit of Au or Ag nanocrystals for many other applications, including surface-enhanced Raman scattering (SERS) and surface-enhanced fluorescence, can be greatly augmented by achieving a tight control over their geometric shapes [36−38].

Heterogeneous catalysis is another interesting example. It has been established that many reactions on catalysts based on metal nanocrystals are highly sensitive, in terms of activity and/or selectivity, to the arrangement (or, more precisely, the coordination number) of atoms and thus the type of facet on the surface, which is determined by the geometric shape of the nanocrystals [39−41]. It has been reported that the hydrogenation of benzene catalyzed by 13-nm Pt cuboctahedrons covered by a mix of {111} and {100} facets generated both cyclohexane and cyclohexene, whereas only cyclohexene was produced on 13-nm Pt cubes encased by {100} facets [42]. For the oxygen reduction reaction (ORR), the catalytic activity of 6-nm Pd cubes covered by {100} facets was found to be one order of magnitude higher than that of 6-nm Pd octahedrons covered by {111} facets [43]. In the case of Pt_3Ni alloy, the ORR activity of {111} facets on octahedral nanocrystals could be more than 50 times higher than the {100} facets on cubic counterparts [44]. Similar correlations between the catalytic activity/selectivity and the geometric shape (or more directly, the type of facet exposed on the surface) of nanocrystals have also been observed in many other systems [45−47].

These and many other examples clearly illustrate the critical importance of shape control to the effective use of noble-metal nanocrystals in a wide variety of applications. Thanks to the tremendous efforts from many research groups, the past decade has

witnessed spectacular success in developing a myriad of methods for shape-controlled syntheses of colloidal metal nanocrystals [48, 49]. Metal nanocrystals with many distinctive shapes can now be readily prepared, with notable examples including one-dimensional (2-D) nanocrystals such as thin plates or prisms with triangular, hexagonal, or circular projections; 1-D nanocrystals such as rods, bars, and wires with circular, square, rectangular or pentagonal cross sections; as well as 0-D nanocrystals such as spheres, spheroids, cubes, cuboctahedrons, octahedrons, tetrahedrons, rhombic dodecahedrons, bipyramids, decahedrons, and icosahedrons. In addition, nanocrystals with concave surfaces, facets of high Miller index (containing indices > 1), or branched arms have also become increasingly common in recent years [50−52].

1.2 Shape-Controlled Synthesis of Colloidal Noble-Metal Nanocrystals

The formation of colloidal metal nanocrystals in a solution phase can be divided into three major steps [48]: *i*) nucleation or formation of small clusters from metal atoms and ions; *ii*) evolution of the nuclei into seeds with well-defined internal structures; and *iii*) growth of the seeds into nanocrystals with distinctive shapes. The outcome is determined by a set of thermodynamic (*e.g.*, redox potential and surface capping) and kinetic (*e.g.*, concentration, mass transport, temperature, and the involvement of foreign species) parameters that are intimately and intricately entangled to each other. When considering a synthesis of nanocrystals as a chemical reaction, the atoms derived from a precursor can be viewed as reactants while the nanocrystals with different shapes being products. From this perspective, the nanocrystals having the lowest Gibbs free energy will be the thermodynamic products and are expected to dominate in a synthesis. However, despite being unfavorable by thermodynamics, nanocrystals with shapes deviating from the thermodynamic product could still be trapped in a less stable state as the kinetic products if the reaction has a lower activation energy barrier relative to that for the thermodynamic products. As such, the thermodynamic or kinetic products are expected to be in

dominance when the synthesis is conducted under thermodynamic or kinetic control, respectively. According to the Arrhenius equation, the most effective way to reduce the impact of activation energy on reaction rate is to raise the reaction temperature [53]. As a result, temperature plays the most important role in determining whether thermodynamic or kinetic control is in dominance.

1.2.1 Thermodynamic Control

The essence of thermodynamic control is to give a system an adequately long period of time so that all the atoms can reach their final destinations to attain the global minimum for the Gibbs free energy of the entire system. This can be accomplished by aging the sample for a long period of time, raising the temperature of a system to increase the mobility of atoms on the surface, or both. The shape obtained under thermodynamic control can be considered as an *equilibrium state* defined by a set of experimental parameters, including temperature, pressure, and surrounding environment. As such, whenever there is a perturbation to any one of these parameters, the state and thus the shape will be altered accordingly.

A nanocrystal will take its equilibrium shape when its total Gibbs free energy reaches the global minimum [54]. As shown in Eq. (1.1), the total Gibbs free energy of a nanocrystal can be expressed as the sum of Gibbs free energy for the bulk and the excess Gibbs free energy caused by the surface:

$$dG = dG_{bulk} + \gamma\, dA \tag{1.1}$$

where γ denotes the specific surface free energy (per unit area) and A is the surface area. At a fixed volume, the total Gibbs free energy will reach the minimum value under the condition of a minimized total surface free energy:

$$\int \gamma_i \, d\, A_i = minimum \tag{1.2}$$

where the integral is taken over the entire surface of a nanocrystal. This equation implies that a nanocrystal should take an equilibrium shape when its total surface free energy is minimized. If the specific surface free energy does not depend on the direction, as in an isotropic system like a noncrystalline material (a liquid or an amorphous solid), the total surface free energy is solely proportional to the total surface area. In this case, the total surface free energy will be minimized when the "nanocrystal" (or more appropriately, nanoparticle because of the amorphous structure in this case) takes a spherical shape to minimize the total surface area at a fixed volume. For a crystalline material, however, the surface free energies of different crystallographic planes tend to differ from each other because of the intrinsic anisotropy in atomic arrangement. As a result, one has to know the specific surface free energies of different crystallographic planes in order to derive the equilibrium shape of a nanocrystal in a vacuum.

The specific surface free energy is defined as the increase in free energy per unit area when a new surface is created. When atoms are tightly bound to each other, the bonds between them need to be broken in order to create a pair of new surfaces. In a sense, the surface free energy reflects the cost in energy when bonds are broken and is thus determined by the number and strength of bonds involved. Specifically, under the *broken bond approximation* where only interactions between the nearest neighbors are considered, the specific surface free energy of a crystallographic plane can be calculated using the following equation:

$$\gamma = \frac{1}{2} N_B \varepsilon \rho_A \tag{1.3}$$

where N_B is the number of broken bonds per surface unit cell (or per surface atom), ε is the bond strength, ρ_A is the number of surface atoms per unit area, and the factor ½ is added because each bond involves two atoms [55]. Both N_B and ρ_A can be derived from the crystal structure. Figure 1.1 schematically illustrates the models of three principal low-index planes, including (111), (100), and (110), of a face-centered cubic (*fcc*) metal with a lattice constant of a_0. The dashed box in each model represents the corresponding unit cell for the surface atoms. From these models, the values of ρ_A are calculated as $2.31(1/a_0^2)$, $2(1/a_0^2)$, and $1.41(1/a_0^2)$ for the (111), (100), and (110) planes, respectively. In addition, the number of broken bonds per surface unit cell can be easily derived as 3 and 4 for the (111) and (100) planes, respectively. In the case of (110) plane, it should be noted that one additional broken bond from the sub-surface (labeled as *a'b'*) needs to be included because it is also involved in the formation of two (110)-type surfaces. Consequently, the number of broken bonds per surface unit cell is 6 instead of 5 for the (110) plane.

Once N_B and ρ_A have been determined, the specific surface free energies of these low-index planes can be calculated as $\gamma_{(111)}=3.46(\varepsilon/a_0^2)$, $\gamma_{(100)}=4(\varepsilon/a_0^2)$, and $\gamma_{(110)}=4.24(\varepsilon/a_0^2)$. These results indicate that the surface free energies of the low-index planes of an *fcc* metal increase in the order of $\gamma_{(111)}<\gamma_{(100)}<\gamma_{(110)}$. These results also imply that for an *fcc* metal, the anisotropy ratio between the surface energies of an arbitrary crystallographic plane and the (111) plane should be the same regardless of its elemental composition. The *broken bond approximation* offers a simple method for estimating the surface free energies of a metal nanocrystal surrounded by vacuum. However, the exclusion of some other factors such as the interactions with the second and the third nearest neighbors and the relaxation of surface could potentially lead to significant errors in calculating the surface free energies of different types of crystallographic planes, especially for those with high indices [56]. Alternatively, computational modeling based on the density

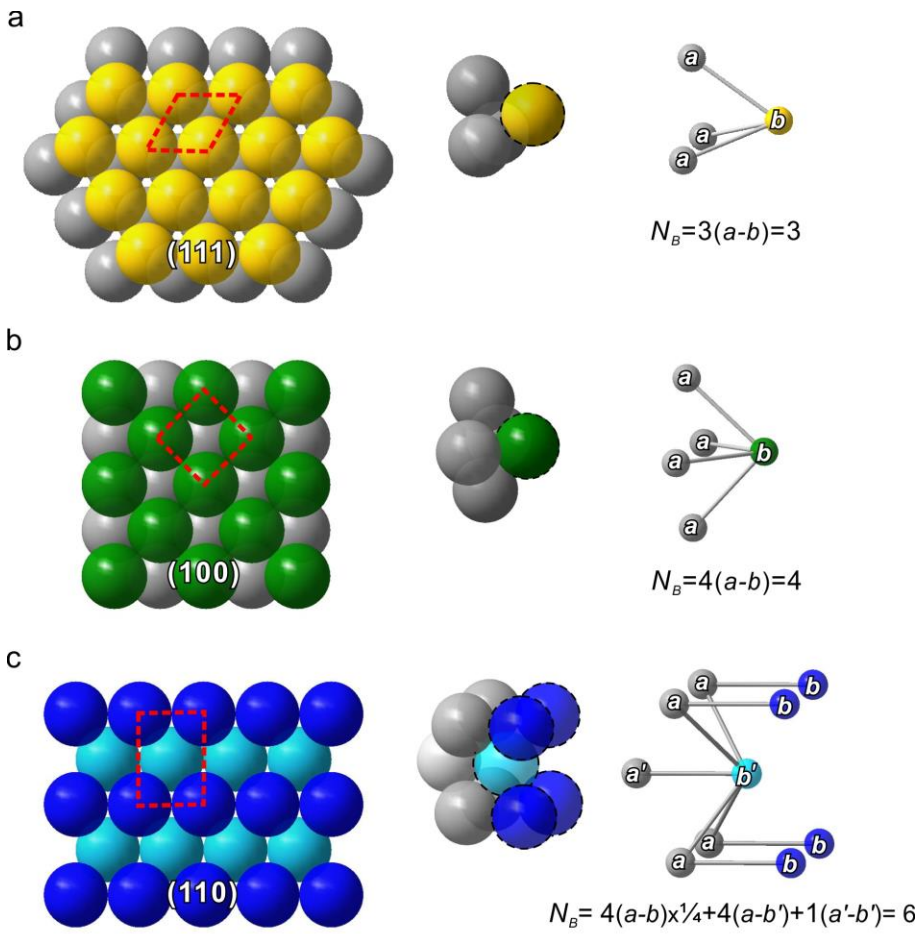

Figure 1.1. Models of the three major low-index planes of a face-center-cubic metal and the corresponding numbers (N_B) of bonds per surface unit cell that have to be broken in creating a pair of new surfaces: (a) (111), (b) (100), and (c) (110). The red dashed box represents the surface unit cell for each crystallographic plane. (Reprinted with permission from [101]. Copyright 2015 American Chemical Society.)

functional theory (DFT) offers a more accurate approach to the calculation of surface free energies [57, 58]. It was shown that the ratio between the surface energies of an arbitrary plane and the (111) plane can indeed differ slightly between different metals.

For a metal nanocrystal, its equilibrium shape cannot be spherical because many high-index facets with relatively high specific surface free energies would be required for the formation of a perfect sphere. When considering a nanocrystal made of an *fcc* metal and situated in a vacuum, one would expect an octahedral or tetrahedral shape so that only {111} facets with the lowest specific surface free energy will be exposed on the surface. Both octahedron and tetrahedron, however, have larger surface area-to-volume ratios when compared with a cube enclosed by {100} facets. In an effort to minimize the total surface free energy, a "hybrid" shape enclosed by a mix of {100} and {111} facets in the right proportion eventually becomes the winner favored by thermodynamics.

Theoretically, the equilibrium shape of a nanocrystal in a vacuum can be derived using the Wulff construction [59]. The basic principle is shown in Eq. (1.4),

$$\frac{\gamma_i}{h_i} = constant \tag{1.4}$$

where γ_i and h_i are the specific surface free energy and the distance to the center for the i^{th} facet, respectively. This equation indicates that the distance of the facet from the center of the crystal is proportional to the specific surface free energy of a given facet. Following this theorem, the Wulff construction begins with a polar plot of the specific surface free energies as a function of orientation, where the length of each radius vector is proportional to its specific surface free energy. Next, a line perpendicular to each vector is drawn at the intersection point with the polar plot, as represented by the short-dashed lines in Figure 1.2a. Repeating the procedure for all different directions represented by the crystal axes eventually results in a closed polyhedron inside the polar plot, which

represents the equilibrium shape of the nanocrystal. In principle, one can always predict the equilibrium shape (*i.e.*, the so-called Wulff shape) of a metal once the specific surface free energies of different crystallographic planes become available either theoretically [57, 58] or experimentally [60−62].

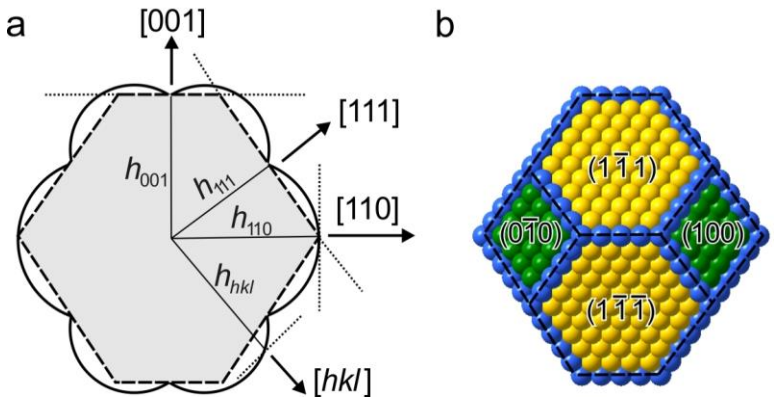

Figure 1.2. (a) The two-dimensional section of a polar plot of the specific surface free energies of an *fcc* crystal oriented along $[1\bar{1}0]$ as derived from the Wulff thereom. The inner envelope denoted by dashed lines corresponds to the equilibrium shape of the nanocrystal. (b) A three-dimensional atomic model corresponding to the equilibrium shape shown in (a). (Reprinted with permission from [101]. Copyright 2015 American Chemical Society.)

Figure 1.2a shows a 2D polar plot of the specific surface free energy and the corresponding equilibrium shape of an *fcc* nanocrystal viewed along $[1\bar{1}0]$. In the 3D space, this equilibrium shape corresponds to a truncated octahedron, with only {100} and {111} facets on the surface. Based on the *broken bond approximation* for an *fcc* metal, its {111} facets are lower in specific surface free energy than its {100} facets, with a ratio of $\gamma_{(100)}$ to $\gamma_{(111)}$ being 1.16. As a result, it is anticipated that the {111} facets will take a

slightly larger proportion than the {100} facets according to the Wulff theorem. Taken together, the equilibrium shape of a nanocrystal made of an *fcc* metal and surround by a vacuum should be a truncated octahedron (Figure 1.2b), where the ratio between the areas of {100} and {111} facets can vary slightly depending on the metal.

When a single-crystal seed made of an *fcc* metal is allowed to grow in a vacuum and truly under thermodynamic control, it should evolve into a truncated octahedron with increasingly larger sizes, as confined by the Wulff theorem. Since the equilibrium shape of a nanocrystal is determined by the relative magnitudes of specific surface free energies associated with different crystallographic facets, it is feasible to alter the ratios between the specific surface free energies to obtain nanocrystals with shapes other than the one predicted using the Wulff theorem. How to manipulate the relative specific surface free energies associated with different crystallographic planes has been a central theme in engineering the shape of metal nanocrystals formed under thermodynamic control. Among the various approaches in this endeavor, surface adsorption of chemical species (atomic, ionic, molecular, or macromolecular) from a gas or solution phase seems to be the simplest and most versatile.

In heterogeneous catalysis, it has been documented by many reports that the gas molecules can chemisorb onto the surface of a nanocrystal *via* covalent bonding and thus effectively reduce the specific surface free energy [63−66]. Due to the involvement of covalent bonding, the adsorbate can preferentially bind only to a specific type of facet on the surface and thus alter the ratios between the specific surface free energies of different facets, leading to the formation of nanocrystals with profiles deviated from the Wulff shape predicted for the same system in a vacuum.

In a study reported in 1985, for example, Pt nanocrystals supported on an amorphous SiO_2 substrate were found to change shape when the sample was annealed at 600 °C in the presence of different gas molecules (Figure 1.3, a and b) [67]. The shapes observed for the Pt nanocrystals were truncated cuboctahedrons and cubes when the samples were

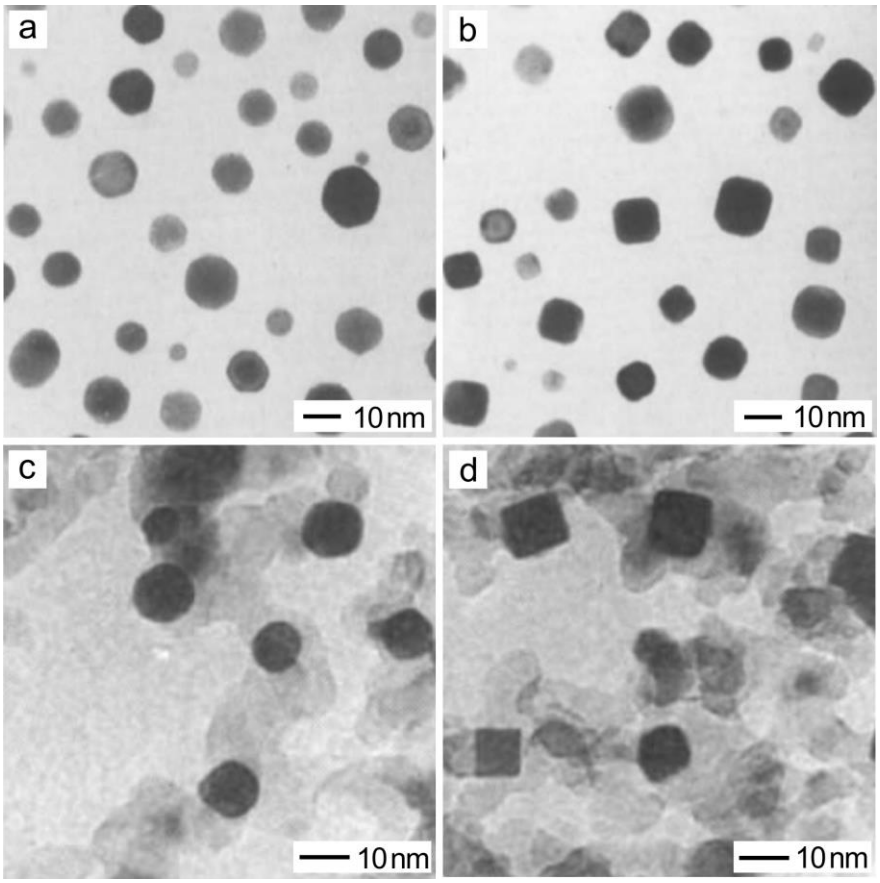

Figure 1.3. The transformations between Pt nanocrystals with distinct shapes when they were thermally annealed under different gas atmospheres. (a, b) TEM images of Pt nanocrystals supported on planar amorphous SiO_2 after annealing under (a) N_2 and (b) H_2 at 600 °C for 24 h. (Adapted with permission from [67]. Copyright 1985 Elsevier B. V.) (c, d) TEM images of Pt nanocrystals supported on Al_2O_3 powders after annealing (c) in air at 700 °C for 1 h, and (d) under H_2 containing a trace amount of H_2S at 500 °C for 16 h. (Adapted with permission from [69]. Copyright 1986 Nature Publishing Groups.)

annealed in N_2 and H_2, respectively. Interestingly, the Pt nanocrystals could be reversibly switched between these two shapes by alternating the gas under which the sample was thermally annealed. Even though the exact mechanism for the shape transformation was not clear at that time, this study demonstrated the feasibility of controlling the shape of a metal nanocrystal by exposing the sample to an appropriate gas. At an elevated temperature, the migration of atoms on the surface would be greatly accelerated, allowing the nanocrystal to quickly attain the distinct shape defined by a new set of thermodynamic parameters [68].

A similar observation was reported in 1986 for Pt nanocrystals supported on Al_2O_3 powders when the sample was subjected to thermal annealing under different gaseous environments [69]. As shown in Figure 1.3, c and d, annealing the nanocrystals in air led to a nearly spherical shape, whereas a cubic shape was obtained in a H_2 atmosphere containing a trace amount of H_2S. If the interaction between the gas molecules and Pt surface is relatively weak, as in the case of air where only physisorption was involved, the relative surface energies for different types of facets of a nanocrystal are more or less equivalent to the case of vacuum. As such, it is understandable that the nanocrystal would take a nearly spherical shape similar to what is predicted using the Wulff theorem. In contrast, the presence of sulfur species would induce the formation of a cubic shape, which can be attributed to the sulfur poisoning mechanism commonly observed for noble-metal catalysts [70]. In this case, the preferential binding of sulfur to Pt(100) could effectively lower its specific surface free energy to reverse the order of relative specific surface free energies between $\gamma_{(100)}$ and $\gamma_{(111)}$. In maximizing the expression of the facet favored by thermodynamics, the Pt nanocrystals were transformed into a cubic shape enclosed by six {100} facets as long as there was an adequate amount of H_2S in the gaseous environment.

Taken together, the above two examples demonstrated that the shape of a metal nanocrystal supported on a solid substrate can be altered in a controllable fashion by

introducing a gaseous species capable of covalently binding to a specific type of facet. The chemisorption will lower the specific surface free energy of that facet and thereby alter the ratios between the areas occupied by different types of facets on the surface of a nanocrystal. Despite these successful demonstrations, the use of a high temperature and a solid support, as well as the limited choices of gases, may greatly limit the potential application of such a gas-phase method for engineering the shape of metal nanocrystals. When switching to a solution-phase method, there would be no such limitation due to the availability of many different capping agents for each type of facet.

Capping agents are ionic species, small molecules, or macromolecules that can selectively bind to different types of facets on a nanocrystal to alter their specific surface free energies and thus their proportions in terms of area [71−74]. When a capping agent is introduced into a reaction solution, the type of facet stabilized by the capping agent will exhibit a lower specific surface free energy, leading to the formation of nanocrystals with a shape that maximizes the expression of that type of facet. In addition to the Wulff theorem, the shape taken by a growing nanocrystal can also be understood from a kinetic perspective based on the relative growth rates of different crystallographic planes. Since the capping agent chemisorbed on a facet will hinder or prevent the deposition of atoms onto this facet, surface capping will eventually lead to the formation of a shape with that particular facet preferentially expressed. In other words, the facet covered by the capping agent will take a slower growth rate and thus a greater proportion on the surface. Taking the growth of a truncated octahedral seed as an example, Figure 1.4 compares the pathways of shape evolution in the presence of two complementary capping agents. With the introduction a capping agent for the {100} facets, the order of surface free energies will become $\gamma_{\{100\}} < \gamma_{\{111\}}$ and thereby the growth will be faster along the <111> directions than along the <100> directions. Owing to the difference in growth rate, the ratio between the areas of {100} and {111} facets on the surface will gradually increase, and the nanocrystal will evolve from truncated octahedron to cuboctahedron, truncated

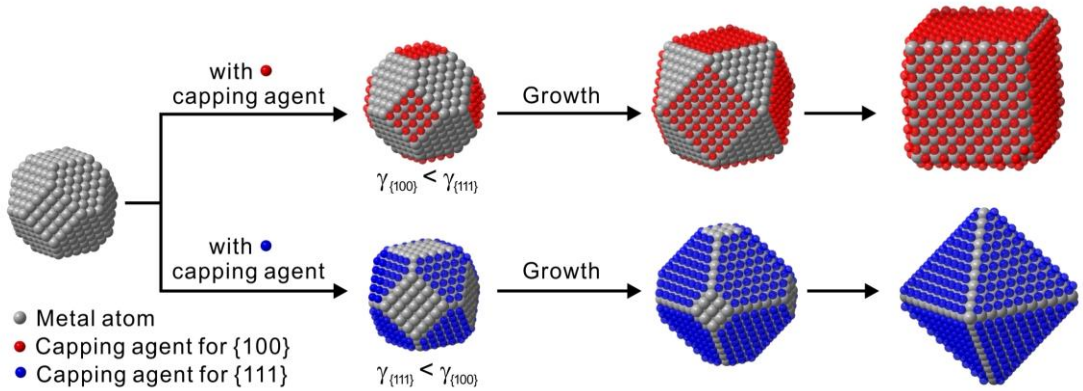

Figure 1.4. Schematic illustrations showing the role of capping agents in directing the growth of a single-crystal seed made of an *fcc* metal. The shape of resultant nanocrystals can be manipulated in a controllable fashion through the introduction of a capping agent (represented by red or blue dots) that can selectively bind to a specific type of facet, altering the order of surface free energies and eventually leading to the formation of a nanocube enclosed by {100} facets and an octahedron enclosed by {111} facets, respectively. (Reprinted with permission from [101]. Copyright 2015 American Chemical Society.)

cube, and eventually a cube enclosed by {100} facets only. In contrast, the specific surface free energy of {111} facets will be further lowered in the presence of a capping agent for the {111} facets. The faster growth rate along the <100> directions will keep reducing the proportion of {100} facets during growth, eventually leading to the formation of an octahedron enclosed by {111} facets only.

Thanks to the availability of a rich variety of chemicals that can act as capping agents for different types of surfaces, solution-phase synthesis provides a powerful route to the preparation of metal nanocrystals with a myriad of shapes. Generally, the preferential binding of a capping agent to a specific metal surface may be attributed to many factors, including the crystal and surface structures of the metal, as well as the functional group(s) of the capping agent. An integration of experimental studies and computational approach based on DFT and *ab initio* calculations will offer a powerful and irreplaceable approach

to revealing the role played by a capping agent in carving out the shape of a nanocrystal at an atomic/molecular level, as well as to the identification of capping agent(s) for generating a specific type of metal surface. In principle, such a thermodynamic control, as enabled by the introduction of a capping agent to selectively bind to a specific type of metal surface, allows people to effectively manipulate the order of specific surface free energies and ultimately obtain colloidal nanocrystals with well-controlled shapes or facets.

Taken together, thermodynamic control in solution phase is a simple and yet effective strategy that can be easily implemented during a synthesis. As a result, it has been widely explored for the shape-controlled synthesis of colloidal metal nanocrystals. A thermodynamically controlled synthesis can be implemented in two slightly different ways: *i*) introducing different types of capping agents to selectively chemisorb onto different types of metal surfaces and thus lower the specific surface free energies of these facets and *ii*) controlling the coverage density of a capping agent by adjusting its concentration in the reaction solution to manipulate its power in lowering the specific surface free energy of a facet. Thanks to the efforts from many research groups, a variety of capping agents have been identified over the past decade for the shape-controlled synthesis of colloidal metal nanocrystals. To this end, poly(vinyl pyrrolidone) (PVP) and citrate have been recognized, respectively, as the capping agent for Ag(100) and Ag(111) surfaces [75]; I^- ions have been established as an effective capping agent for Pd(100) and Au(111) surfaces [76, 77]; and CO has been demonstrated with selectivity toward Pt(100) and Pd(111) surfaces [78, 79]. In addition, some biological molecules/macromolecules such as peptides and RNAs have been shown with a capability of selectively binding to different types of metal surfaces and thereby induce the formation of metal nanocrystals with different shapes [80−82]. Most significantly, the biomolecules can be rationally designed with different functional groups to selectively bind to specific metal surfaces, synthesized, and then employed as capping agents. Through the use of some existing

analytic tools, it is even feasible to measure and compare the binding affinities between the biomolecules and various metal surfaces [81, 82].

1.2.2 Kinetic Control

As driven by thermodynamics, the atoms initially added to a specific region on the surface of a nanocrystal (typically, the most active site with the highest surface free energy) should migrate to the site lowest in surface free energy. In many cases, however, the surface diffusion is not adequate so the nanocrystal will be trapped in a thermodynamically less favorable shape, leading to the formation of a kinetic product. To this end, the exact shape (or morphology) displayed by the nanocrystal will be determined by the relative magnitudes of the rates corresponding to atom deposition ($V_{\text{deposition}}$) and surface diffusion ($V_{\text{diffusion}}$). Both of them are kinetic parameters and can be manipulated by varying experimental conditions related to chemical kinetics.

Taking the growth of a cubic seed (with all of its six side faces being completely covered by a capping agent) as an example, the newly formed atoms should be deposited onto the corners owing to the high energy of these sites (Figure 1.5). Upon deposition, the adatoms can have two different options: staying at the corner sites where deposition occurs or migrating to different sites (*e.g.*, edges and side faces) through surface diffusion. The growth pathway of this cubic seed and thereby the shape taken by the product have a strong dependence on the ratio between the rates for atom deposition and surface diffusion (*i.e.*, $V_{\text{deposition}}/V_{\text{diffusion}}$). When $V_{\text{deposition}}/V_{\text{diffusion}} << 1$, most of the adatoms at the corners will migrate to edges and side faces and the growth will prevail along the <100> and <110> directions, leading to the formation of cuboctahedrons favored by thermodynamics (Figure 1.5a). When $V_{\text{deposition}}/V_{\text{diffusion}} >> 1$, on the contrary, surface diffusion can be ignored and the growth will be switched to the <111> directions, promoting the formation of a kinetically favored octapod as the product (Figure 1.5d). Similar arguments can also be applied to the situations where the ratios of $V_{\text{deposition}}$ to

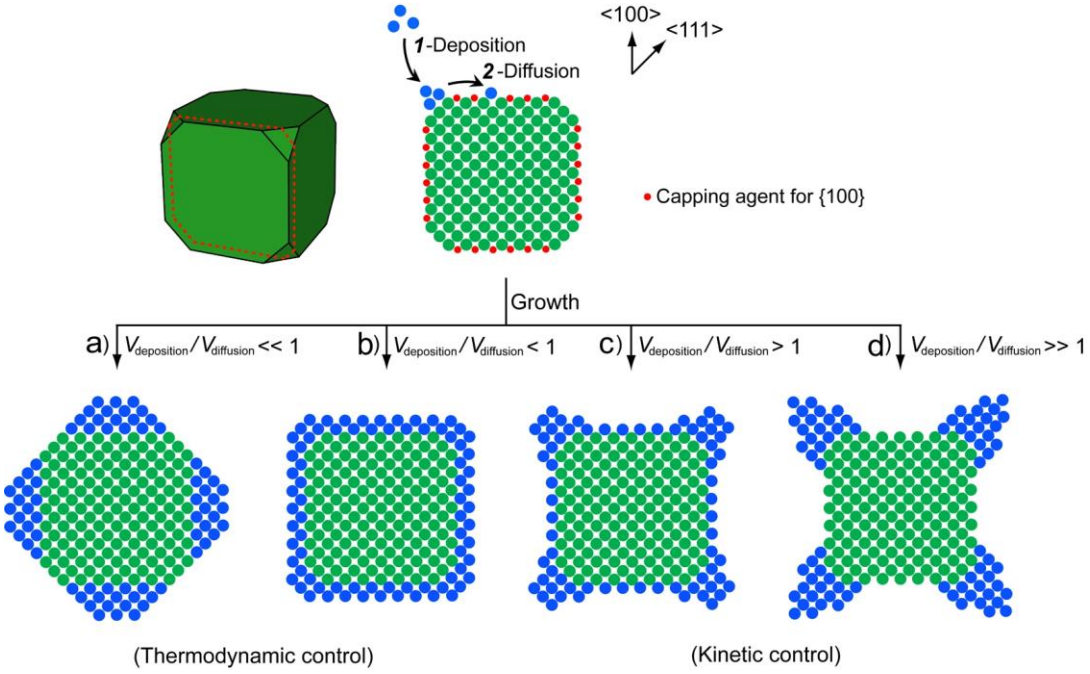

Figure 1.5. Schematic illustrations showing the shape evolution of a cubic seed, with its side faces being covered by a capping agent, under four different kinetic conditions. The 2D atomic models correspond to the cross-section (dashed red line) in the 3D model. (Reprinted with permission from [101]. Copyright 2015 American Chemical Society.)

$V_{diffusion}$ are situated between the two extremes. For instance, when $V_{deposition}/V_{diffusion}$ is slightly less than 1, some of the adatoms will stay at the corners whereas the rest can diffuse to the edges and side faces, leading to the formation of an enlarged cube with slightly truncated corners (Figure 1.5b). This shape is also favored by thermodynamics as long as there is enough capping agent in the reaction solution to effectively passivate and thus stabilize the enlarged side faces. When $V_{deposition}/V_{diffusion}$ is slightly greater than one, a small portion of the adatoms at the corners can migrate to the edges (which are relatively more reactive than the side faces due to a lower coverage density for the capping agent). As a result, the product will become a concave cube (Figure 1.5c). It is

worth pointing out that the total surface free energies of these four different types of nanocrystals are expected to increase in the order of: cuboctahedron < truncated cube < concave cube < octapod. In conclusion, the surface diffusion rate can serve as a reference point to determine if the product is formed under thermodynamic or kinetic control. When $V_{deposition}/V_{diffusion} < 1$, the synthesis is under thermodynamic control, and the synthesis is under kinetic control when $V_{deposition}/V_{diffusion} > 1$.

Significantly, both $V_{deposition}$ and $V_{diffusion}$ can be varied experimentally in a well-controlled fashion. In general, $V_{deposition}$ has a direct correlation with the rate at which the newly formed metal atoms are supplied. This rate is largely determined by the reduction rate (r) of a salt precursor (A) by a reductant (B). In an ideal reaction situation (without the involvement of intermediate steps), r can be expressed as Eq. (1.5):

$$r = k\,[\mathrm{A}]^m \cdot [\mathrm{B}]^n \qquad (1.5)$$

where [A] and [B] are the molar concentrations of A and B, respectively; exponents m and n are the reaction orders with respect to A and B; and k is the rate constant of the reduction reaction that has a strong dependence on temperature [53]. As a result, $V_{deposition}$ can be manipulated in a number of ways, including variations of reagent concentration and reaction temperature, the choice of a specific type of reductant or precursor, and the type of coordination ligand for the metal ion. Among them, controlling the injection rate of the precursor solution (typically, the precursor) with the use of a syringe pump has been demonstrated to be a simple and effective method for controlling the reagent concentration, and thus the magnitude of $V_{deposition}$ [83].

Surface diffusion is a thermally activated process that involves the motion of adatoms on a solid surface through a jumping or hopping mechanism [84]. The diffusion coefficient (D) that measures the rate of jumping of an adatom across a surface can be expressed as an Arrhenius-type equation:

$$D = D_0 \exp(-E_{diff}/RT) \quad (1.6)$$

where D_0 is the pre-exponential factor, E_{diff} is the potential barrier to diffusion, R is the ideal gas constant, and T is the absolute temperature. Clearly, for surface diffusion of adatoms across the surface of a growing seed, D and thus $V_{diffusion}$ are mainly determined by the reaction temperature and E_{diff}. In general, E_{diff} is determined by a number of factors, including the strength of bond between the surface atom and the adatom, the crystallographic plane of the surface, the accessibility of the surface (*e.g.*, passivation by a capping agent), and the chemical potential gradient [85]. For example, it has been showed that the value of E_{diff} for Rh adatoms diffusing on a closely-packed Rh(111) surface was 0.16 eV, while this value increased to 0.60 and 0.88 eV, respectively, when diffusing on loosely-packed Rh(110) and Rh(100) surfaces [67]. During a synthesis, adjusting the reaction temperature should be a simple and straightforward approach to the manipulation of $V_{diffusion}$. It should be pointed out that, in many cases, the alteration of parameters such as temperature might also result in changes to both $V_{deposition}$ and $V_{diffusion}$. As a result, one needs to carefully design an experiment to achieve the desired range of values for the ratio of $V_{deposition}$ to $V_{diffusion}$.

To sum up, in order to access the kinetic products of seed-mediated growth, one has to figure out the sites onto which the atoms newly formed from a salt precursor will be deposited, as well as all possible paths for the adatoms to migrate away through surface diffusion. In principle, the newly formed atoms tend to be added to the site on a growing seed with the highest surface free energy and then migrate to the other sites lower in free energies *via* surface diffusion. The specific surface free energy of a seed is determined by the types of facets exposed, the involvement of capping agent, and the presence of twin defects. The specific surface free energy of a facet will decrease when the facet is

passivated by a capping agent. The extent of decrease in γ due to the chemisorption of a capping agent is determined by both the type of capping agent and its coverage density on the surface [86]. It should be emphasized that a capping agent can not only lower the γ value of a surface but also increase the energy barrier to surface diffusion [85]. In many cases, the shape taken by the product is a compromise of these two processes. Secondly, the ratio of $V_{\text{deposition}}$ to $V_{\text{diffusion}}$ needs to be adjusted to an appropriate range by carefully controlling the reaction kinetics to achieve the desired shapes.

1.2.3 Symmetry Breaking

The symmetry of a crystal is of great importance to materials science as it dictates the physical behaviors of a solid, including its mechanical, optical, thermal, magnetic, and electrical properties. Symmetry breaking has enabled the synthesis of colloidal metal nanocrystals with diversified shapes or morphologies, together with novel properties for a variety of applications. Notable examples include one-dimensional nanostructures (*e.g.*, nanorods and nanowires) and twinned nanoparticles (*e.g.*, decahedrons and icosahedrons) whose symmetries do not commensurate with those of the corresponding crystal lattices or unit cells. In general, the symmetry of a nanocrystal can be broken during the nucleation and growth stages in a solution phase synthesis. For a single-crystal seed made of an *fcc* metal, it tends to grow into a highly symmetric shape such as cube, cuboctahedron, or octahedron depending on the relative growth rates along the <100> and <111> directions [87]. When prepared using a highly isotropic medium, nanocrystals with reduced symmetry can only be obtained by breaking the intrinsic confinement imposed by the cubic symmetry of its unit cell during the course of growth. In comparison, the inclusion of twin defects in a defect-lined crystal can naturally break the symmetry of an *fcc* lattice. Notable examples include the formation of decahedral, icosahedral, and plate-like seeds, followed by their growth into penta-twinned nanorods

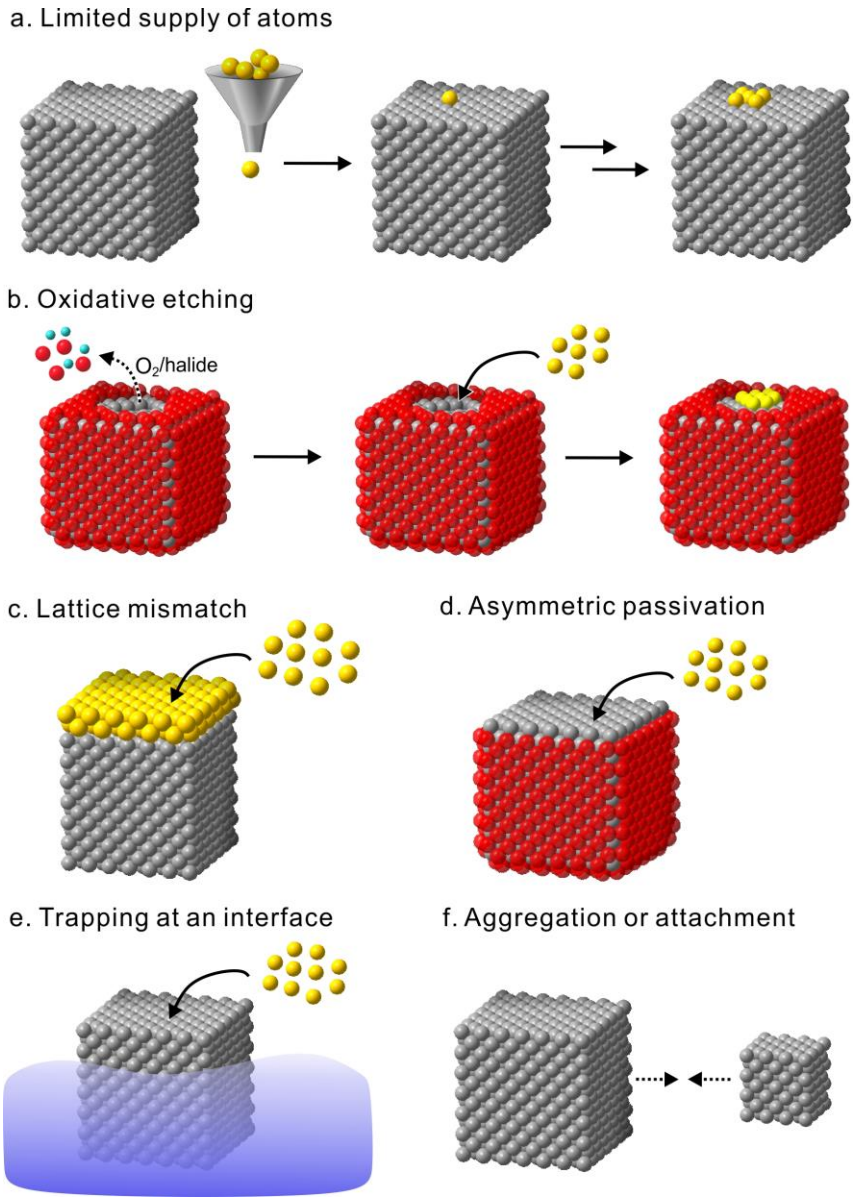

Figure 1.6. A summary of six different experimental strategies that have been demonstrated for breaking the symmetry of a cubic seed during the growth. The first five strategies are based on the atomic addition mechanism while the last one involves aggregative growth. For clarity, the atoms added (or to be added) onto the surface of a seed and the metal ions released from the etching are shown in golden and blue colors, respectively. The red dot in (b, d) corresponds to the capping agent chemisorbed on the surface of a seed.

or nanowires with a pentagonal cross-section or nanoplates with a triangular or hexagonal profile [87−94].

A seed can evolve into nanocrystals with diversified shapes and different symmetries during growth. As illustrated in Figure 1.6 for a single-crystal, cubic seed, its symmetry can be reduced (or broken) through the following mechanisms or pathways: manipulation of reaction kinetics to limit the supply of atoms and thus influence the growth mode; involvement of oxidative etching; overgrowth involving two metals with a significant lattice mismatch; passivation of certain regions of the surface to reduce the symmetry of a seed; trapping of the seed at an interface; and aggregation or attachment of the seeds or nanocrystals [95−100]. Notably, the products obtained from asymmetric growth typically display anisotropic, thermodynamically less favorable shapes. For example, in an ideal situation, the concentric core-shell nanocubes, resulting from the deposition of atoms of a second metal onto all six side faces of a cubic seed, are thermodynamically more favorable than both the non-concentric nanocubes and hybrid dimers originated from the selective growth along three adjacent and one of the six side faces of a cubic seed, respectively. In this case, the asymmetric growth of highly symmetric seeds can be induced through kinetic control by simply manipulating the rate at which metal atoms were generated and deposited from a precursor. When the number of atoms available is smaller than the number of equivalent sites on the surface of a seed, the growth pattern will automatically become asymmetric. This is particularly important in the very early stage of a seeded growth process because the growth pattern will be essentially retained once it has been initiated when surface diffusion is relatively slow.

1.3 Scope of this Work

The aim of this work is to achieve a quantitative understanding of shape evolution of colloidal noble-metal nanocrystals. Despite the significant success that has been accomplished over the past few decades in controlling the shape of noble-metal

nanocrystals, it is largely based on a trial and error approach. It will be more powerful and productive if there is a quantitative understanding of the thermodynamic and kinetic factors responsible for the mechanism and pathways during the nucleation and growth of nanocrystals. The dissertation is organized into two main sections: *i*) quantitative analysis of the coverage density of a surface capping agent and a mechanistic study of its effect on the heterogeneous nucleation and growth of nanocrystals, and *ii*) quantitative understanding of role of kinetic parameters involved in a synthesis, including reduction kinetics and surface diffusion rate, in determining the internal structure and the growth mode of a seed.

In Chapter 2, I describe a method for quantitatively analyzing the role played by Br^- ions in the synthesis of Pd nanocrystals using a combination of inductively coupled plasma mass spectrometry (ICP-MS) and X-ray photoelectron spectroscopy (XPS). The coverage density of Br^- ions on Pd{100} could be directly derived from the ratio of Br^- ions to Pd atoms obtained from the ICP-MS analysis for Pd nanocubes. I have also investigated the binding mechanism of the chemisorbed Br^- ions using XPS. On the basis of the quantitative information, I further demonstrated that the minimum amount of Br^- ions needed for capping the surface of Pd nanocubes with a certain size could be estimated in advance during the design of an experiment.

In Chapter 3, I apply the collision model that has long been established in surface science to seed-mediated growth of nanocrystals in an effort to account for the deposition probability of atoms on the surface of a seed and thus its growth pattern in the presence or absence of surface capping. Using palladium nanocubes as a model system, I demonstrate how the atom deposition occurs on a cubic seed with its side facets being free of or passivated by chemisorbed Br^- ions. The mechanistic insights from this study also indicate that the growth pattern of a seed strongly depends on its surface condition as well as the rate of surface diffusion.

In Chapter 4, with the polyol synthesis of Pd nanocrystals as an example, I

demonstrate that kinetics parameters, including rate constant and activation energy, can be derived from spectroscopic measurement. These parameters can be used to calculate the initial reduction rate of a given reaction and further study its quantitative correlation with the internal structure of a seed and nanocrystal. On a quantitative basis, the ranges of initial reduction rates required for the formation of nanocrystals with a specific internal structure, including single-crystal, multiply twinned, and stacking fault-lined, can all be determined and even allow one to design new experiments.

In Chapter 5, I develop a model to analyze the symmetry breaking phenomenon involved in the seed-mediated growth of Pd nanocrystals under the dropwise addition of a precursor solution with the use of a syringe pump. The dropwise approach allows for a tight control over the reduction and thus the achievement of a steady state for the number of precursor ions in the growth solution. By correlating the growth modes with the reaction kinetics of a given synthesis, I demonstrate that symmetry breaking can only be initiated and retained by keeping the atom deposition at a rate slow enough to limit the number of initial nucleation sites on a seed but faster enough to beat the surface diffusion process.

1.4 Notes to Chapter 1

Part of this chapter is adapted from the perspective article "Shape-controlled synthesis of colloidal metal nanocryatsls: Thermodynamic *versus* kinetic products" co-authored by me and published in *Journal of the American Chemical Society* [101].

1.5 References

[1] Lewis, L. N. *Chem. Rev.* **1993**, *93*, 2693−2730.

[2] Somorjai, G. A. *Chem. Rev.* **1996**, *96*, 1223−1236.

[3] Aiken III, J. D.; Finke, R. G. *J. Mol. Catal. A-Chem.* **1999**, *145*, 1−44

[4] Ertl, G. *Handbook of Heterogeneous Catalysis*, Wiley-VCH, Weinheim, **2008**.

[5] N. M. Davey, R. J. Seymour, *Platinum Met. Rev.* **1985**, *29*, 2.

[6] Okinaka, Y.; Hoshino, M. *Gold Bull.* **1998**, *31*, 3−13.

[7] Jeong, S.; Woo, K.; Kim, D.; Lim, S.; Kim, J. S.; Shin, H.; Xia, Y.; Moon, J. *Adv. Funct. Mater.* **2008**, *18*, 679−686.

[8] Talapin, D. V.; Lee, J.-S.; Kovalenko, M. V.; Shevchenko, E. V. *Chem. Rev.* **2010**, *110*, 389−458.

[9] Maier, S. A.; Brongersma, M. L.; Kik, P. G.; Meltzer, S.; Requicha, A. A. G.; Atwater, H. A. *Adv. Mater.* **2001**, *13*, 1501−1505.

[10] Kauranen, M.; Zayats, A. V. *Nat. Photonics* **2012**, *6*, 737−748.

[11] Gupta, M. C.; Ballato, J. *The Handbook of Photonics*, CRC Press, Taylor & Francis Group, Boca Raton, **2006**.

[12] Koenderink, A. F.; Alù, A.; Polman, A. *Science* **2015**, *348*, 516−521.

[13] Murray, C. B.; Sun, S.; Doyle, H.; Betley, T. *MRS Bull.* **2001**, *26*, 985−991.

[14] Kozicki, M. N; Mitkova, M.; Park, M.; Balakrishnan, M.; Gopalan, C. *Superlattices Microst.* **2004**, *34*, 459−465.

[15] Ditlbacher, H.; Lamprecht, B.; Leitner, A.; Aussenegg F. R. *Optics Lett.* **2000**, *25*, 563−565.

[16] Nozik, A. J.; Miller, J. *Chem. Rev.* **2010**, *110*, 6443−6445.

[17] Linic, S. Christopher, P.; Ingram, D. B. *Nat. Mater.* **2011**, *10*, 911−921.

[18] Jena, P. *J. Phys. Chem. Lett.* **2011***, 2*, 206−211.

[19] Cohn, J. G. *Environ. Health Perspect.* **1975**, *10*, 159−164.

[20] Parks II, J. E. *Science* **2010**, *327*, 1584−1585.

[21] Alivisatos, P. *Nat. Biotechnol.* **2004**, *22*, 47−52.

[22] Jain, P. K.; El-Sayed, I. H.; El-Sayed, M. A. *Nano Today* **2007**, *2*, 18−29.

[23] Burda, C.; Chen, X.; Narayanan, R.; El-Sayed, M. A. *Chem. Rev.* **2005**, *105*, 1025−1102.

[24] Xia, Y.; Li, W.; Cobley, C. M.; Chen, J. ; Xia, X.; Zhang, Q.; Yang, M.; Cho, E. C.; Brown P. K. *Acc. Chem. Res.* **2011**, *44*, 914−924.

[25] Grzelczak, M.; Pérez-Juste, J.; Mulvaney, P.; Liz-Márzan, L. M. *Chem. Soc. Rev.* **2008**, *37*, 1783−1791.

[26] Camden, J. P.; Dieringer, J. A.; Zhao, J.; Van Duyne, R. P. *Acc. Chem. Res.* **2008**, *41*, 1653−1661.

[27] Burda, C.; Chen, X.; Narayanan, R.; El-Sayed, M. A. *Chem. Rev.* **2005**, *105*, 1025−1102.

[28] Rycenga, M.; Cobley, C. M.; Zeng, J.; Li, W.; Moran, C. H.; Zhang, Q.; Qin, D.; Xia, Y. *Chem. Rev.* **2011**, *111*, 3669−3712.

[29] Eustis, S.; El-Sayed, M. A. *Chem. Soc. Rev.* **2006**, *35*, 209−217.

[30] Mayer, K. M.; Hafner, J. H. *Chem. Rev.* **2011**, *111*, 3828−3857.

[31] Willets, K. A.; Van Duyne, R. P. *Annu. Rev. Phy. Chem.* **2007**, *58*, 267−297.

[32] Mulvaney, P. *Langmuir* **1996**, *12*, 788−800.

[33] Murphy, C. J.; Sau, T. K.; Gole, A. M.; Orendorff, C. J.; Gao, J.; Gou, L.; Hunyadi, S. E.; Li, T. *J. Phys. Chem. B* **2005**, *109*, 13857−13870.

[34] Lee, K. S.; El-Sayed, M. A. *J. Phys. Chem. B* **2005**, *109*, 20331−20338.

[35] Ye, X.; Jin, L.; Caglayan, H.; Chen, J.; Xing, G.; Zheng, C.; Doan-Nguyen, V.; Kang, Y.; Engheta, N.; Kagan, C. R.; Murray, C. B. *ACS Nano* **2012**, *6*, 2804−2817.

[36] McLellan, J. M.; Li, Z.-Y.; Siekkinen, A. R.; Xia, Y. *Nano Lett.* **2007**, *7*, 1013−1017.

[37] Mulvihill, M.; Tao, A.; Benjauthrit, k.; Arnold, J.; Yang, P. *Angew. Chem., Int. Ed.* **2008**, *47*, 6456−6460.

[38] Aslan, K.; Lakowicz, J. R.; Geddes, C. D. *Anal. Bioanal. Chem.* **2005**, *382*, 926−933.

[39] Narayanan, R.; El-Sayed, M. A. *Nano Lett.* **2004**, *4*, 1343−1348.

[40] Guo, S.; Zhang, S.; Sun, S. *Angew. Chem., Int. Ed.* **2013**, *52*, 8526−8544.

[41] Xie, S.; Choi, S.-I., Xia, X.; Xia, Y. *Curr. Opin. Chem. Eng.* **2013**, *2*, 142−150.

[42] Bratlie, K. M.; Kilewer, C. J.; Somorjai, G. A. *J. Phys. Chem. B* **2006**, *110*, 17925−17930.

[43] Shao, M.; Yu, T.; Odell, J. H.; Jin, M.; Xia, Y. *Chem. Commun.* **2011**, *47*, 6566−6568.

[44] Stamenkovic, V. R.; Fowler, B.; Mun, B. S.; Wang, G.; Ross, P. N.; Lucas, G. A.; Marković, N. M. *Science* **2007**, *315*, 493−497.

[45] Xu, R.; Wang, D.; Zhang, J.; Li, Y. *Chem. Asian J.* **2006**, *1*, 888−893.

[46] Lee, I.; Morales, R.; Albiter, M. A.; Zaera, F. *Proc. Natl. Acad. Sci. USA* **2008**, *105*, 15241−15246.

[47] Tian, N.; Zhou, Z. Y.; Sun, S. G.; Ding, Y.; Wang, Z. L. *Science* **2007**, *316*, 732−735.

[48] Xia, Y.; Xiong, Y.; Lim, B.; Skrabalak, S. E. *Angew. Chem., Int. Ed.* **2009**, *48*, 60−103.

[49] Tao, A. R.; Habas, S.; Yang, P. *Small* **2008**, *4*, 310−325.

[50] Zhang, H.; Jin, M.; Xia, Y. *Angew. Chem., Int. Ed.* **2012**, *51*, 7656−7673.

[51] Lim, B.; Xia, Y. *Angew. Chem., Int. Ed.* **2011**, *50*, 76−85.

[52] Quan, Z.; Wang, Y.; Fang, J. *Acc. Chem. Res.* **2013**, *46*, 191−202.

[53] Atkins, P.; de Paula, J. *Physical Chemistry*, 8th Ed.; W.H. Freeman, New York, **2006**.

[54] Markov, I. V. *Crystal Growth for Beginners: Fundamentals of Nucleation, Crystal Growth and Epitaxy*, 1st Ed.; World Scientific, Singapore, **1995**.

[55] Mackenzie, J. K.; Moore, A. J. W.; Nicholas, J. F. *J. Phys. Chem. Solids* **1962**, *23*, 185−196.

[56] Frenken, J. W. M.; Stoltze, P. *Phys. Rev. Lett.* **1999**, *82*, 3500−3503.

[57] Galanakis, I.; Papanikolaou, N.; Dederichs, P. H. *Surf. Sci.* **2002**, *511*, 1−12.

[58] Zhang, J. M.; Ma, F.; Xu, K. W. *Appl. Surf. Sci.* **2004**, *229*, 34−42.

[59] Wulff, G. Z. *Kristallogr. Mineral.* **1901**, *34*, 449−530.

[60] Kumikov, V. K.; Khokonov, Kh. B. *J. Appl. Phys.* **1983**, *54*, 1346−1350.

[61] Surnev, S.; Arenhold, K.; Conen, P.; Voigtländer, Bonzel, H. P. *J. Vac. Sci. Technol. A* **1998**, *16*, 1059−1065.

[62] Bonzel, H. P.; Emundts, A. *Phys. Rev. Lett.* **2000**, *84*, 5804−5807.

[63] Burrows, M. G. T.; Stockmayer, W. H. *Surf. Sci.* **1940**, *176*, 471−483.

[64] Ertl, G.; Rau, P. *Surf. Sci.* **1969**, *15*, 443−465.

[65] Shi, A.-C.; Masel, R. I. *J. Catal.* **1989**, *120*, 421−431.

[66] Roberts, M. W. *Surf. Sci.* **1994**, *299*, 769−784.

[67] Wang, T.; Lee, C.; Schmidt, L. D. *Surf. Sci.* **1985**, *163*, 181−197.

[68] Oura, K.; Lifshits, V. G.; Saranin, A. A.; Zotov, A. V.; Katayama, M. *Surface Science: An Introduction*, 1st Ed.; Springer, Heidelberg, **2003**.

[69] Harris, P. J. F. *Nature* **1986**, *323*, 792−794.

[70] Somorjai, G. A. *J. Catal.* **1972**, *27*, 453−456.

[71] Chen, M.; Wu, B.; Yang, J.; Zheng, N. *Adv. Mater.* **2012**, *134*, 15822−15831.

[72] Chiu, C.-Y.; Ruan, L.; Huang, Y. *Chem Soc. Rev.* **2013**, *42*, 2512−2527.

[73] Lohse, S. E.; Burrows, N. D.; Scarabelli, L.; Liz-Mazán, L. M.; Murphy, C. J. *Chem Mater.* **2014**, *26*, 34−43.

[74] Niu, Z.; Li, Y. *Chem. Mater.* **2014**, *26*, 72−83.

[75] Zeng, J.; Zheng, Y.; Rycenga, M.; Tao, J.; Li, Z.-Y.; Zhang, Q.; Zhu, Y.; Xia, Y. *J. Am. Chem. Soc.* **2010**, *132*, 8552−8553.

[76] Millstone, J. E.; Wei, W.; Jones, M. R.; Yoo, H.; Mirkin, C. A. *Nano Lett.* **2008**, *8*, 2526−2529.

[77] Huang, X.; Zheng, N. *J. Am. Chem. Soc.* **2009**, *131*, 4602−4603.

[78] Zhang, J.; Fang, J. Wang, C.; Daimon, H.; Lee, Y.; Kim, J.; Sun, S. *J. Am. Chem. Soc.* **2007**, *129*, 6974−6975.

[79] Huang, X.; Tang, S.; Mu, X.; Dai, Y.; Chen, G.; Zhou, Z.; Ruan, F.; Yang, Z.;

Zheng, N. *Nat. Nanotechnol.* **2011**, *6*, 28−32.

[80] Chiu, C.-Y.; Li, Y.; Ruan, L.; Ye, X.; Murray, C. B.; Huang, Y. *Nat. Chem.* **2011**, *3*, 393−399.

[81] Heinz, H.; Farmer, B. L.; Pandey, R. B.; Slocik, J. M.; Patnaik, S. S.; Pachter, R.; Naik, R. R. *J. Am. Chem. Soc.* **2009**, *131*, 9704−9714.

[82] O'Brien, M. N.; Radha, B.; Brown, K. A.; Jones, M. R.; Mirkin, C. A. *Angew. Chem., Int. Ed.* **2014**, *53*, 9532−9538.

[83] Zhang, H.; Li, W.; Jin, M.; Zeng, J.; Yu, T.; Yang, D.; Xia, Y. *Nano Lett.* **2011**, *11*, 898−903.

[84] Tringides, M. C. (ed.) *Surface Diffusion: Atomistic and Collective Processes.* NATO ASI Series B: Physics. Volume 360, Plenum Press, New York and London, **1997**.

[85] Shustorovich, E. *Metal-Surface Reaction Energetics: Theory and Applications to Heterogeneous Catalysis, Chemisorption, and Surface Diffusion*, Wiley-VCH, **1991.**

[86] Xia, X.; Zeng, J.; Zhang, Q.; Moran, C. M.; Xia, Y. J. *Phys. Chem. C* **2012**, *116*, 21647−21656.

[87] Sun, Y.; Gates, B.; Mayers, B.; Xia, Y. *Nano Lett.* **2002**, *2*, 165−168.

[88] Malikova, N.; Pastoriza-Santos, I.; Schierhorn, M.; Kotov, N. A.; Liz-Márzan, L. M. *Langmuir* **2002**, *18*, 3694−3697.

[89] Jana, N. R.; Gearheart, L.; Murphy, C. J. *Adv. Mater.* **2001**, *13*, 1389−1393.

[90] Huang, X.; Zheng, N. *J. Am. Chem. Soc.* **2009**, *131*, 4602−4603.

[91] Yang, H.; He, S.; Tuan, H. *Langmuir* **2014**, 30, 602−610.

[92] Pietrobon, B.; McEachran, M.; Kitaev, V. *ACS Nano* **2009**, *3*, 21−26.

[93] Zhang, Q.; Hu, Y.; Guo, S.; Goebl, J.; Yin, Y. *Nano Lett.* **2010**, *10*, 5037−5042.

[94] Millstone, J. E.; Hurst, S. J.; Métraux, G. S.; Cutler, J. I.; Mirkin, C. A. *Small* **2009**, *5*, 646−664.

[95] Zeng, J.; Zhu, C.; Tao, J.; Jin, M.; Zhang, H.; Li, Z.-Y.; Zhu, Y.; Xia, Y. *Angew.*

Chem., Int. Ed. **2012**, *51*, 2354−2358.

[96] Cobley, C. M.; Rycenga, M.; Zhou, F.; Li, Z.; Xia, Y. *Angew. Chem., Int. Ed.* **2009**, *48*, 4824−4827.

[97] Jin, M.; Zhang, H.; Wang, J.; Zhong, X.; Lu, N.; Li, Z.-Y.; Xie, Z.; Kim, M. J.; Xia, Y. *ACS Nano* **2012**, *6*, 2566−2573.

[98] Lee, S.-U.; Hong, J. W.; Choi, S.-I.; Han, S. W. *J. Am. Chem. Soc.* **2014**, *136*, 52215−5224.

[99] Zhang, L.; Wang, Y.; Tong, L.; Xia, Y. *Nano Lett.* **2014**, *14*, 4189−4194.

[100] Halder, A.; Ravishankar, N. *Adv. Mater.* **2007**, *19*, 1854−1858.

[101] Xia, Y.; Xia, X.; Peng, H.-C. *J. Am. Chem. Soc.* **2015**, *137*, 7947−7966.

CHAPTER 2

QUANTITATIVE ANALYSIS OF THE COVERAGE DENSITY OF BROMIDE ON THE {100} FACETS OF PALLADIUM AND ITS ROLE IN CONTROLLING THE SHAPE OF PALLADIUM NANOCRYSTALS

2.1 Introduction

Palladium nanocrystals with controlled shapes have received considerable interest in recent years owing to their remarkable performance towards various catalytic reactions, including alkene hydrogenation [1−3], CO oxidation [4−6], and various organic coupling reactions [7−9]. It is well-known that the catalytic activity and selectivity of nanocrystals for a structure-sensitive reaction is strongly dependent on the type of facets exposed on the surface [10, 11]. Therefore, nanocrystals with a specific shape and thus the desired facet would be invaluable to various catalytic applications. Thanks to the efforts of many research groups, a large number of protocols for the synthesis of Pd nanocrystals with distinct shapes have been developed by identifying various capping agents, and by developing strategies based on kinetic control [12−15]. As discussed in Chapter 1.2.1, the general function of a capping agent in a thermodynamically controlled synthesis is to stabilize surface atoms with a specific arrangement through selective chemisorption and change the order of surface free energies of various types of facets. As a result, the growth rates along different crystallographic directions will be altered, leading to the formation of nanocrystals with diversified shapes [16−19].

Bromide ions have been widely used as a capping agent for the synthesis of Pd and Ag nanocrystals enclosed by {100} facets such as nanocubes and nanobars because of their preferential binding to the (100) surface [20−23]. A typical protocol for the synthesis of Pd nanocubes involves the reduction of a Pd(II) precursor by ascorbic acid in the presence of KBr or NaBr. The function of Br^- ions is believed to serve as a capping agent for the Pd(100) surface, effectively altering the order of surface free energies and thus promoting the formation of Pd nanocrystals enclosed by {100} facets. Despite the full demonstration of its critical role in the formation of Pd nanocubes and nanobars, there is still no experimental evidence to support the proposed mechanism. As a result, a quantitative analysis of the role played by Br^- ions in the synthesis of Pd nanocrystals would be critically important to both fundamental understanding and future development.

2.2 Results and Discussion

In this work, I quantitatively analyzed the role played by Br^- ions in the synthesis of Pd nanocubes using a combination of inductively coupled plasma mass spectrometry and X-ray photoelectron spectroscopy. Unlike other techniques for surface analysis such as scanning tunneling microscopy (STM), which usually requires the use of an extended surface and cannot easily generate chemical information [24], I could directly obtain both elemental and surface chemical information of nanocrystals by combining ICP-MS and XPS. Thanks to the high sensitivity of ICP-MS, it is possible to directly measure the number of Br^- ions adsorbed on the surface of a specific number of Pd nanocubes. To achieve a better statistics for the coverage density of Br^- ions on Pd(100), I used Pd nanocubes with three different edge lengths of 7.5, 10.5, and 18 nm, respectively (Figure

2.1). The samples were washed with deionized (DI) water four times to remove the excess capping agent. Table 2.1 lists the atomic ratio of Br^- ions to Pd atoms for these samples as obtained from ICP-MS analysis. The ratio decreased from 0.11 to 0.09 and 0.05 as the edge length of Pd nanocubes increased from 7.5 to 10.5 and 18 nm. Because of the higher surface area to volume ratios for smaller nanocubes, it is expected to observe such a negative correlation between the Br^-/Pd ratio and the edge length. Based on the crystal structure of Pd and the size of nanocubes, I further calculated the ratio between Br^- ions and surface Pd atoms, and then the coverage densities of Br^- ions on these Pd nanocubes. As shown in Table 2.1, these two parameters were more or less the same across the three different samples of nanocubes. Considering the possible truncation at corners [25], a value of 0.8 for the ratio between Br^- ions and surface Pd atoms indicated that the Br^- ions formed a monolayer on the {100} facets of Pd nanocubes.

Table 2.1. ICP-MS analysis of the coverage density of Br^- ions on the surfaces of Pd nanocubes with different edge lengths.

Size of Pd cubes	Br^- to all Pd	Br^- to surface Pd	Br^- density (ions/nm^2)
7.5 nm	0.114	0.74	9.7 ± 0.3
10.5 nm	0.087	0.78	10.3 ± 0.3
18.0 nm	0.053	0.82	10.8 ± 0.6

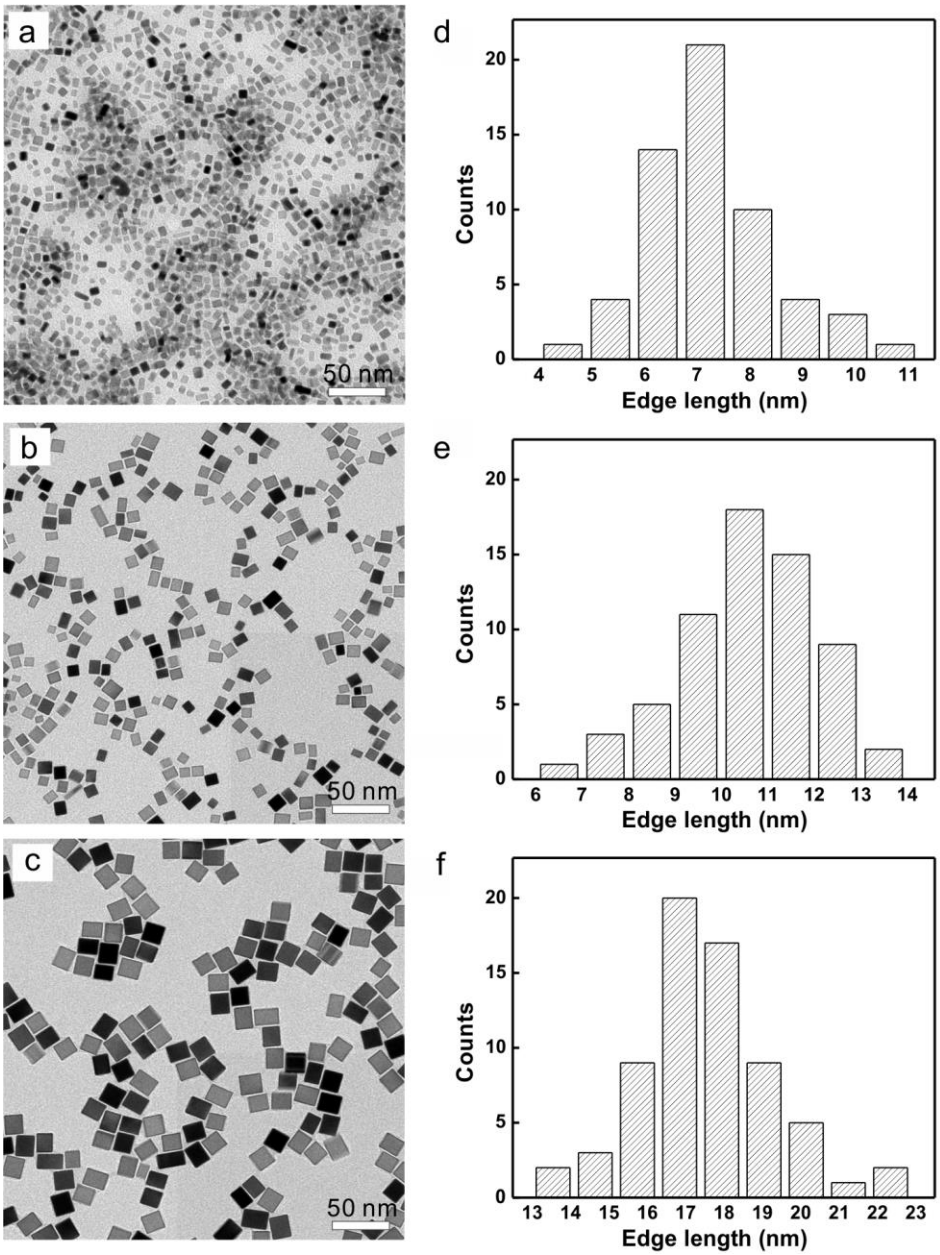

Figure 2.1. TEM images of Pd nanocubes with edge lengths of (a) 7.5 nm, (b) 10.5 nm, and (c) 18 nm, respectively; (d−f) The corresponding statistical analysis of size distribution for each sample. (Reprinted with permission from [32]. Copyright 2013 American Chemical Society.)

In general, there are two types of interactions between a capping agent and the metal surface: physisorption and chemisorption [26, 27]. In order to decipher which type of interaction is involved in the case of Br^- ions and Pd nanocubes, a set of experiments were conducted with XPS analysis. First, I analyzed the surface chemical composition of a sample of Pd nanocubes (18 nm) that had been washed with DI water for different times. Surprisingly, in addition to Pd 3d, peaks of N 1s, C 1s, and Br 3d were also observed in the survey spectra (Figure 2.2), indicating that the Br^- ions and PVP, a colloidal stabilizer, could not be removed by washing with DI water only.

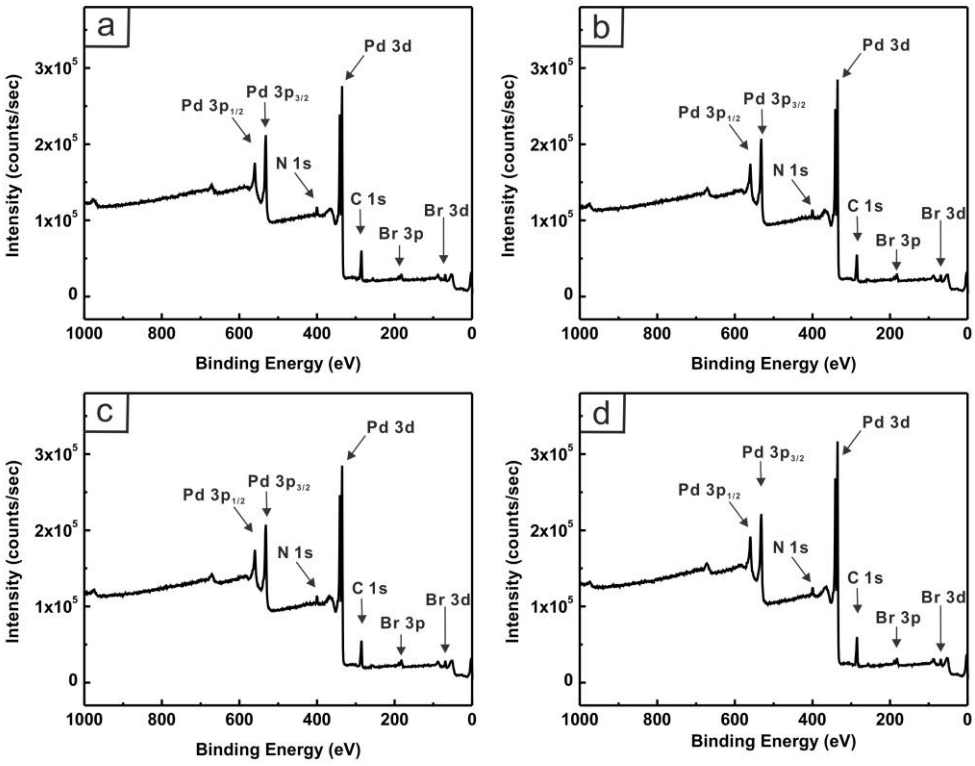

Figure 2.2. XPS survey spectra of Pd nanocubes (18 nm in edge length) that had been washed (a) 3, (b) 4, (c) 6, and (d) 8 times with DI water. (Reprinted with permission from [32]. Copyright 2013 American Chemical Society.)

Since the physically adsorbed Br^- ions should be gradually removed during the washing process, this result suggested that chemisorption was likely the main interaction between Br^- ions and Pd(100). It is expected the chemisorbed Br^- ions could be removed only by desorption at a higher temperature. I demonstrated this concept by conducting another set of experiments, in which aqueous or ethylene glycol suspensions containing PVP, citric acid, and the Pd nanocubes were aged at different temperatures for 18 hours. The role of citric acid was to act as a mild reducing agent for the Pd^{2+} ions bound to the surface. Transmission electron microscopy (TEM) characterization showed that there was no significant change to the cubic shape of the nanocubes during the aging process (see Figure 2.3).

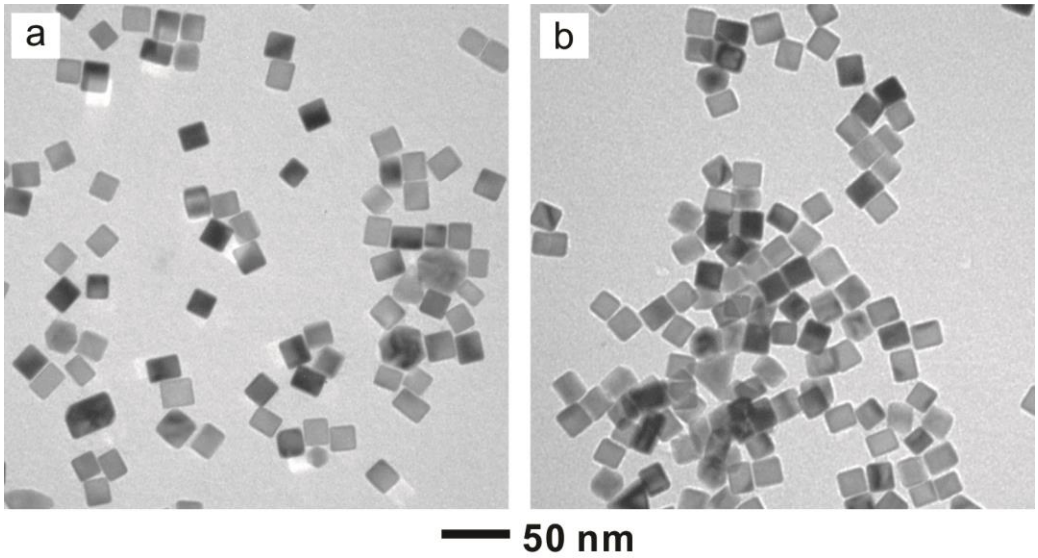

Figure 2.3. TEM images of Pd nanocubes (18 nm in edge length) that had been aged at (a) 80 °C and (b) 100 °C, respectively, for 18 hours. (Reprinted with permission from [32]. Copyright 2013 American Chemical Society.)

Figure 2.4a shows high-resolution Pd 3d XPS spectra of the samples. The two peaks located at 340.4 and 335.1 eV can be assigned to elemental Pd $3d_{3/2}$ and Pd $3d_{5/2}$, respectively. The shoulders at higher energies (342.2 eV for Pd $3d_{3/2}$ and 337.2 eV for Pd $3d_{5/2}$), which are consistent with the reported values for Pd(II) samples [28], confirmed the existence of Pd(II) species on the surface of the nanocubes due to the chemisorption of Br^- ions. However, when the nanocubes were aged in the aqueous or ethylene glycol (EG) solution containing a reducing agent at an elevated temperature, the shoulders gradually decreased in intensity and completely disappeared for the EG sample aged at 100 °C. The drop in intensity for the shoulder peaks indicates that some of the surface Pd(II) were reduced to Pd(0) by citric acid during the aging process. Moreover, it is worth pointing out that the Pd(0) peak of the EG sample aged at 100 °C slightly shifted to a higher energy, which is due to charge transfer from Pd to PVP, as reported in prior studies [29].

The temperature dependence of the intensities of the shoulder peaks can be understood by the following argument: when the temperature was increased, the desorption of Br^- ions would be accelerated and the reducing power of citric acid would be increased too. Synergistically, this would lead to the reduction of Pd(II) to Pd(0) and removal of Br^- ions from the surface. This picture is supported by the ICP-MS data in Figure 2.4b, where the amount of Br^- ions remaining on the surface of the Pd nanocubes showed a similar trend after aging under different conditions. When the sample was treated in EG at 100 °C, the amount of Br^- ions dropped to only 12% of the original value. I analyzed the concentration of Pd ions in the supernatant of the reaction solution using ICP-MS and found essentially no detectable amount of Pd ions in the supernatant,

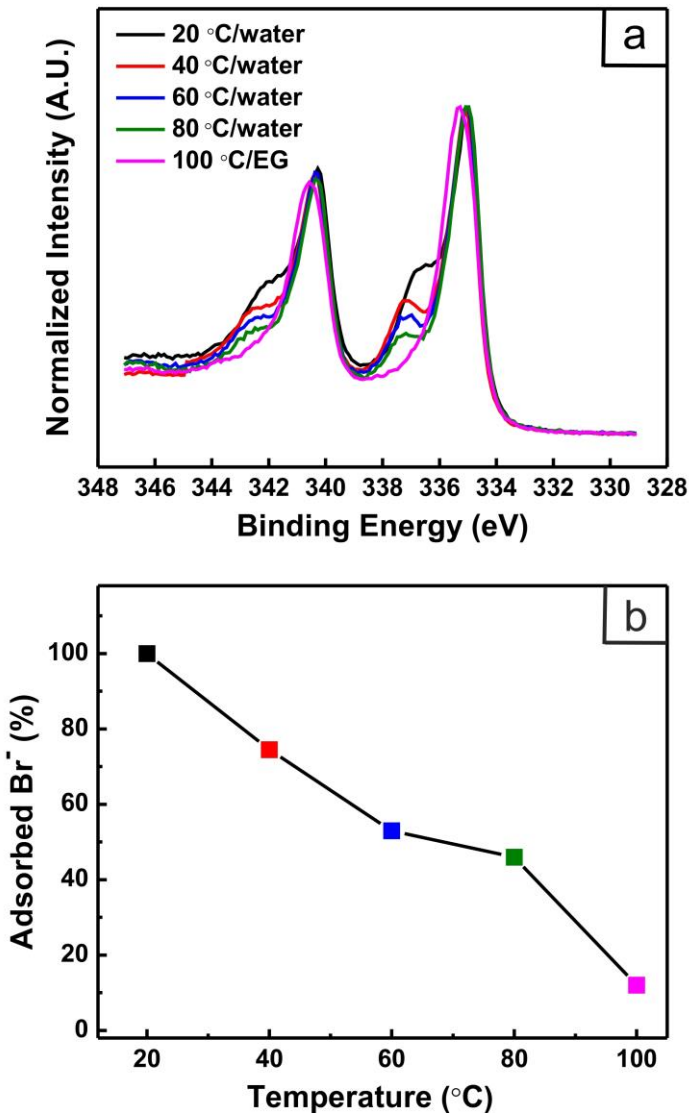

Figure 2.4. (a) XPS spectra of Pd 3d and (b) ICP-MS analysis of residual Br^- ions for the Pd nanocubes after they had been subjected to aging in water or ethylene glycol at different temperatures for 18 h. (Reprinted with permission from [32]. Copyright 2013 American Chemical Society.)

excluding the possibility of the replacement of Pd-Br complex with citrate. Combining the results from XPS and ICP-MS, it can be concluded that the desorption of Br^- ions from the {100} facets of Pd nanocubes can be described by the following reaction:

$$Pd(II)\text{-}Br^- + 2\ e^- \rightarrow Pd(0) + Br^- \qquad (2.1)$$

Interestingly, when the Br^--free nanocubes were aged in an aqueous KBr solution (10 mM) under air, the Br^- ions were found to adsorb onto the surface of Pd nanocubes again. In contrast, there were no detectable Br^- ions on the surface of the nanocubes when the aging was conducted under N_2 atmosphere (Figure 2.5). The results suggest that the Br^- ions could only bind to Pd{100} facets in the presence of O_2 by driving reaction (2.1) in the reverse direction.

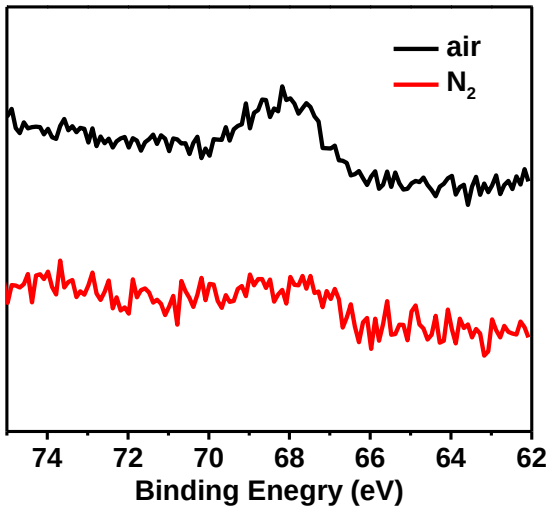

Figure 2.5. Br 3d XPS spectra taken from the Br^--free 18-nm Pd nanocubes after they had been subjected to aging in aqueous KBr solution (10 mM) under air or N_2 atmosphere for 3h. (Reprinted with permission from [32]. Copyright 2013 American Chemical Society.)

The role played by Br^- ions in the nanocube synthesis is generally considered to involve selective adsorption onto the Pd{100} facets, thus stabilizing these facets. The slower growth rate along [100] eventually leads to the formation of cubes enclosed by {100} facets. To validate this mechanism, another set of experiments were conducted based on a previously established protocol [30], in which the Pd nanocubes of 18 nm in edge length were used as seeds for further growth of Pd in the presence of formaldehyde. By varying the amount of Pd precursor, I obtained nanocrystals with different proportions of {100} and {111} facets, including truncated cubes, cuboctahedrons, truncated octahedrons, and octahedrons (Figure 2.6). As illustrated in Figure 2.7a, the proportion of {100} facets gradually decreased during the overgrowth. Taking cuboctahedron as an example, the proportion of {100} facets is only 50% of that for the cubic seed. At the stage of a perfect octahedron, since it is completely enclosed by {111} facets, ideally there should be no {100} facets exposed on the surface. Figure 2.7b shows the Pd 3d XPS spectra of the Pd nanocrystals sampled at different stages of the growth. The results reveal that the shoulder peaks diminished during the growth process and eventually disappeared in the Pd octahedrons. As discussed above, the shoulders of Pd peaks can be attributed to the chemisorption of Br^- ions, and thus the drop in intensity for these shoulder peaks indicates that the Br^- ions gradually desorbed from the surface during the growth process. Furthermore, ICP-MS analysis also showed the same trend of decreasing Br^- ion concentration for the resultant nanocrystals during the shape evolution (Figure 2.7c). The amount of Br^- for cuboctahedrons was around 60% of that for cubes, which is more or less consistent with the fraction of {100} surfaces from the calculation (50%) based on their models. It is worth noting that the octahedrons still contained 20% of the

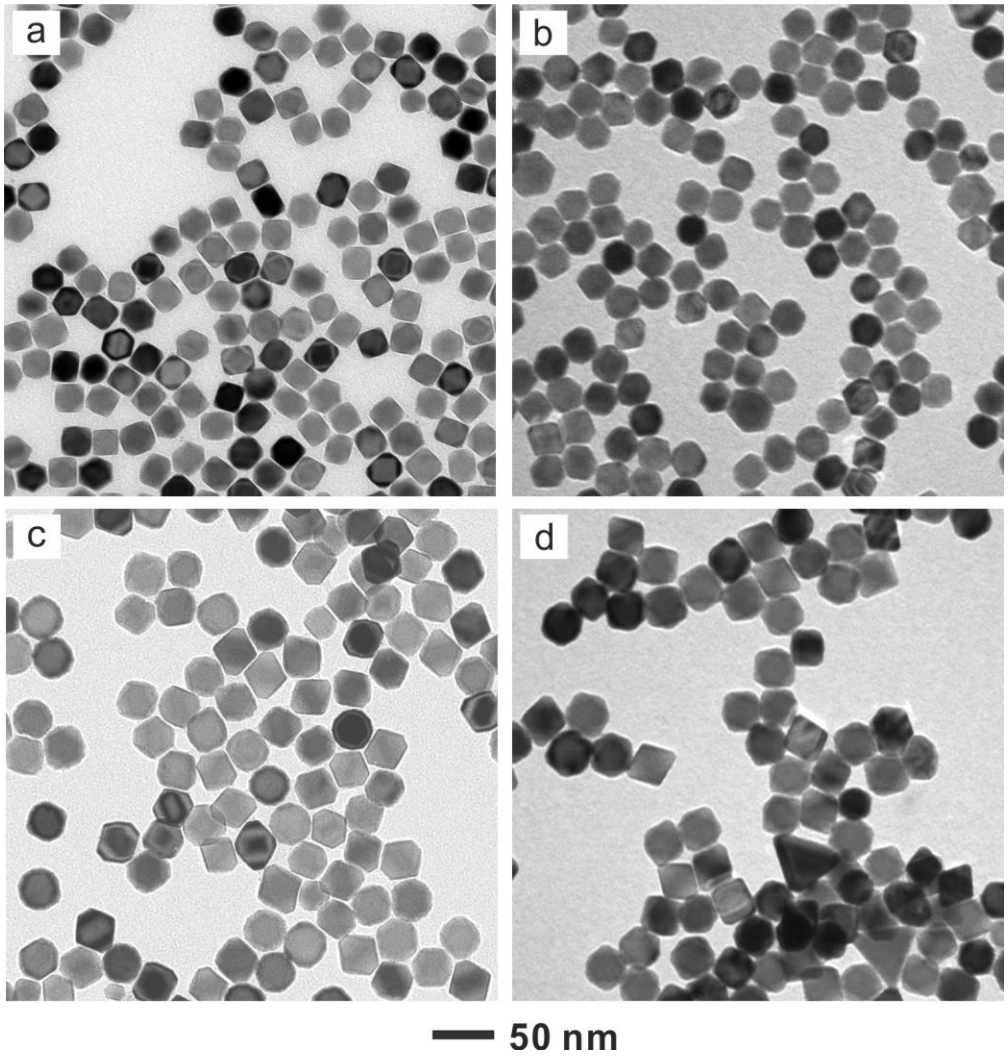

Figure 2.6. TEM images of Pd nanocrystals with different shapes: (a) truncated cubes, (b) cuboctahedrons, (c) truncated octahedrons, and (d) octahedrons. (Reprinted with permission from [32]. Copyright 2013 American Chemical Society.)

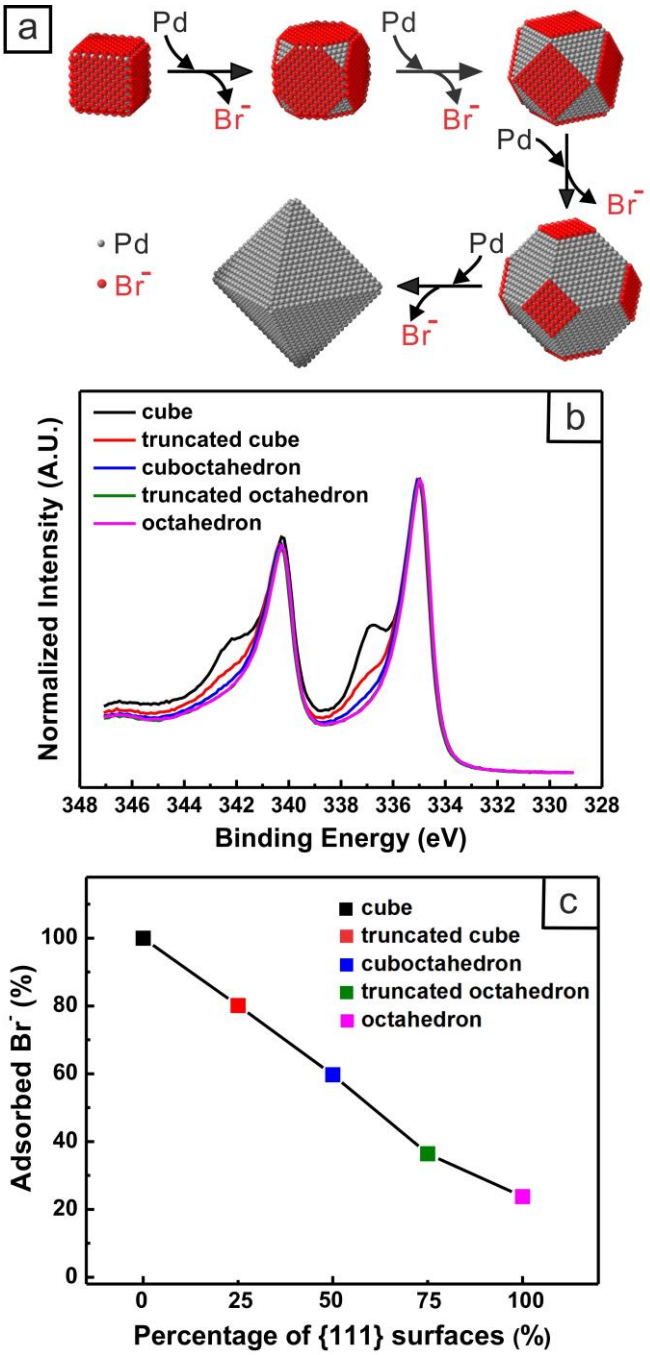

Figure 2.7. (a) Schematic illustration of the Br^- desorption along with the Pd overgrowth on Pd{100} surfaces. (b) Pd 3d XPS spectra and (c) ICP-MS analysis of the residual Br^- ions at different growth stages, showing that the Br^- ions desorbed from Pd {100} surfaces during the Pd overgrowth. (Reprinted with permission from [32]. Copyright 2013 American Chemical Society.)

Br^- ions initially adsorbed on the surface of Pd cubic seeds. This could be attributed to the slight truncation of the vertices of an octahedron during the centrifugation process, which would create newly exposed {100} facets to trap some Br^- ions.

As noted earlier, in a typical synthesis of Pd nanocrystals, the shape of the resultant nanocrystals could be controlled by introducing different capping agents. Because of the preferential adsorption of Br^- onto the Pd {100} facets, it is expected that the introduction of Br^- ions would favor the formation of Pd nanocrystals enclosed mainly by {100} facets, such as truncated cubes and cubes, depending on the concentration of Br^- ions. However, use of Br^- ions at a high concentration could lead to an increase for the particle size due to the formation of a more stable $[PdBr_4]^{2-}$ complex via ligand exchange between $[PdCl_4]^{2-}$ and the excess Br^- ions. Since $[PdBr_4]^{2-}$ has a higher stability constant [31], the reduction rate would be slower and thus the number of seeds generated in the initial stage would be reduced. As a result, the development of a protocol to control the shape while maintaining the size of the nanocrystals would be highly desired. On the basis of the coverage density of Br^- ions on Pd{100} facets acquired from ICP-MS, I designed a set of experiments to demonstrate the quantitative role of Br^- ions in controlling the evolution of Pd nanocrystals into nanocubes. Figure 2.8a schematically illustrates how to control the shape of Pd nanocrystals experimentally by controlling the amount of Br^- ions. First, a control synthesis was conducted in the absence of Br^- ions. As expected, due to the lack of capping agent, Pd cuboctahedrons with a mean size of 5.7 nm were obtained (Figure 2.8b). Next, with information about the amount of Pd precursor, the yield of Pd, the ratio of Br^- ions adsorbed on the Pd{100} surface, and the resultant particle size, the critical amount of Br^- ions needed to cover the entire Pd{100}

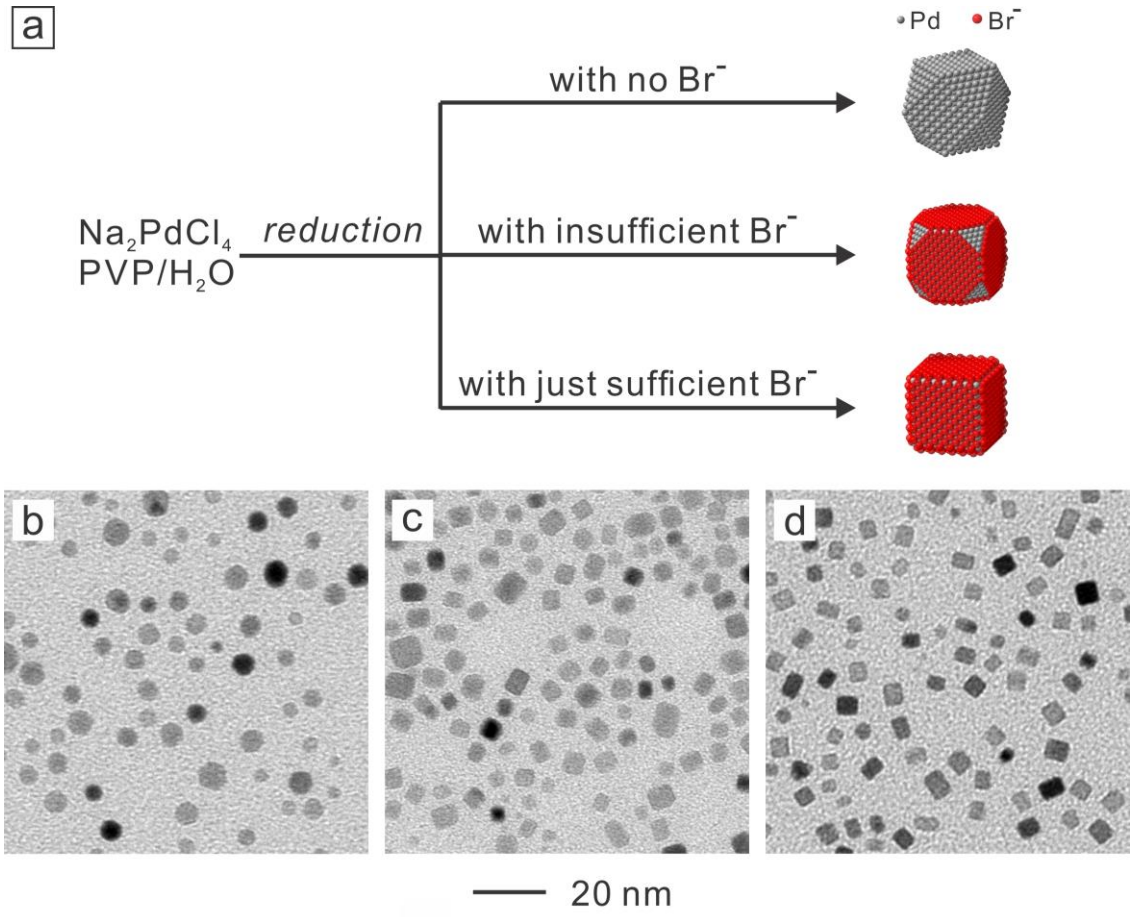

Figure 2.8. (a) A schematic showing how the shape of a Pd nanocrystal can be controlled by adding a specific amount of Br^- ions into the solution as a capping agent for the Pd{100} facets. (b–d) TEM images of Pd nanocrystals synthesized with different amounts of Br^- ions: (b) no Br^- was added, (c) in the presence of insufficient Br^-, and (d) with a sufficient amount of Br^- added. The shape evolution of Pd nanocrystals was clearly observed from (b) cuboctahedron to(c) truncated cube and (d) cube. (Reprinted with permission from [32]. Copyright 2013 American Chemical Society.)

facets can be estimated. When the amount of Br^- ions introduced into the synthesis was less than the estimated critical value, the exposed Pd{100} surfaces could not be fully stabilized by the Br^- ions, resulting in the formation of truncated cubes with some {111} facets on the surface (Figure 2.8c). When the amount of Br^- ions was further increased to exceed the critical value, I obtained perfect Pd nanocubes fully covered by {100} facets, as shown in Figure 2.8d. These results show that the degree of truncation of nanocubes can be tightly controlled by introducing a particular amount of Br^- ions into the synthesis. Moreover, it is worth noting that the average sizes of these three types of Pd nanocrystals were very close (5.7 nm for the cuboctahedrons, 6.0 nm for the truncated cubes, and 5.9 nm for the perfect nanocubes, respectively). The reason for this result was that the ratio of Br^- ions to Pd precursor in the last synthesis was around 0.15, just slightly higher than the critical value. In comparison, the conventional protocol for nanocube synthesis involves the use of an excess amount of Br^- ions, with typical ratios in the range of 0.22−25.8 [5, 21]. The relatively low concentration of Br^- ions involved in the new protocol effectively minimizes the kinetic effect caused by the ligand exchange, helping keep the resultant particles at a similar size.

2.3 Summary

In summary, I have demonstrated a new strategy for quantitatively analyzing the role played by Br^- ions in the synthesis of Pd nanocrystals using a combination of XPS and ICP-MS. From the atomic ratio of Br^- ions to Pd atoms obtained from ICP-MS analysis, the coverage density of Br^- ions on the Pd{100} facets was found to be *ca.* 10 ions/nm^2 for Pd nanocubes of three different sizes. The chemisorbed Br^- ions could be removed

from the surface through desorption at an elevated temperature under reducing conditions, as confirmed by the drop in XPS peak intensity for Pd(II) species. The adsorbed Br^- ions could also be released from the surface by decreasing the proportion of {100} facets during the growth of Pd nanocubes, which also confirmed the selective adsorption of Br^- ions on Pd{100} rather than {111} facets. Moreover, the quantitative information about the coverage density of Br^- ions allowed me to estimate the amount of Br^- ions needed to generate Pd nanocrystals with specific proportions of {100} and {111} facets. I believe this approach based on a combination of XPS and ICP-MS can be extended to other systems for a systematic study of the explicit roles played by various capping agents in the shape-controlled synthesis of nanocrystals.

2.4 Experimental Methods

Chemicals and Materials. Ethylene glycol was purchased from J. T. Baker. Sodium tetrachloropalladate(II), ascorbic acid, citric acid, formaldehyde, poly(vinyl pyrrolidone) ($M_W \approx 55{,}000$), potassium chloride, and potassium bromide were all purchased from Sigma-Aldrich. All chemicals were used as received without further purification. Deionized water with a resistivity of 18.2 MΩ·cm was used for preparing all aqueous solutions.

Synthesis of Pd Nanocubes with Various Sizes. The Pd nanocubes with three different edge lengths of 7.5, 10.5, and 18 nm were synthesized using a recently reported protocol with minor modifications [5]. In a typical synthesis, 8 mL aqueous solution containing PVP (105 mg), AA (60 mg), and different amounts of KBr and KCl were added into a 20 mL vial. The solution was pre-heated at 80 °C for 5 min before the addition of 3 mL Na_2PdCl_4 aqueous solution (64.6 mM). The addition of KBr and KCl in the following amounts gave the nanocubes with edge lengths of 7.5 nm (75 mg of KBr

and 141 mg of KCl), 10.5 nm (300 mg of KBr), and 18 nm (600 mg of KBr), respectively. Each reaction was then allowed to proceed at 80 °C for 3 h. After the removal of excess PVP and KBr/KCl by centrifuging and washing four times with water, the final product was dissolved with concentrated HNO_3 for the ICP-MS analysis.

Synthesis of Pd Nanocrystals with Different Shapes. The Pd nanocrystals with different shapes, including truncated cube, cuboctahedron, truncated octahedron, and octahedron, were synthesized based on a previously established protocol [30]. Typically, 0.3 mL of an aqueous suspension of the 18-nm Pd nanocubes (1.8 mg/mL in concentration) and 8 mL of an aqueous solution containing PVP (105 mg) and HCHO (100 μL) were added into a 20 mL vial. After the mixture of reagents had been heated at 60 °C for 10 min, 3 mL of aqueous solution containing different amounts of Na_2PdCl_4 was introduced. With the increase of the amount of Na_2PdCl_4, the shape of resultant Pd nanocrystals evolved from nanocubes to truncated cubes (5.8 mg), cuboctahedrons (8.7 mg), truncated octahedrons (17.4 mg), and octahedrons (29.0 mg). The reaction mixture was then allowed to proceed at 60 °C for 3 h. During the entire synthesis, the vial was capped except during the addition of reagents. The product was collected by centrifuging and washing with DI water four times before further characterization.

Synthesis of Pd Nanocrystals with the Introduction of a Specific Amount of Br^- Ions. In a standard synthesis, 4 mL aqueous solution containing PVP (53 mg), AA (30 mg), and different amounts of KBr (0 mg for the control synthesis, 0.87 mg for the truncated cubes, 1.75 mg for the perfect cubes, respectively) were added into a 20 mL vial. The solution was pre-heated at 40 °C for 5 min. Next, 1.5 mL of an aqueous solution containing Na_2PdCl_4 (28.5 mg) was added. The reaction mixture was allowed to proceed at 40 °C for 2 h. During the entire synthesis, the vial was capped except during the addition of reagents. After centrifuging and washing with DI water three times, the samples were characterized by transmission electron microscopy. Note that the minimum amount of Br^- for capping all the Pd{100} facets was calculated based on the coverage

density and the critical value of KBr was found to be 1.74 mg for this protocol.

Removal of Chemisorbed Br^- Ions from the Surface of Pd Nanocubes. Removal of surface-chemisorbed Br^- ions was conducted for the 18-nm Pd nanocubes under a mild reductive condition. Typically, 0.2 mL of an aqueous suspension of the 18-nm Pd nanocubes was introduced into 3 mL DI water or EG containing PVP (30 mg) and CA (30 mg) hosted in a vial and then capped. The mixtures were then aged at different temperatures for 18 h. After centrifuging and washing with water three times, the product was collected for further analysis.

Characterization. The TEM images were taken using a JOEL (JEM-1400) microscope operated at 120 kV. The samples for TEM analysis were prepared by drying a drop of the nanocrystals suspension onto carbon-coated copper grids. The XPS data were collected using Thermo K-Alpha photoelectron spectrometer with an Al Kα source. The samples for ICP-MS analysis were prepared by dissolving the nanocrystals with concentrated HNO_3 and further diluted with 1% HNO_3 solution to a level of 100 ppb.

Calculation of the Br^- Ion Coverage Density on the Pd{100} Facets and the Br^- to Surface Pd Atom Ratio. Based on the ratio of Br^- ions to all Pd atoms obtained from ICP-MS analysis, the Br^- ion coverage density was calculated according to the equation:

$$\frac{Br^-}{total\ Pd} = \frac{Pd\ cube\ surface\ area\ (nm^2) \times Br^-\ coverage\ density\ \left(\frac{ions}{nm^2}\right)}{number\ of\ Pd\ atoms\ per\ cube}$$

$$= \frac{6 \cdot l^2 \cdot \phi_{Br}}{4 \cdot \left(\frac{l^3}{a^3}\right)}$$

$$= \frac{3}{2} \cdot \frac{a^3 \cdot \phi_{Br}}{l}$$

Rearranging the equation gives

$$\phi_{Br} = \frac{2}{3} \cdot \frac{l}{a^3} \cdot \left(\frac{Br^-}{total\ Pd}\right)$$

Where l is the average edge length of Pd nanocubes (7.5 nm, 10.5 nm, or 18 nm); a is the lattice constant of Pd (0.389 nm); and ϕ_{Br} is the Br^- coverage density. It is worth pointing out that the sub-10-nm Pd nanocubes prepared using the present protocols generally have a rectangle cross section with an aspect ratio of 1.0−1.2. As a result, the average edge length of nanocubes was used to minimize the effect of variation in edge length for the calculation.

With the information of Br^- ion coverage density, the ratio between Br^- ions to surface Pd atoms was calculated by the following equation:

$$\frac{Br^-}{surface\ Pd} = \frac{Pd\ cube\ surface\ area\ (nm^2) \times Br^-\ coverage\ density\ \left(\frac{ions}{nm^2}\right)}{number\ of\ Pd\ atoms\ on\ the\ surface\ of\ cube}$$

$$= \frac{6 \cdot l^2 \cdot \phi_{Br}}{6 \cdot \left[2 \cdot \left(\frac{l^2}{a^2}\right)\right]}$$

$$= \frac{a^2 \cdot \phi_{Br}}{2}$$

Calculation of the Amount of Br^- Ions Needed for Generating Perfect Pd Nanocubes. Based on the Br^- ion coverage density information, the minimum ratio between Br^- ions to Pd precursor molecules for generating perfect Pd nanocubes was calculated according to the following equation:

$$\frac{Br^- \cdot \varphi_{Br}}{(total\ Pd) \cdot \varphi_{Pd}} = \frac{3}{2} \cdot \frac{a^3 \cdot \phi_{Br}}{l}$$

Where l is the particle size (6 nm) of Pd nanocrystals involved in the control synthesis (with no Br^-); φ_{Br} and φ_{Pd} are the yield of Pd (98.4%) and the ratio of Br^- ions adsorbed on the Pd surface (95.3%) under this experimental condition as determined by ICP-MS; amount of Pd precursor used in the synthesis was 0.0969 mmol (28.5 mg of Na_2PdCl_4); and ϕ_{Br} is the Br^- coverage density determined in this work: ~10 ions/nm^2. By plugging

these parameters into the equation, the critical value of Br^- ions was found to be 0.0146 mmol or 1.74 mg of KBr.

2.5 Notes to Chapter 2

Part of this chapter is adapted from the paper "Quantitative analysis of the coverage density of Br^- ions on Pd{100} facets and its role in controlling the shape of Pd nanocrystals" published in *Journal of the American Chemical Society* [32].

2.6 References

[1] Doyle, A. M.; Shaikhutdinov, S. K.; Jackson, S. D.; Freund, H.-J. *Angew. Chem., Int. Ed.* **2003**, *42*, 5240−5243.

[2] Bhattacharjee, S.; Dotzauer, D. M.; Bruening, M. L. *J. Am. Chem. Soc.* **2009**, *131*, 3601−3610.

[3] Schauermann, S; Nilius, N.; Shaikhutdinov, S.; Freund, H.-J. *Acc. Chem. Res.* **2003**, *42*, 1673−1681.

[4] McClure, S. M.; Goodman, D. W. *Chem. Phys. Lett.* **2009**, *469*, 1−13.

[5] Jin, M.; Liu, H.; Zhang, H.; Xie, Z.; Liu, J.; Xia, Y. *Nano Res.* **2011**, *4*, 83−91.

[6] Freund, H.-J.; Meijer, G.; Scheffler, M.; Schlögl, R.; Wolf, M. *Angew. Chem., Int. Ed.* **2011**, *50*, 10064−10094.

[7] Kim, S.-W.; Kim, M.; Lee, W. Y.; Hyeon, T. *J. Am. Chem. Soc.* **2002**, *124*, 7642−7643.

[8] Doucet, H.; Hierso, J.-C. *Angew. Chem., Int. Ed.* **2007**, *46*, 834−871.

[9] Moreno-Mañas, M.; Pleixats, R. *Acc. Chem. Res.* **2003**, *36*, 638−643.

[10] An, K.; Somorjai, G. A. *ChemCatChem* **2012**, *4*, 1512−.

[11] Zhang, H.; Jin, M.; Xiong, Y.; Lim, B.; Xia, Y. *Acc. Chem. Res.* **2013**, *46*, 1783−1794.

[12] Tao, A. R.; Habas, S.; Yang, P. *Small* **2008**, *4*, 310−325.

[13] Lim, B.; Jiang, M.; Tao, J.; Camargo, P. D. C.; Zhu, Y.; Xia, Y. *Adv. Funct. Mater.* **2009**, *19*, 189−200.

[14] Huang, X.; Tang, S.; Zhang, H.; Zhou, Z.; Zheng, N. *J. Am. Chem. Soc.* **2009**, *131*, 13916−13917.

[15] Niu, W.; Zhang, L.; Xu, G. *ACS Nano* **2010**, *4*, 1987−1996.

[16] Langille, M. R.; Personick, M. L.; Zhang, J.; Mirkin, C. A. *J. Am. Chem. Soc.* **2012**, *134*, 14542−14554.

[17] Xie, S.; Lu, N.; Xie, Z.; Wang, J.; Kim, M. J.; Xia, Y. *Angew. Chem., Int. Ed.* **2012**, *51*, 10266−10270.

[18] Chiu, C.-Y.; Li, Y.; Ruan, L.; Ye, X.; Murray, C. B.; Huang, Y. *Nat. Chem.* **2011**, *3*, 393−399.

[19] Chen, M.; Wu, B.; Yang, J.; Zheng, N. *Adv. Mater.* **2012**, *24*, 862−879.

[20] Zhang, Y.; Grass, M. E.; Kuhn, J. N.; Tao, F.; Habas, S. E.; Huang, W.; Yang, P.; Somorjai, G. A. *J. Am. Chem. Soc.* **2008**, *130*, 5868−5869.

[21] Xiong, Y.; Cai, H.; Wiley, B. J.; Wang, J.; Kim, M. J.; Xia, Y. *J. Am. Chem. Soc.* **2007**, *129*, 3665−3675.

[22] Sun, Y.; Zhang, L.; Zhou, H.; Zhu, Y., Sutter, E.; Ji, Y.; Rafailovich, M. H.; Sokolov, J. C. *Chem. Mater.* **2007**, *19*, 2065−2070.

[23] Zhang, Q.; Moran, C. H.; Xia, X.; Rycenga, M.; Li, N.; Xia, Y. *Langmuir* **2012**, *28*, 9047−9054.

[24] Zou, S.; Gao, X.; Weaver, M. J. *Surf. Sci.* **2000**, *452*, 44−57.

[25] Lim, B.; Kobayashi, H.; Camargo, P. H. C.; Allard, L. F.; Liu, J.; Xia, Y. *Nano Res.* **2010**, *3*, 180−188.

[26] Lavrich, D. J.; Wetterer, S. M.; Bernasek, S. L.; Scoles, G. *J. Phys. Chem. B* **1998**, *102*, 3456−3465.

[27] Xia, Y.; Xiong, Y.; Lim, B.; Skrabalak, S. E. *Angew. Chem., Int. Ed.* **2009**, *48*,

60−103.

[28] Voogt, E. H.; Mens, A. J. M.; Gijzeman, O. L. J.; Geus, J. W. *Surf. Sci.* **1996**, *350*, 21−31.

[29] Qiu, L.; Liu, F.; Zhao, L.; Yang, W.; Yao, J. *Langmuir* **2006**, *22*, 4480−4482.

[30] Jin, M.; Zhang, H.; Xie, Z.; Xia, Y. *Energy Environ. Sci.* **2012**, *5*, 6352−3657.

[31] Feldberg, S.; Klotz, P, Newman, L. *Inorg. Chem.* **1972**, *11*, 2860−2865.

[32] Peng, H.-C.; Xie, S.; Park, J.; Xia, X.; Xia, Y. *J. Am. Chem. Soc.* **2013**, *135*, 3780−3783.

CHAPTER 3

THE EFFECT OF SURFACE CAPPING ON THE HETEROGENEOUS NUCLEATION AND GROWTH OF PALLADIUM NANOCYSTALS IN A SEED-MEDIATED SYNTHESIS

3.1 Introduction

In addition to the conventional one-pot synthesis, seed-mediated growth that involves the reduction of a precursor in the presence of pre-formed seeds has been actively explored for generating nanocrystals with diversified but well-controlled sizes, shapes, and internal structures [1]. It also allows one to better understand and control the shape of metal nanocrystals by avoiding the complicated, poorly understood self-nucleation process. Significantly, thanks to recent developments in electron microscopy and elemental mapping techniques, it is now feasible to resolve changes to the seeds due to growth by comparing the products sampled at different stages of a synthesis. Through the use of seeds with a well-defined internal structure, one could systematically examine the roles of various thermodynamic and kinetic parameters in controlling the evolution of seeds into nanocrystals with distinctive shapes.

As discussed in Chapter 1.2.1, introducing a surface capping agent to selectively passivate certain facets on the surface of a growing seed offers a promising strategy for preparing nanocrystals with new shapes or morphologies [2−6]. For Pd nanocrystals, a number of different capping agents have been identified and validated for controlling their geometric shapes. Notable examples include halide ions (Br^- and I^-) for Pd(100) and CO for Pd(111) surfaces [7−11], as well as some biological molecules that have been shown with distinctive abilities to passivate different types of Pd surfaces [12−14]. Despite these successful demonstrations, there is still an urgent need to resolve the

explicit roles played by a surface capping agent in affecting the deposition probability of atoms and thus the growth pattern of a seed in a seed-mediated growth synthesis.

In this work, I conducted a set of experiments based on the overgrowth of Pd on Pd seeds to demonstrate that the collision model commonly used in surface science can still be applied to seed-mediated growth of nanocrystals to account for the growth pattern of a seed in the presence or absence of a capping agent. A monometallic system was chosen for this study to rule out the possible impacts of other factors, such as lattice mismatch and difference in cohesive energy between the two metals in a bimetallic system that may result in preferential deposition at certain sites [15, 16]. Also, as demonstrated in Chapter 2, the chemisorbed Br^- ions could be readily removed from the surface of Pd nanocubes through thermally induced desorption under a reductive condition [17]. By depositing Pd atoms onto Pd cubic seeds (with or without chemisorbed Br^- ions) and carefully monitoring their morphological changes, I demonstrate that the surface condition of a seed indeed plays the key role in determining the probability of atom deposition, as well as the growth mode or pattern of the seed. In addition, by facilitating the surface diffusion of Pd adatoms, the deposition of Pd on the (100) surface of a Pd cubic seed could be switched from an island growth mode to a layered growth mode. The collision model could be further extended to explain the growth of other types of Pd seeds whose surfaces are covered by a mix of {111} and {100} facets in different proportions or characterized by different internal structure, including cuboctahedrons and penta-twinned nanowires.

3.2 Results and Discussion

Figure 3.1a schematically illustrates how an atom newly formed in the solution would interact with the surface of a seed. According to the collision model that has long been established in surface science to account for the interactions between atoms (or molecules) and the surface of a bulk substrate, the atom is supposed to collide with the surface and then take different possible pathways [18]. Specifically, when the atom

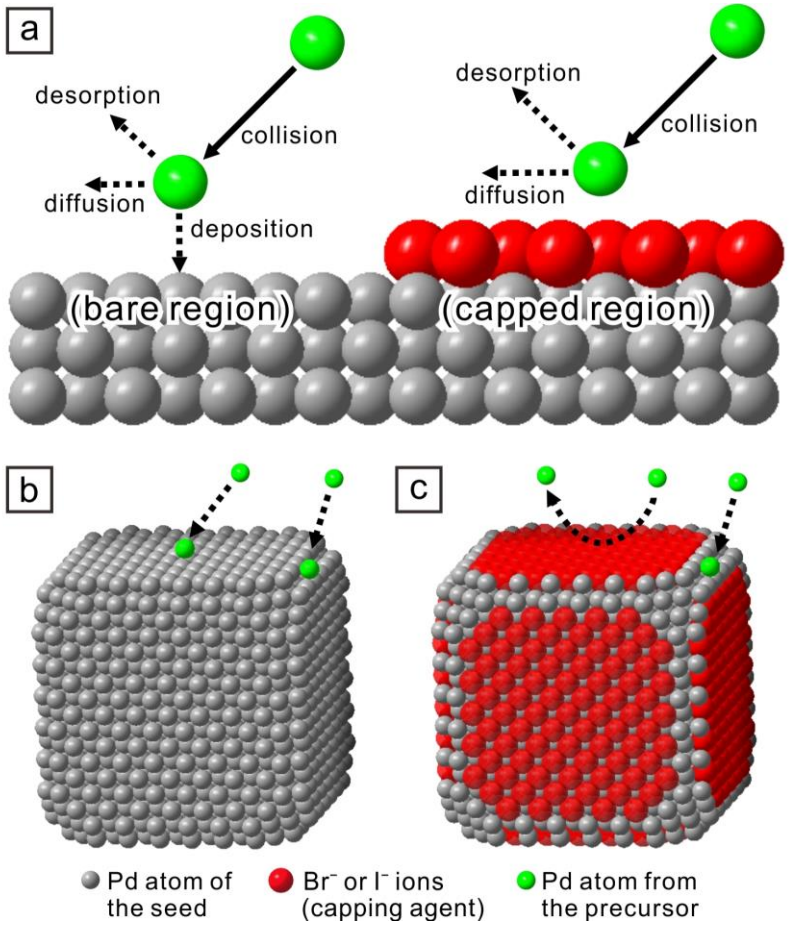

Figure 3.1. Schematic illustrations of (a) different options for a newly formed Pd atom upon its collision with the bare and capped regions on a seed, respectively, and (b, c) anticipated growth pathways for a Pd cubic seed in the (b) absence and (c) presence of halide capping agent for the {100} facets.

approaches the surface, it will be trapped on the surface through physical adsorption. In general, there are three options with a sum of unity for a physisorbed atom, including deposition, migration, and desorption. Specifically, when an atom strikes the bare region on the surface of a seed where there is no capping agent, it has a probability of f_{dep} to be permanently deposited through the formation of bonds with atoms on the surface. At the same time, it has a probability of f_{des} to desorb from the surface, together with a

probability of f_{dif} to diffuse to a neighboring site followed by choosing an option again of whether to deposit, diffuse, or desorb. The overall probability, f_0, for the atom to be deposited on the bare region is therefore the sum of the deposition probability at the initial site, and the probability of diffusing from the initial site and then depositing to the second site, and so on.

In comparison, the option of deposition will not be available if the atom strikes a region capped and thus passivated by a capping agent. As a consequence, the incident atom simply bounces off from the surface and return to the solution (with a probability of f'_{des}) or diffuse to another sites on the surface (with a probability of f'_{dif}), with no deposition on the capped region. Collectively, the overall probability for an atom to be deposited on a surface can be considered as the outcome of multiple competing processes and strongly depends on the surface condition, including the presence of a capping agent and its coverage density. For a surface that is partially passivated by a capping agent with a coverage density of θ, the probability, f_θ, for the deposition of an atom can be calculated using the following equation:

$$f_\theta = f_0 \left[1 + \frac{f'_{des}}{f_{dep}+f_{des}} \cdot \frac{\theta}{1-\theta}\right]^{-1} \qquad (3.1)$$

where the value of θ varies between 0 (a bare surface) to 1 (a completely capped surface); f_0 is the probability for an atom to be deposited on a completely bare surface when the coverage of capping agent is zero.

By applying the collision model to a seed-mediated growth process, it is expected that the presence of a capping agent will result in different growth patterns for the capped and bare regions on the surface of a seed. For a model system involving cubic seeds, Figure 3.1, b and c, shows the different patterns for atom deposition in the absence and presence of capping agent, respectively. When there is no capping agent on the surface of a cubic

seed, the entire surface can serve as nucleation sites for the deposition of atoms (Figure 3.1b). As a result, the newly formed atoms have a high probability to be deposited randomly on the side faces, corners, and edges. In comparison, if the side faces of a cubic seed are passivated by a chemisorbed capping agent, deposition of atoms on these regions will not be allowed, confining the deposition exclusively to the corners and edges (Figure 3.1c).

It should be noted that the proposed collision model for seed-mediated growth is based on the generally accepted argument that the metal precursor is firstly reduced to atoms in the reaction solution and then deposited onto the seed. Alternatively, it is also possible that the precursor compounds adsorb onto the seed and are then reduced to atoms [19]. If this is the case, the interaction between the precursor and capping agent will become a decisive factor in determining the growth pattern of a seed. For example, if their interaction is negligible or even repulsive (*e.g.*, $PdBr_4^{2-}$ and Br^-), it will be less likely that the precursor can adsorb onto the capped region, thus confining the deposition to the bare region of a seed. In comparison, the deposition is expected to primarily occur on the capped region when there is an attractive interaction between the precursor and capping agent (*e.g.*, Ag^+ and Br^-), giving a growth pattern opposite to the one predicted by the collision model. The challenges in investigating the explicit pathway are mainly due to the shortage of experimental instruments capable of *in-situ* monitoring the heterogeneous nucleation process with a satisfying resolution. Nevertheless, it can still be indirectly inferred that the pathway where the precursor is reduced into atoms in the reaction solution prior to the deposition is in dominance for a given synthesis if there is a good agreement between the growth pattern of a seed observed experimentally and the one predicted from the collision model.

The Growth of Pd Cubic Seeds in the Presence/Absence of Capping Agent. To uncover how a surface capping agent will affect the heterogeneous nucleation and overgrowth on a seed, I initially focused on a set of experiments involving the deposition

of Pd atoms on Pd cubic seeds. Figure 3.2a in the Supporting Information shows TEM image of the cubic seeds with an average edge length of 18 nm. Each of the nanocubes is mainly enclosed by six {100} facets as the side faces, together with slight truncation at corners and edges to express {111} and {100} facets, respectively. As a capping agent, the Br^- ions selectively passivate the {100} facets on the cubic seeds but they could be removed from the surface at an elevated temperature under a reductive condition, as evidenced by XPS analysis (Figure 3.2b). The Pd nanocubes, with or without Br^- ions on their {100} facets, were then used as seeds to investigate the heterogeneous nucleation and overgrowth of Pd.

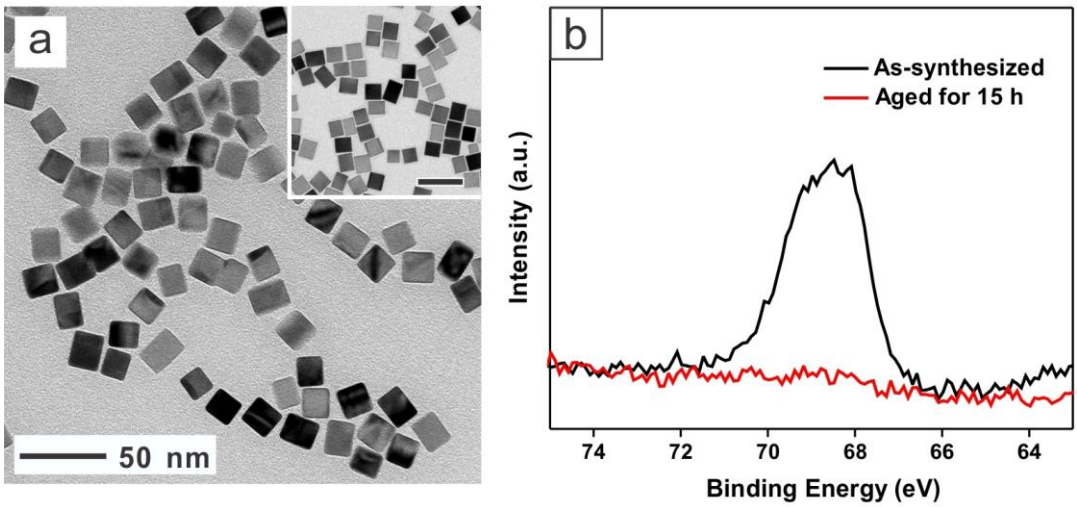

Figure 3.2. (a) TEM images of the 18-nm Pd cubic seeds that had been aged in EG at 120 °C for 15 h to remove the Br^- ions chemisorbed on the surface during the synthesis. The inset shows TEM image of the Pd cubic seeds prior to the treatment, where the scale bar is 50 nm. (b) Br 3d XPS spectra of the Pd cubic seeds before and after the removal of chemisorbed Br^- ions.

The Na_2PdCl_4 precursor solution was introduced into a suspension of the cubic seeds using a syringe pump at a relatively low rate of 0.5 mL/h at room temperature in order to avoid precursor concentration build-up and thereby homogeneous nucleation. Figure 3.3, a−c, shows TEM images of samples obtained at different stages of a synthesis involving Pd cubic seeds with no Br^- ions on the surface. In the early stage when a small amount of the precursor solution was introduced, several islands started to appear on the surface of each cubic seed, indicating heterogeneous nucleation for the newly formed atoms (Figure 3.3a). As the amount of the precursor solution was increased, the number of islands gradually increased and continuously grew into larger sizes, resulting in multiple bumps on the surface of each seed (Figure 3.3, b and c). The bumps were distributed randomly on the surface of a seed, implying that the deposition had no preference in terms of facet on the seed in the absence of a surface capping agent. Considering the lower coordination numbers for atoms on the corners and edges relative to the side faces, the newly formed atoms should have a slightly greater tendency to be deposited onto the corners and edges. In reality, such a preference was compromised by the substantially smaller areas for the corners and edges relative to the side faces, and therefore most of the atoms turned out to be deposited on the side faces because of a much greater collision frequency with the side faces. In comparison, for the cubic seeds whose {100} facets were passivated by the chemisorbed Br^- ions, the deposition of Pd atoms on side faces should be suppressed according to the collision model illustrated in Figure 3.1c. As a result, the newly formed Pd atoms were exclusively deposited on the bare regions without any chemisorbed Br^- ions, including the edges and the corners, leading to the formation of concave nanocubes (Figure 3.3, d−f).

The Role of Surface Diffusion in Determining the Growth Mode. The resultant Pd nanocrystals show two distinctive morphologies with rough and smooth surfaces, respectively, in the absence and presence of chemisorbed Br^- ions. The difference in morphology implies that two different modes could be involved in the growth process. In

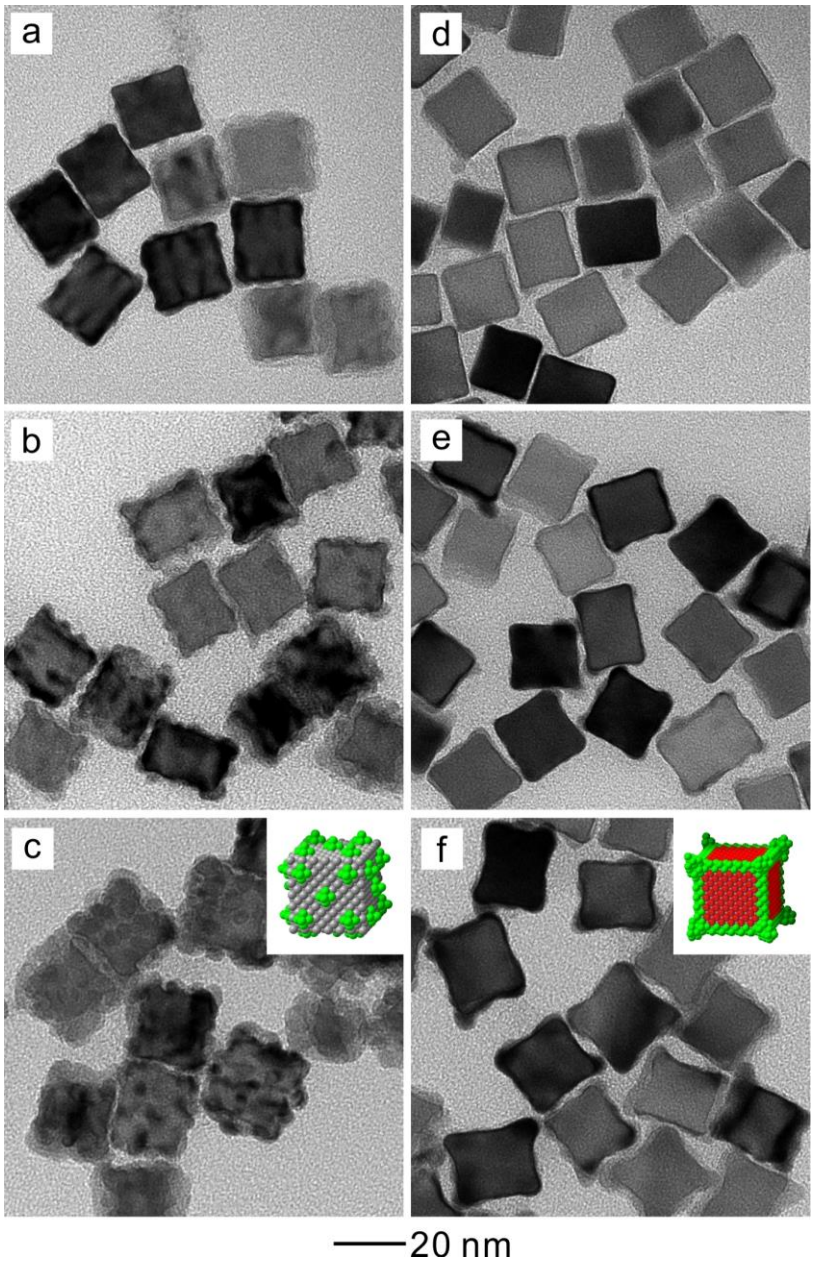

Figure 3.3. TEM images of Pd nanocrystals obtained from the overgrowth of 18-nm Pd cubic seeds in the (a−c) absence and (d−f) presence of Br^- ions chemisorbed on the {100} side faces, as a function of the injected volume of Na_2PdCl_4 solution: (a, d) 0.12 mL, (b, e) 0.36 mL, and (c, f) 0.72 mL. All syntheses were conducted at room temperature. In the schematic models, Br^- ions and the added Pd atoms and are represented by red and green spheres, respectively.

the absence of a capping agent, the surface of resultant nanocrystals was bumpy, corresponding to an island growth pattern, or the Volmer-Weber mode. From thermodynamic perspective, the overgrowth of a metal on a substrate made of the same metal should favor a layered growth pattern, or the Stransky-Krastabov mode, due to the lack of intrinsic difference between the two materials in terms of cohesive energy and lattice constant [18]. The island growth mode for the Br^--free seeds can be understood from the following arguments. Since the newly formed atoms have the probability to be deposited on the entire surface of a seed in the absence of chemisorbed Br^- ions, the initially formed nucleation sites should be separated from each other. In addition, as documented in literature, the activation energy barrier for the diffusion of adatoms on a specific surface is strongly dependent on the surface structure [20, 21]. For an *fcc* metal, the diffusion is typically rapid and occurs with a low energy barrier on the close-packed (111) surface, whereas the diffusion on (100) surface needs to overcome a higher activation energy barrier. Specifically, the surface diffusion on the {100} side faces of a Br^--free cubic seed was too insignificant to induce effective mass transport, and the adatoms tended to stay and accumulate on top of the just-formed nucleation sites, resulting in the island growth mode. In contrast, for the Br^--capped cubic seeds where the atoms were only deposited on the corners and edges with relatively small areas, the distance between individual nucleation sites was relatively short. As a result, the nucleation sites on a Br^--capped seed could easily migrate and merge, leading to the formation of a smooth surface.

Because surface diffusion is a thermally activated process, the migration of adatoms should be a temperature dependent process [22]. Specifically, increasing the reaction temperature will accelerate the surface diffusion rate and thus facilitate the transition of growth mode from island growth to layered growth for the Br^--free seeds. As shown in Figure 3.4a, by increasing the reaction temperature from 20 to 50 °C while keeping other experimental conditions the same, the number of bumps was greatly reduced while the

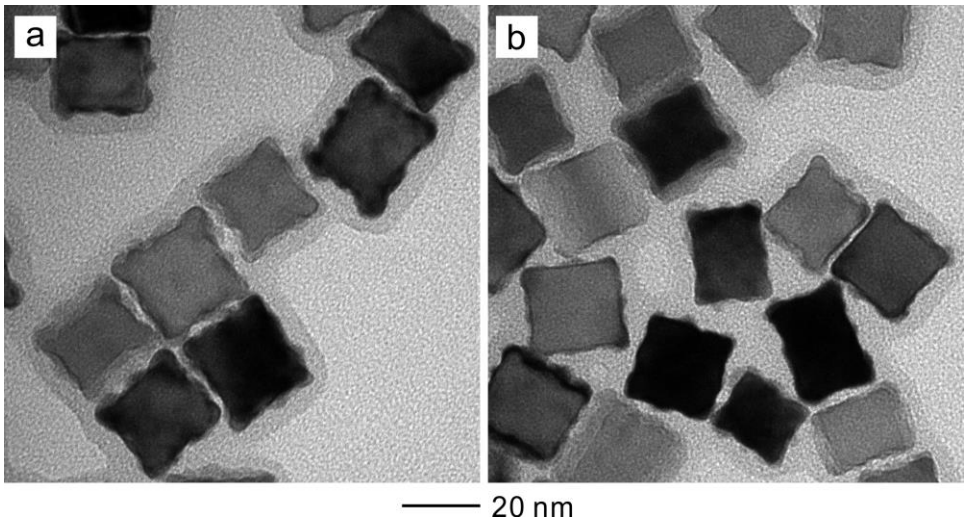

Figure 3.4. TEM images of Pd nanocrystals that were grown from Br^--free Pd cubic seeds using the standard procedure, except for the raise of reaction temperature to (a) 50 °C and (b) 80 °C, respectively.

surface of resultant Pd nanocrystals became smoother compared to those obtained using the standard procedure at 20 °C. When the temperature was further increased to 80 °C, there were only a few bumps on the surface, suggesting the switching of deposition from an island growth mode to a layered growth mode (Figure 3.4b). In this case, the rapid surface diffusion of adatoms at an elevated temperature led to the coalescence between individual nucleation sites and thus a smoother surface. Taken together, these results suggest that an elevated temperature was needed for the adatoms to overcome the relatively higher activation energy barrier for the diffusion on a Pd(100) surface and thus enable a layered growth mode.

The Role of Capping Agent in Determining the Probability of Atom Deposition. I also conducted a synthesis that involves the use of a mixture of the two different types of cubic seeds (Br^--capped and Br^--free) at a 1:1 ratio in order to understand how the presence a capping agent affects the probability of atom deposition. In this case, the

collision frequencies of the atoms with both types of seeds should be essentially the same and thus the number of atoms deposited on a seed directly reflects the overall probability of atom deposition. Thanks to the distinctive growth modes, the corresponding seeds and the nanocrystals could be identified based on their morphologies. As shown in Figure 3.5a, the numbers of concave cubes (products of the Br^--capped seeds) and dendritic nanocubes (product of the Br^--free seeds) are more or less the same, confirming the equal number of the two types of seeds. In this regard, one may expect that the newly formed Pd atoms should have the same probability to be deposited on both types of seeds due to their equivalence in surface area. According to Eq. (3.1), however, the deposition probability for atoms strongly depends on the surface condition and is a function of the coverage density (θ) of surface capping. It is decreased relative to a bare surface whenever the surface of a seed is capped and thus passivated by a capping agent (*i.e.*, $f_\theta \leq f_0$). As a result, the newly formed atoms would not be deposited evenly on both types of seeds, but more onto the Br^--free seeds where there was no capping agent on the surface, as shown in a magnified TEM image (Figure 3.5b). Specifically, for a Br^--capped seed, only those atoms striking the corners and edges of a seed can have the probability to be deposited on the surface, whereas the deposition would be blocked by the chemisorbed Br^- ions. In comparison, the collisions of atoms with the Br^--free seeds can be considered effective over the entire surface due to the lack of a capping agent. Collectively, despite of their equal surface area and thus the same collision frequency, more atoms are expected to be deposited onto the Br^--free seeds due to the presence of a larger bare area with a higher deposition probability. This result implies that that the presence of a capping agent on the surface indeed lowered the overall deposition probability (f_θ) for atoms on a seed. It also validates the efficacy of applying the collision model to explain the deposition probability of atoms and thus the growth pattern of a seed in a seed-mediated synthesis.

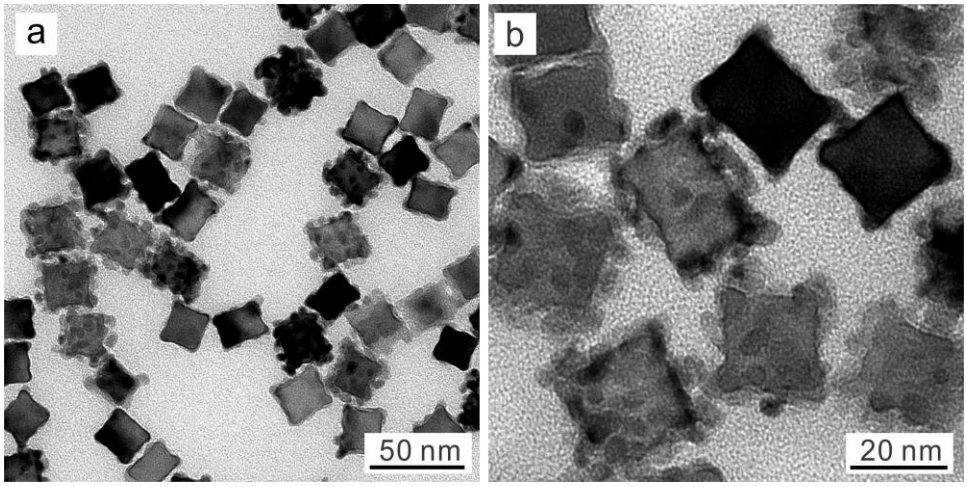

Figure 3.5. TEM images of Pd nanocrystals prepared using the standard procedure except for the use of a 1:1 mixture of Br^--free and Br^--capped 18-nm Pd nanocubes as the seeds and the introduction of 0.36 mL of the Na_2PdCl_4 solution.

Extension from Cubic to Other Types of Seeds with Different Shapes. I also conducted a set of experiments using other types of seeds whose surfaces are enclosed by a mix of {111} and {100} facets in different proportions or characterized by different internal structures. As shown in Figure 3.6a, in contrast to a cubic seed mostly enclosed by {100} facets, a cuboctahedral seed is bound by {111} facets and {100} facets in roughly the same proportion in terms of area. The cuboctahedral seeds were first prepared using a seed-mediated growth approach with the 18-nm Pd cubic seeds whose {100} facets were capped by Br^- ions using a published protocol [23]. Meanwhile, penta-twinned nanowires of Pd were prepared using I^- ions as the capping agent to facilitate the formation of Pd(100) surface (Figure 3.6b). Each of the nanowires is enclosed by five {100} facets and ten {111} facets on its side surfaces and the two ends, respectively. Owing to the selective chemisorption of I^- on Pd(100) surface [10], the side surfaces of nanowires were capped while the edges and ends were free of I^- ions. In order to study the growth patterns of these seeds in the absence of a capping agent, the as-synthesized

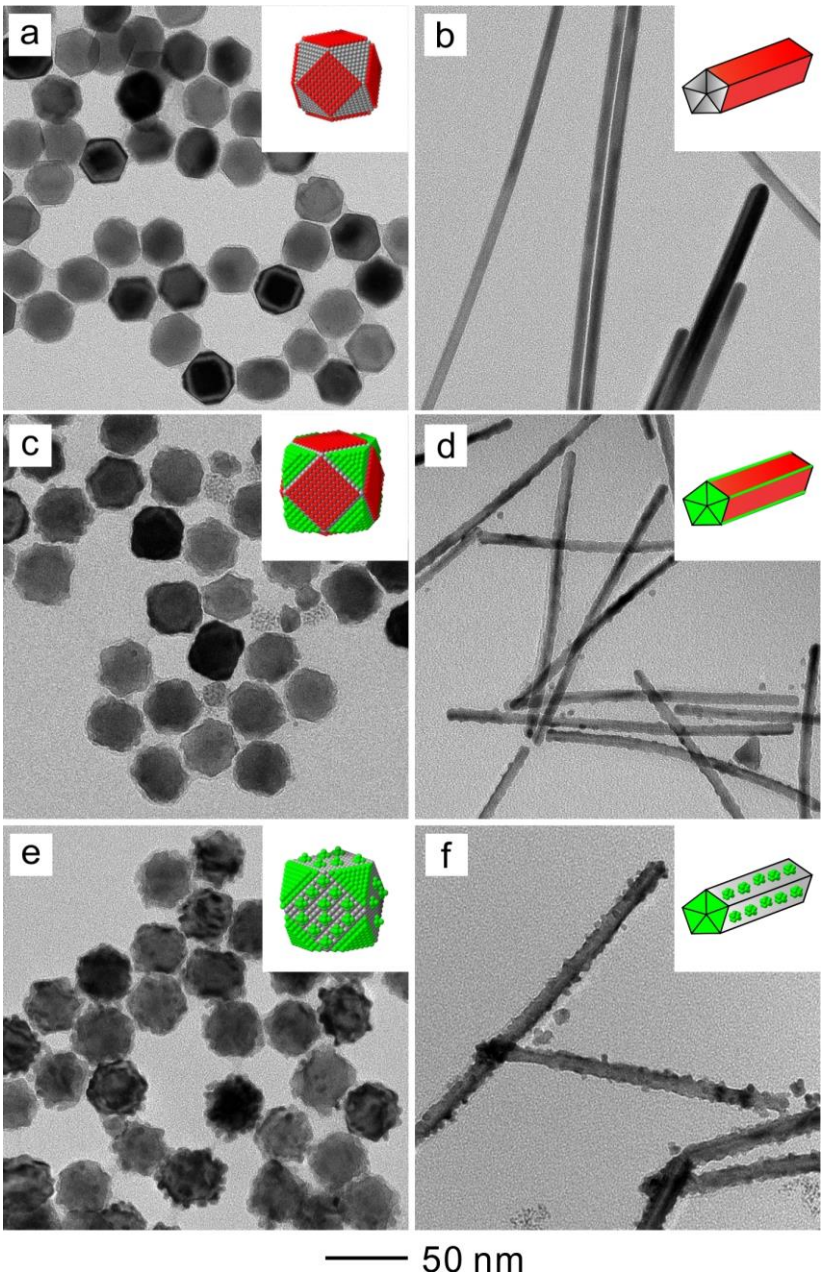

Figure 3.6. TEM images of the as-synthesized (a) cuboctahedrons and (b) penta-twinned nanowires that subsequently served as the seeds. (c–f) TEM images of the resultant Pd nanocrystals obtained using the standard procedure, except for the involvement of different types of seeds: (c) Br^--capped Pd cuboctahedrons, (d) I^--capped Pd nanowires, (e) Br^--free Pd cuboctahedrons, and (f) I^--free Pd nanowires. In the schematic models, the surface capping agents and Pd atoms are denoted by red and green dots, respectively.

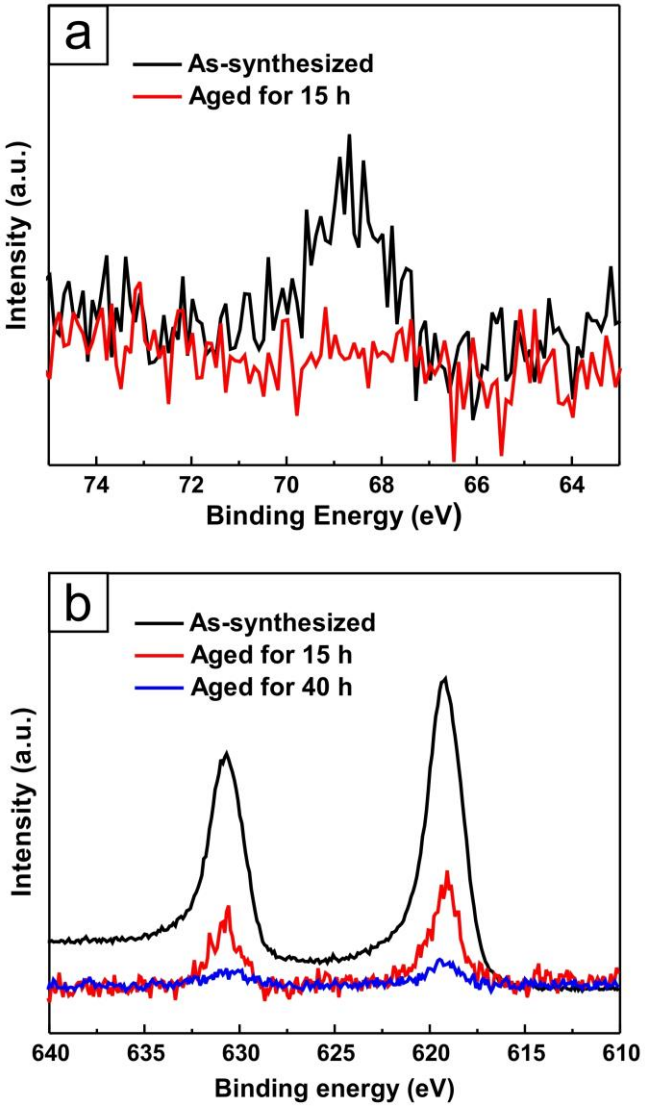

Figure 3.7. (a) Br 3d XPS spectra of the Pd cuboctahedral seeds before and after aging in EG at 120 °C to remove the chemisorbed Br^- ions. (b) I 3d XPS spectra of the Pd nanowire seeds before and after aging in EG at 160 °C for two different intervals of time.

seeds were subjected to aging under a reductive condition at elevated temperatures to remove the capped halide ions. By applying the protocol used to remove the Br^- ions from the surface of nanocubes, Br^--free cuboctahedrons were obtained, as evidenced by the absence of Br 3d peak in the XPS spectrum (Figure 3.7a). However, the same protocol did not work for the removal of the chemisorbed I^- ions from the surface of Pd nanowires, possibly due to a stronger binding of I^- ions, relative to Br^- ions, to the Pd(100) surface [24]. In this regard, a higher reaction temperature and longer time would be required for the removal of I^- ions from the surface. As shown in Figure 3.7b, the intensity of I 3d XPS peak was greatly reduced when the nanowires were subject to aging at 160 ℃ for 15 h, and eventually the chemisorbed I^- ions were mostly removed from the surface after 40 h.

Figure 3.6, c−f, shows TEM images of the nanocrystals obtained from different types of seeds. Because the {100} facets of the Br^--capped cuboctahedrons were passivated by Br^- ions, the newly formed Pd atoms could only be deposited on the Pd{111} facets . With the continuous deposition of Pd atoms, the eight {111}-enclosed corners of a cuboctahedral seed were gradually filled, giving a square projection with slight truncation at the corners (Figure 3.6c). In comparison, in the absence of Br^- ions on the {100} surfaces of a cuboctahedral seed, the Pd atoms were randomly deposited on the entire surface of seed (Figure 3.6e). The resultant nanocrystals retained the cuboctahedral shape of the seeds and only evolved into larger cuboctahedrons with multiple bumps on the surface.

Similar to the overgrowth of cubic seeds, the growth mode for a cuboctahedral seed was also found to be influenced by the surface condition. Owing to the larger proportion of {111} facets of a cuboctahedron relative to a cube, the difference in growth modes on the Pd(100) and Pd(111) surfaces can be conveniently resolved. Specifically, the surface of resultant nanocrystals is relatively smooth for the Br^--capped cuboctahedral seeds, suggesting a layered growth mode on the Pd(111) surface. In comparison, if the

chemisorbed Br^- ions have been removed from the cuboctahedral seeds, the morphology of the resultant nanocrystals showed a combination of layered and island growth. In particular, the growth took an island growth mode on the Pd(100) surface and a layered growth mode on the Pd(111) surface of a cuboctahedral seed due to their difference in the diffusion activation barrier.

The role of a surface capping agent in affecting the overgrowth pattern was also observed in the case of nanowire seeds. Because the side surface of a nanowire is enclosed by {100} facets and passivated by chemisorbed I^- ions, the newly formed Pd atoms could only be deposited onto the edges and the two ends (Figure 3.6d). In contrast, the Pd atoms were found to be deposited randomly on the entire surface of an I^--free nanowire, leading to the formation of a nanowire with multiple bumps on the side faces. The bumpy surface also suggests that an island growth mode was in dominance for the atom deposition, due to the presence of a larger bare area and a higher diffusion energy barrier for Pd(100) surface (Figure 3.6f).

3.3 Summary

In summary, I have systematically investigated the roles of a capping agent in determining the growth pattern of various types of Pd nanocrystals in a seed-mediated setting. Upon collision with the surface of a seed, the atom has three options: deposition, desorption, and migration. In the presence of a capping agent that selectively passivates certain regions of a seed and thus block the deposition of atoms, only desorption and migration are allowed. In this case, the newly formed Pd atoms are expected to only grow from the bare regions on the surface of a seed. To this end, the atom deposition would be exclusively confined to the corners and edges when the {100} side faces of a cubic seed were capped by Br^- ions. In comparison, the atoms were randomly deposited on the entire surface of a seed, including the side faces, edges, and corners if the chemisorbed Br^- ions had been removed from the surface of the seed. In addition, the growth mode

was found to be strongly correlated with the type and area of facets exposed on the surface of a seed. When the deposition occurred on the (100) surface with a higher activation energy barrier for diffusion relative to the (111) surface, the deposition on a Pd cubic seed would adopt an island growth mode because the nucleation sites were too far away from each other and the surface diffusion was inadequate to enable sufficient mass transport. In contrast, the growth of Br^--capped seeds took a layered mode because of a smaller proportion of the (111) surface and its lower diffusion activation energy barrier. The growth on Pd(100) surface could be switched to a layered mode by raising the reaction temperature to accelerate surface diffusion. The difference in growth mode for different types of seeds further allowed me to examine the correlation between the surface condition and the overall probability of atom deposition. Furthermore, the collision model was extended to explain the growth patterns of other types of seeds characterized by a mix of {111} and {110} facets in different proportions or different internal structures, including cuboctahedrons and penta-twinned nanowires. I believe that the mechanistic understanding achieved in this work is extendable to other systems involving combinations of different materials, types of seeds, and capping agents.

3.4 Experimental Methods

Synthesis of Pd Cubic Seeds. The Pd nanocubes to be used as seeds were prepared using a previously reported protocol [25]. In a typical synthesis, 8 mL of an aqueous solution containing 105 mg of PVP, 60 mg of AA, and 600 mg of KBr was added into a 20-mL glass vial and heated at 80 ℃ for 5 min. Then, 3 mL of an aqueous solution containing 57 mg of Na_2PdCl_4 was injected in one shot under magnetic stirring. The reaction was allowed to proceed at 80 ℃ for 3 h. The product was collected by centrifugation at 13,200 rpm, washed with water three times, and re-dispersed in 11 mL of deionized water.

Synthesis of Pd Cuboctahedral Seeds. The Pd cuboctahedral seeds were prepared using a seed-mediated approach according to a reported protocol [23]. Typically, 8 mL of an aqueous solution containing 105 mg of PVP, 100 μL of HCHO, and 0.3 mL of an aqueous suspension of the 18-nm Pd nanocubes (1.8 mg/mL in concentration) were added into a 20-mL glass vial and heated at 60℃ for 5 min under magnetic stirring. Subsequently, 3 mL of an aqueous solution containing 8.7 mg of Na_2PdCl_4 was introduced into the pre-heated mixture with a pipette in one shot. The reaction was allowed to proceed at 60 ℃ for 3 h before the product was collected by centrifugation at 13,200 rpm and washing with deionized water three times, and re-dispersed in 11 mL of deionized water.

Synthesis of Pd Nanowire Seeds. The Pd nanowires to be used as seeds were synthesized with the introduction of I^- ions as the capping agent to stabilize of the Pd{100} facets. In a typical synthesis, 105 mg of PVP, 100 mg of AA, 100 mg of NaI, and 5 μL of aqueous hydrochloric acid solution (HCl, 37 %) were dissolved in 8 mL of diethylene glycol (DEG) hosted in a 20-mL glass vial, and pre-heated in an oil bath (160 ℃) for 15 min under magnetic stirring. Subsequently, 3 mL of DEG containing 30 mg Na_2PdCl_4 was pipetted into the reaction mixture in one shot. The reaction was allowed to proceed at 160 ℃ for 1 h and quenched by immersing the vial in an ice-water bath. The product was collected by centrifugation at 13,200 rpm, washed once with acetone and then twice with DI water to remove DEG and excess PVP, and re-disperse in 11 mL of deionized water.

Removal of the Chemisorbed Br^- or I^- Ions from the Surface of Pd Seeds. The procedure used for the removal of the chemisorbed capping agent was adapted from the method described in Chapter 2 [17]. Specifically, 1 mL of an aqueous suspension of Pd seeds (1.8 mg/mL in concentration) and 5 mL EG containing 50 mg of PVP and 50 mg of CA were added into a 20-mL vial. The reaction mixture was then aged at 120 ℃ for 15 h and 160℃ for 40 h to remove the chemisorbed Br^- and I^- ions, respectively, from the

surface of the seeds. After centrifuging at 16,000 rpm and washing with ethanol once and water three times, the solid product was re-dispersed in 1 mL of deionized water.

Standard Procedure for the Seeded Growth. In a standard synthesis, 0.72 mL of aqueous Na_2PdCl_4 (0.5 mg/mL) was injected at a rate of 0.5 mL/h using a syringe pump into 4 mL of an aqueous suspension containing 100 μL of the Pd seeds (1.8 mg/mL), 30 mg of AA, and 50 mg of PVP at room temperature under magnetic stirring. After all the precursor solution had been introduced, the synthesis was allowed to proceed for another 5 min. The product was collected by centrifugation at 13,200 rpm and washed with water three times before characterization.

Characterization. The TEM images were taken using a Hitachi (HT7700) microscope operated at 120 kV. The sample for TEM analysis was prepared by drying a drop of the suspension of nanocrystals on a carbon-coated copper grid, followed by drying at room temperature under ambient conditions. The XPS data were collected using a Thermo K-Alpha spectrometer with an Al Kα source.

3.5 References

[1] Niu, W.; Zhang, L.; Xu, G. *Nanoscale* **2013**, *5*, 3172−3181.

[2] Chen, M.; Wu, B.; Yang, J.; Zheng, N. *Adv. Mater.* **2012**, *134*, 15822−15831.

[3] Chiu, C.-Y.; Ruan, L.; Huang, Y. *Chem. Soc. Rev.* **2013**, *42*, 2512−2527.

[4] Lohse, S. E.; Burrows, N. D.; Scarabelli, L.; Liz-Mazán, L. M.; Murphy, C. J. *Chem. Mater.* **2014**, *26*, 34−43.

[5] Niu, Z.; Li, Y. *Chem. Mater.* **2014**, *26*, 72−83.

[6] Ortiz, N.; Skrabalak, S. E. *Langmuir* **2014**, *30*, 6649−6659.

[7] Chen, Y.-H.; Hung, H.-H.; Huang, M. H. *J. Am. Chem. Soc.* **2009**, *131*, 9114-9121.

[8] Sun, Y.; Zhang, L.; Zhou, H.; Zhu, Y.; Sutter, E.; Ji, Y.; Rafailovich, M. H.; Sokolov,

J. C. *Chem. Mater.* **2007**, *19*, 2065−2070.

[9] Niu, W.; Zhang, L.; Xu, G. *ACS Nano* **2010**, *4*, 1987−1996.

[10] Xia, X.; Choi, S.-I.; Herron, J. A.; Lu, N.; Scaranto, J.; Peng, H.-C.; Wang, J.; Mavrikakis, M.; Kim, M. J.; Xia, Y. *J. Am. Chem. Soc.* **2013**, *135*, 15706−15709.

[11] Huang, X.; Tang, S.; Mu, X.; Dai, Y.; Chen, G.; Zhou, Z.; Ruan, F.; Yang, Z.; Zheng, N. *Nat. Nanotechnol.* **2011**, *6*, 28−32.

[12] Gugliotti, L. A.; Feldheim, D. L.; Eaton, B. E. *Science* **2004**, *304*, 850−852.

[13] Heinz, H.; Farmer, B. L.; Pandey, R. B.; Slocik, J. M.; Patnaik, S. S.; Pachter, R.; R. R. Naik *J. Am. Chem. Soc.* **2009**, *131*, 9704−9714.

[14] Chiu, C.-Y.; Li, Y.; Huang, Y. *Nanoscale* **2010**, *2*, 927−930.

[15] Fan, F.-R.; Liu, D.-Y.; Wu, Y.-F.; Duan, S.; Xie, Z.-X.; Jiang, Z.-Y.; Tian, Z.-Q. *J. Am. Chem. Soc.* **2008**, *130*, 6949−6951.

[16] Xie, S.; Peng, H.-C.; Lu, N.; Wang, J.; Kim, M. J.; Xie, Z.; Xia, Y. *J. Am. Chem. Soc.* **2013**, *135*, 16658−16667.Doyle, A. M.; Shaikhutdinov, S. K.; Jackson, S. D.; Freund, H.-J. *Angew. Chem., Int. Ed.* **2003**, *42*, 5240−5243.

[17] Peng, H.-C.; Xie, S.; Park, J.; Xia, X.; Xia, Y. *J. Am. Chem. Soc.* **2013**, *135*, 3780−3783.

[18] Kolasinki, K. W. *Surface Science, 2nd ed.*; Wiley: New York, 2008.

[19] Xia, Y.; Xiong, Y.; Lim, B.; Skrabalak, S. E. *Angew. Chem., Int. Ed.* **2009**, *48*, 60−103.

[20] Antczak, G.; Ehrlich, G. *Surface Diffusion: Metals, Metal atoms, and Clusters*; Cambridge University Press: Cambridge, 2006.

[21] Nilekar, A. U.; Greeley, J.; Mavrikakis, M. *Angew. Chem., Int. Ed.* **2006**, *45*, 7046−7049.

[22] Xia, X.; Xie, S.; Liu, M.; Peng, H.-C.; Lu, N.; Wang, J.; Kim, M. J.; Xia, Y. *Proc. Natl. Acad. Sci. U.S.A.* **2013**, *110*, 6669−6673.

[23] Jin, M.; Zhang, H.; Xie, Z.; Xia, Y. *Energy Environ. Sci.* **2012**, *5*, 6352−6357.

[24] Elding, L. I.; Olsson, L.-F. *Inorg. Chim. Acta* **1986**, *117*, 9−16.

[25] Jin, M.; Liu, H.; Zhang, H.; Xie, Z.; Xia, Y. *Nano Res.* **2011**, *4*, 83−91.

CHAPTER 4

USE OF REDUCTION RATE AS A QUANTITATIVE KNOB FOR CONTROLLING THE INTERNAL STRUCTURE AND SHAPE OF PALLADIUM NANOCRYSTALS

4.1 Introduction

Significant progress has been made in understanding the formation of nanocrystals with a specific shape by identifying the nucleation and growth pathway. In general, nuclei with fluctuating structures will be formed *via* homogeneous nucleation when metal atoms are generated in a solution through the reduction or decomposition of a precursor. Once the nuclei have grown past a critical size, they evolve into seeds with different internal structures, including those with a single-crystal, singly-twinned, multiply twinned, or stacking fault-lined structure [1]. Unlike the ideal ABCABC sequence of stacking along the <111> direction in a cubic close packing, single-crystal seed, planar defects occurs whenever the ideal ABCABC sequence of stacking along the <111> direction is disrupted. The presence of planar defects in a crystal lattice will therefore lead to the formation of seeds with diversified internal structures. For example, in a singly-twinned crystal with a local stacking sequence of ABCAB|C|BACBA, either side of the marked C plane (*i.e.*, the twin boundary) has a perfect cubic close packing (*ccp*) structure, with the two lattices being mirror images to each other across the twin boundary (Figure 4.1a). When more than one twin defects are introduced into the lattice of an *fcc* metal, multiply twinned seeds, including decahedrons and icosahedrons, will be obtained. As shown in Figure 4.1b, a decahedral seed can be viewed as an assembly of five tetrahedral units by sharing one common edge. For an icosahedral seed, it consists of twenty tetrahedral units, with its surface enclosed exclusively by {111} facets (Figure

4.1c).

In addition to the twin boundary, another type of planar defect occurs when inserting or extracting an A, B, or C layer into a *ccp* structure, corresponding to an extrinsic or intrinsic stacking fault, respectively. When a layer of C is inserted or extracted, respectively, the stacking sequence will be changed to ABCACBCABC or ABCABABC. In either case, there is a thin layer of hexagonal close packing (*hcp*) structure, in the sequence of CBC or ABA, at the site of the stacking fault. The presence of a periodically alternating *ccp*/*hcp* structure is commonly observed in noble-metal nanocrystals owing to a relatively low energy barrier involved in the formation of stacking faults under very

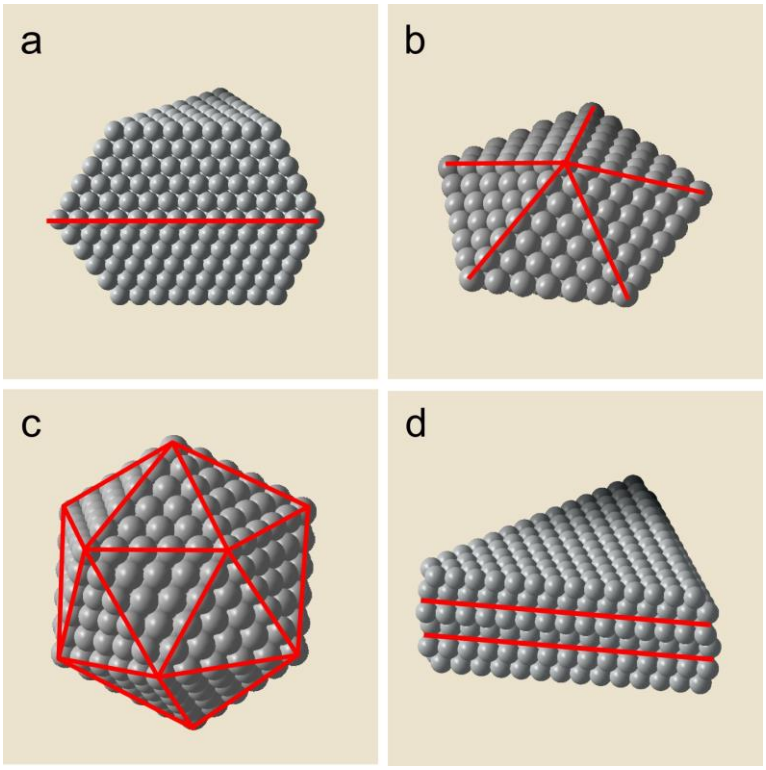

Figure 4.1. Atomic models of four different types of seeds lined with twin defects or stacking faults. The seeds in (a−c) contain one, five, and thirty twin defects while the seed in (d) contains two stacking faults. The twin planes or stacking faults are delineated in red.

slow reaction kinetics. Geometrically, the inclusion of stacking faults along the <111> direction of a crystal leads to the formation of seeds lined with stacking faults, together with a triangular or hexagonal, plate-like appearance whose two large, flat surfaces are presented by {111} facets (Figure 4.1d).

Once the seeds with fixed internal structures have formed, they will then grow in size into nanocrystals with distinctive shapes or facets as dictated by interplay of surface capping and reaction kinetics [1]. For example, the single-crystal seed can evolve into a cube, truncated cube, cuboctahedron, truncated octahedron, octahedron, or rhombic dodecahedron depending on the relative growth rates of {100}, {111}, and {110} facets, which can be maneuvered *via* the use of a facet-selective capping agent [2, 3]. For the seeds with multiple twin defects and stacking faults, the final products will be decahedrons (or icosahedrons) and thin plates, respectively. This correlation between the shape of a nanocrystal and the internal structure of its seed was initially formulated for Ag nanocrystals prepared using the polyol method, with ethylene glycol serving as a solvent and a precursor to the reductant for $AgNO_3$ at an elevated temperature [4]. Later, it was also observed in other metals including Au, Cu, Pd, Pt, and Rh, as well as their bimetallic combinations [1, 5−7].

From a thermodynamic perspective, the inclusion of defects into a crystal lattice will significantly increase the total free energy of a system, making such seeds less favorable. In particular, the strain energy associated with the defect zone increases rapidly as a defect-lined seed is enlarged in size [8, 9]. As a result, the stability of a twinned or stacking fault-lined seed is negatively correlated with its size. The energetic penalty caused by the formation of a twin defect or stacking fault can, however, be compensated by reducing the total surface area and thus the total surface free energy relative to its single-crystal counterpart. In particular, the inclusion of twin defects can continue up to a critical size, above which the energetic cost of retaining the defects will become prohibitive, forcing the seed to transform into the single-crystal form [10]. Computational

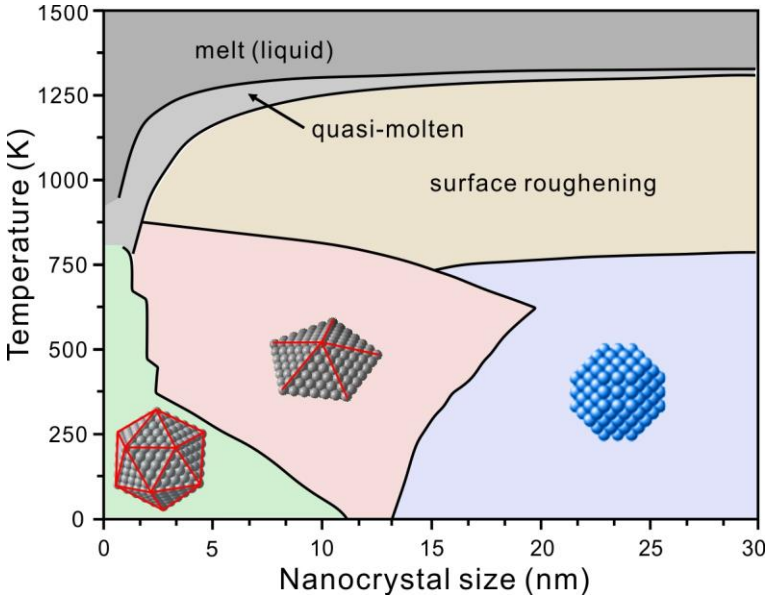

Figure 4.2. Populations of seeds with different internal structures as determined by thermodynamic factors. A phase diagram of Au nanocrystals derived from calculations, indicating the transition from icosahedrons to decahedrons and then single-crystal seeds as their sizes increase. (Adapted with permission from [11]. Copyright 2009 American Chemical Society.)

simulation is an invaluable tool that allows for the calculation of the free energy of formation for a seed at given temperature and size by taking into account of all the relevant factors, including the interaction between atoms, the surface energy, and the strain energy. By applying the calculation to all possible structures at different temperatures and then comparing their free energies, one can construct a quantitative phase diagram that can be used to identify the thermodynamically most stable structure under the specific set of experimental conditions [11]. Most significantly, the phase diagram provides an additional dimension with regard to the critical diameters that separate the adjacent groups of seeds with different internal structures. With Au as an example, Au nanocrystal seeds with different internal structures are expected to emerge as both the size and temperature are changed, as shown in Figure 4.2. More specifically,

the icosahedral, decahedral, and single-crystal species are thermodynamically favored at relatively small, intermediate, and large sizes [11]. For seeds with small sizes, the most stable structure changes from icosahedral to decahedral as temperature is increased. The possible transition between seeds with different internal structures has been validated by high-resolution TEM (HRTEM) studies, in which various types of thermodynamic equilibria can be achieved by heating the sample *in situ* [11]. Heating also increases the mobility of constituent atoms as well, helping reshape the seeds into their most stable structure at the given temperature [12].

Although computational simulation can predict the stability of seeds under a specific set of thermodynamic conditions, the results often offset from experimental observations. For example, multiply twinned nanoparticles of Au, including decahedrons and icosahedrons, have been prepared with sizes larger than 100 nm, far beyond the limits derived from computational studies, despite thermodynamic arguments to the contrary [13, 14]. The discrepancy between experimental and computational results can be attributed to reaction kinetics, involving a set of experimental parameters that can be manipulated independent of thermodynamics [15, 16]. Since the energy barrier for the transition from one type of seed to another is relatively low, seeds with more than one type of internal structures can co-exist in a synthesis. Under certain conditions, instead of reaching the state of global minimum free energy, some seeds are trapped in a local minimum in terms of energy, leading to the presence of a thermodynamically less stable but kinetically favored state. In this case, seeds that are not favored in terms of thermodynamics can still appear in the final product once they are generated in the nucleation stage.

Despite the incredible progress that has been made over the past few decades, it remains a grand challenge to rationally and reproducibly manipulate the shape of noble-metal nanocrystals and thus control their properties. The challenge can be largely attributed to the lack of a quantitative knob that can be employed to precisely control the

nucleation and growth of nanocrystals. For example, there is still no quantitative knowledge about the experimental conditions or parameters that control the internal structure taken by a seed during the nucleation process. In many cases, one has to rely on the introduction of an oxidative etchant to selectively etch away seeds with twin defects and thus obtain single-crystal seeds only [17]. While this strategy works effectively for the syntheses of nanocrystals with a single-crystal structure, it cannot be applied to those with twin defects or stacking faults. Ideally, one needs a quantitative knob that can be tuned to precisely manipulate the nucleation and growth pathways in a predictable way by controlling a small set of experimental parameters.

4.2 Results and Discussion

With Pd as a typical example, here I and my collaborator demonstrate that there exists a quantitative correlation between the internal structure of nanocrystals and the initial reduction rate of a synthesis. This study was inspired by the variable outcomes of a polyol synthesis that typically involves the reduction of Na_2PdCl_4(II) by EG or DEG glycol in the presence of PVP [18, 19]. The internal structure undertaken by the nanocrystals was found to be sensitive to the type of polyol used and the reaction temperature. Figure 4.3a shows TEM image of the Pd nanocrystals obtained using EG-based reduction at 140 °C. The particles took a truncated octahedral shape, with the surface covered by a mix of {111} and {100} facets (see the inset for an atomic model). The high-angle annular dark-field scanning-TEM image in Figure 4.3b clearly shows a single-crystal structure with a well-resolved, periodic arrangement of atoms. In contrast, when the synthesis was conducted in DEG and at 140 °C, multiply twinned icosahedrons with an average edge length of 5.8 nm were obtained in 100% purity (Figure 4.3c). As illustrated in the inset, each icosahedron is enclosed by 20 {111} facets. The twin defects revealed by the corresponding HAADF-STEM image (Figure 4.3d) confirm the

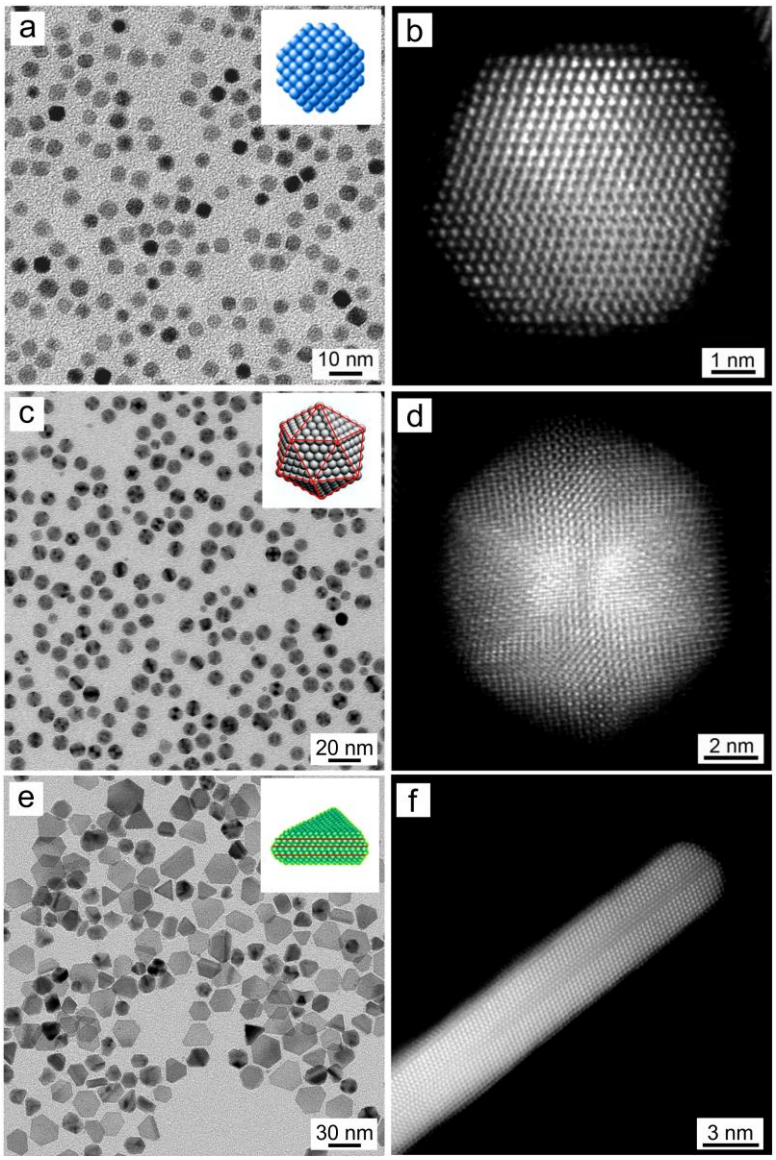

Figure 4.3. Palladium nanocrystals with three distinctive internal structures obtained under different reaction conditions. The Pd nanocrystals were prepared using the standard procedure except for the variation in the type of polyol and reaction temperature: (a, b) truncated octahedrons in EG at 140 °C; (c, d) icosahedrons in DEG at 140 °C; (e, f) nanoplates in DEG at 75 °C. (a, c, e) TEM images of the Pd nanocrystals produced at each condition. The insets show the corresponding atomic models of the nanocrystals, with the twin planes or stacking faults being delineated in red. (b, d, f) High-resolution HAADF-STEM images of individual nanocrystals, revealing the different internal structures: (b) single-crystal, (d) multiply twinned, and (f) stacking fault-lined. Note that (f) was taken from the side face of a nanoplate. (Reprinted with permission from [25]. Copyright 2015 American Chemical Society.)

involvement of a multiply twinned structure. When the reaction temperature of the DEG-based synthesis was decreased to 75 °C, the final products contained 85% of nanoplates with an average edge length of 25 nm, together with 15% of multiply twinned decahedrons (Figure 4.3e). The HAADF-STEM image (Figure 4.3f) taken from the side face of a nanoplate indicates the existence of stacking faults along a direction normal to the large, flat surfaces of a plate. Collectively, these results suggest that Pd nanocrystals with distinctive internal structures, including single-crystal, multiply twinned, and stacking fault-lined, could all be obtained in high purity by simply varying the type of polyol and/or the reaction temperature while keeping all other parameters unchanged. Since both the type of polyol and temperature will affect the reduction kinetics, we hypothesize that the initial reduction rate of a synthesis could serve as a quantitative knob for controlling the formation of seeds with different internal structures during the nucleation. By controlling this single parameter, one would be able to deterministically obtain Pd nanocrystals with different types of internal structures and thus distinctive shapes.

One has to know the rate law of a reaction in order to quantitatively analyze and compare the effects of reduction kinetics under different conditions. To this end, the concentrations of $PdCl_4^{2-}$ remaining in the reaction solution at different time points after it had been introduced into a polyol were derived by recording the UV-vis spectra of $PdCl_4^{2-}$, the precursor to Pd atom. At each time point, 0.3 mL aliquot was sampled from the reaction solution using a glass pipette and immediately injected into 2.7 mL of 0.1 M aqueous HCl solution held at 0 °C. The quick drop in temperature could immediately quench the reduction reaction and thus preserve the concentration of $PdCl_4^{2-}$. The sample was then centrifuged to remove the Pd nanoparticles, followed by dilution of the supernatant with the same aqueous HCl solution to a level suitable for UV-vis measurement. The HCl played a critical role in preventing the precursor from hydrolysis when it was diluted with water to lower concentrations [20].

In order to determine the concentration of $PdCl_4^{2-}$ in the reaction solution, a calibration curve was prepared by plotting absorbance versus concentration for a set of UV-vis spectra taken from Na_2PdCl_4 solutions with known concentrations. As shown in Figure 4.4a, two absorption peaks appeared at 222 and 279 nm, similar to what was reported for $PdCl_4^{2-}$ in the literature [21]. The positions of these two peaks did not show any shift even after the solution had been diluted with the aqueous HCl solution to a concentration as low as 1 μM, confirming the effectiveness of HCl in preventing the precursor from hydrolysis. In the case of EG at 140 °C, the absorbance of the precursor at 279 nm drastically decreased from 1.00 to 0.04 within just 5 min after the precursor had been introduced into the reaction solution (Figure 4.5a). In comparison, the absorbance of the precursor at 279 nm only dropped from 1.00 to 0.68 within 10 min when the reaction was conducted in DEG (Figure 4.5b). Based on the calibration curve in Figure 4.4b, I readily obtained the concentrations of $PdCl_4^{2-}$ remaining in the reaction solution and the percentages of conversion from $PdCl_4^{2-}$ to Pd(0) at different time points. As shown in Figure 4.5c, 96.5% of the $PdCl_4^{2-}$ was reduced to Pd atoms within 5 min in the EG-based synthesis and this value increased to 98.3% at t=10 min. In comparison, the conversion of the $PdCl_4^{2-}$ to Pd atoms in DEG was only 29.9% within the first 10 min, suggesting a much weaker reducing power for DEG relative to EG.

As discussed in Chapter 1, the reaction rate of an elementary reaction (mA + nB → *product*) is a function of the rate constant, the concentrations of reactants, and the reaction orders (See Eq. 1.5). Specifically, the rate constant is determined by a combination of multiple experimental parameters, including the type of precursor, the type of reductant, solvent, and reaction temperature. In the synthesis of noble-metal nanocrystals, the reduction of a salt precursor is expected to follow a second-order rate law due to the involvement of collision and electron transfer between the precursor and reductant [22]. In the present study, since the reductant (polyol, the reactant B) is in great excess relative to the precursor ($PdCl_4^{2-}$, the reactant A), the concentration of B should

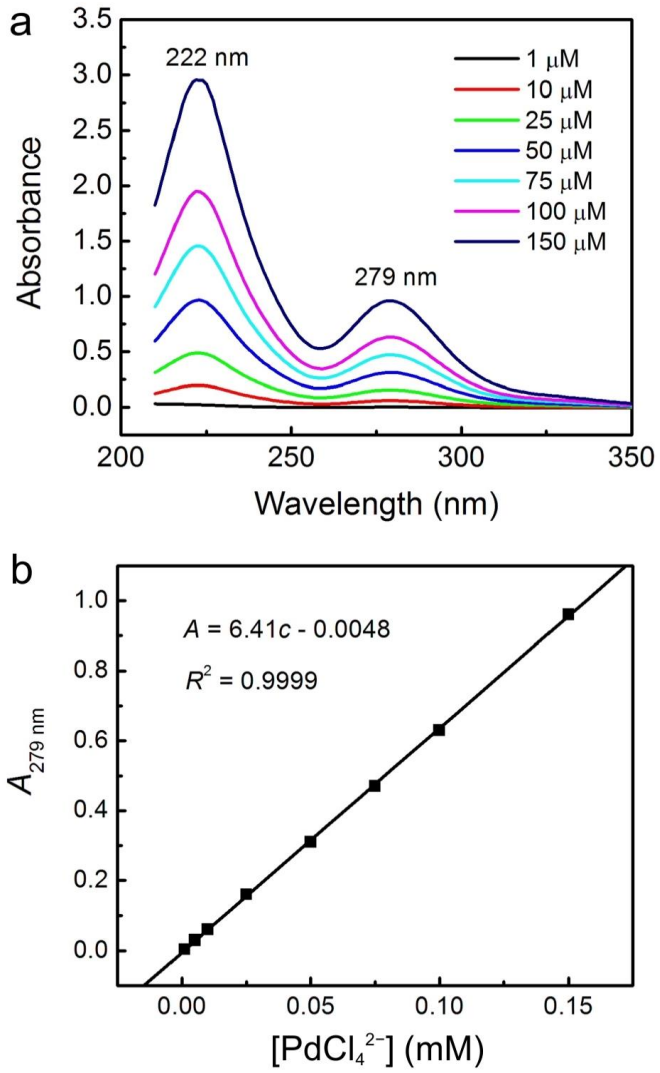

Figure 4.4. (a) UV-vis spectra taken from standard Na_2PdCl_4 solutions with different concentrations. (b) A plot showing the absorbance at 279 nm as a function of the concentration of $PdCl_4^{2-}$. This calibration curve can be used to calculate the concentration of $PdCl_4^{2-}$ remaining in the reaction solution from the UV-vis spectrum of the sample. (Reprinted with permission from [25]. Copyright 2015 American Chemical Society.)

remain at a constant level during the entire synthesis. As such, the kinetics involved could be approximated as a pseudo-first-order reaction, with the rate law being simplified as:

$$r = k\,[\mathrm{A}] = -\,d[\mathrm{A}] / dt \tag{4.1}$$

This equation can be easily integrated to obtain:

$$\ln[\mathrm{A}]_t = -\,kt + \ln[\mathrm{A}]_0 \tag{4.2}$$

where $[A]_0$ and $[A]_t$ represent the concentrations of the precursor at the beginning of a synthesis and at a specific time point, respectively. In this case, a straight line will be obtained with a slope of $-k$ when $\ln[A]_t$ is plotted as a function of reaction time (t).

Figure 4.5d shows plots of $\ln[PdCl_4^{2-}]_t$ as a function of reaction time for EG- and DEG-based syntheses, respectively, conducted at 140 °C. It can be seen that the values of $\ln[PdCl_4^{2-}]_t$ indeed decrease linearly with reaction time, confirming that the reduction was first-order with respect to the precursor concentration. In addition, since the values of $\ln[PdCl_4^{2-}]_t$ did not show any abrupt changes deviated from the linear plot, it is reasonable to assume that no autocatalytic reaction was involved in the polyol synthesis described here [23]. From the slopes of the linear regression lines, the rate constants were determined to be 1.12×10^{-2} s^{-1} and 5.57×10^{-4} s^{-1} for the reduction of $PdCl_4^{2-}$ by EG and DEG, respectively, at 140 °C. Combined with the initial concentration of $PdCl_4^{2-}$ (1.76×10^{-2} M), the corresponding initial rates were 1.97×10^{-4} $M\cdot s^{-1}$ for EG and 9.80×10^{-6} $M\cdot s^{-1}$ for DEG.

I further extended the kinetic measurements to other combinations of polyol and reaction temperature. As shown in Figure 4.6 and Table 4.1, the use of a polyol with a longer hydrocarbon chain or a lower reaction temperature would decrease the rate constant. In addition, from the rate constants at different temperatures, the activation

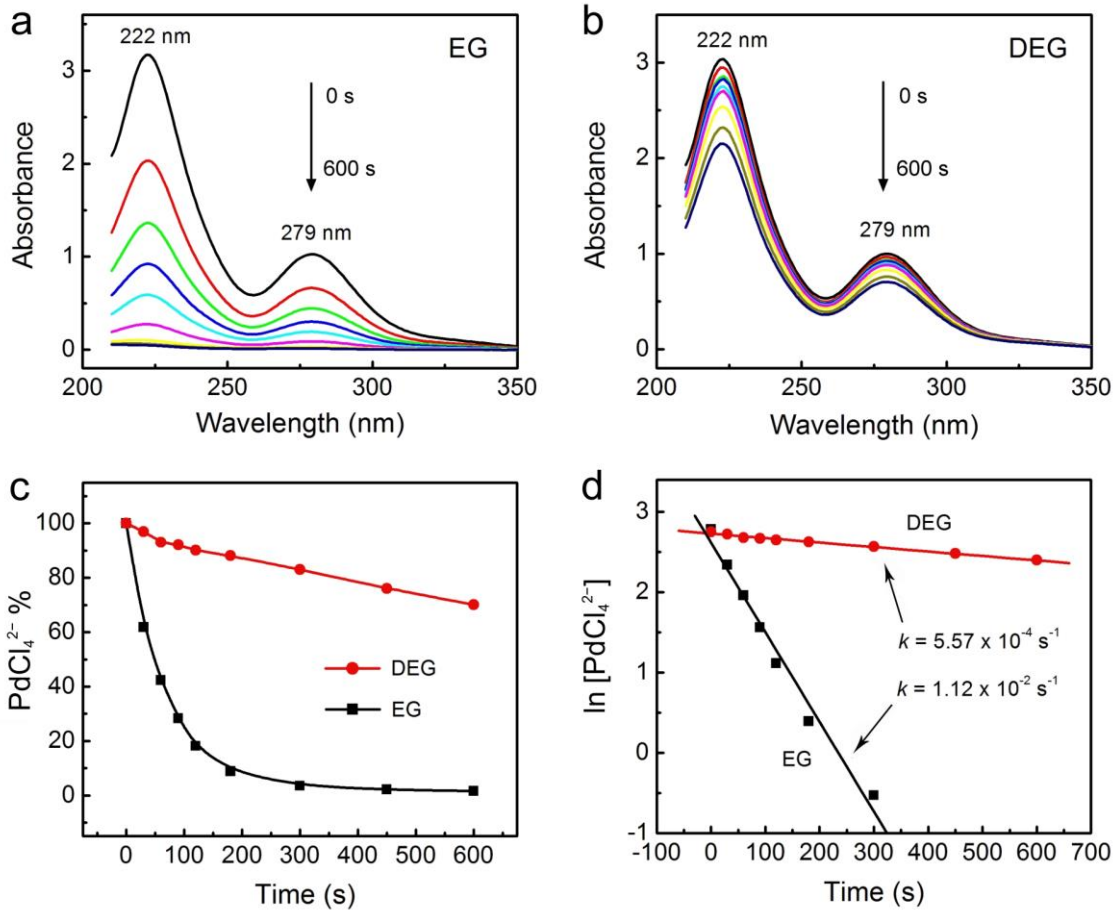

Figure 4.5. Quantitative analysis of the reduction kinetics involved in the polyol synthesis of Pd nanocrystals. (a, b) UV-vis spectra of $PdCl_4^{2-}$ remaining in the EG and DEG solutions after the reaction had proceeded for 0 to 30, 60, 90, 120, 180, 300, 450, and 600 s. (c) A plot showing the percentages of $PdCl_4^{2-}$ remaining in the reaction solutions (calculated using the absorbance at 279 nm) as a function of reaction time. (d) A plot showing the pseudo-first-order reaction kinetics involved in the syntheses of single-crystal and multiply twinned Pd nanocrystals in EG and DEG, respectively, at 140 °C. The rate constants (k) were 1.12×10^{-2} and 5.57×10^{-4} s^{-1}, respectively, for the EG- and DEG-based systems. (Reprinted with permission from [25]. Copyright 2015 American Chemical Society.)

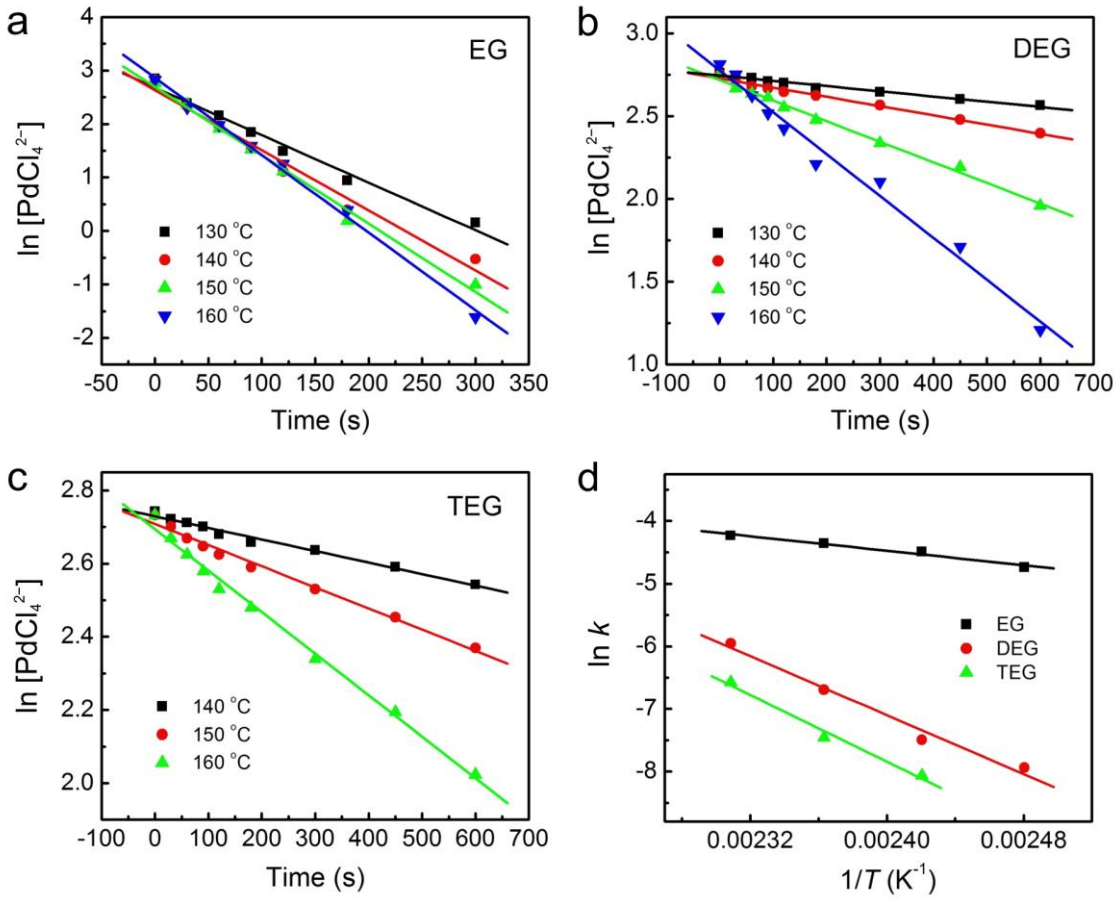

Figure 4.6. Determination of the rate constants under different reaction conditions and the activation energies. (a–c) Plots showing the concentrations of remaining $PdCl_4^{2-}$ as a function of reaction time for different combinations of polyol and temperature. (d) A plot showing ln*k* as a function of 1/T for three different reaction systems, where the slope of linear regression line can be used to calculate the corresponding activation energy of the reaction using the Arrhenius equation. (Reprinted with permission from [25]. Copyright 2015 American Chemical Society.)

Table 4.1. Kinetic parameters for the reduction of $PdCl_4^{2-}$ by various polyols at different reaction temperatures.

Polyol	Temperature (°C)	Rate constant k (s^{-1})	Activation energy E_a ($kJ \cdot mol^{-1}$)
EG	160	1.45×10^{-2}	24.0
	150	1.28×10^{-2}	
	140	1.12×10^{-2}	
	130	8.75×10^{-3}	
DEG	160	2.60×10^{-3}	103.2
	150	1.24×10^{-3}	
	140	5.57×10^{-4}	
	130	3.16×10^{-4}	
TEG	160	1.40×10^{-3}	110.7
	150	5.78×10^{-4}	
	140	3.15×10^{-4}	

energy (E_a) of a reduction reaction involving $PdCl_4^{2-}$ and a specific polyol can be derived from the Arrhenius equation:

$$k = Ae^{-Ea/RT} \tag{4.3}$$

where k is the rate constant of a reaction; A is the frequency factor; T is the reaction temperature (in Kelvin); and R is the universal gas constant (8.314 $J \cdot mol^{-1} \cdot K^{-1}$). Figure 4.6d shows a plot of ln$k$ as a function of $1/T$ for the reactions involving $PdCl_4^{2-}$ and different polyols. For the reduction of $PdCl_4^{2-}$ by EG, DEG, and triethylene glycol (TEG), their E_a values were found to be 24.0, 103.2, and 110.7 $kJ \cdot mol^{-1}$, respectively (Table 4.1). It is worth emphasizing the importance of knowing the activation energy of a reaction. Using the reduction of $PdCl_4^{2-}$ by DEG at 75 °C as an example, a significant drop in reducing power and thus a much slower reduction rate is expected at such a low temperature. As a result, it would be both challenging and time-consuming to experimentally determine the kinetic parameters with high accuracy by using the UV-vis method. It would be very straightforward to obtain the rate constant at this and other temperatures through the Arrhenius equation once the activation energy of this reaction is known. To this end, the rate constant for the reduction of $PdCl_4^{2-}$ by DEG at 75 °C was found to be 2.26×10^{-6} s^{-1}. Combined with the initial concentration of $PdCl_4^{2-}$ (1.76×10^{-2} M), an initial reduction rate of 3.98×10^{-8} $M \cdot s^{-1}$ was found to be responsible for the formation of nanoplates with stacking faults (Figure 4.3e).

As expected, the internal structure of the Pd nanocrystals would change significantly when the reduction kinetics was adjusted by varying the reaction temperature. Using the synthesis of single-crystal, truncated octahedrons of Pd in EG and at 140 °C as an example, when the reaction temperature was raised to 160 °C while keeping all other parameters the same, the particles in the product still had a single-crystal structure albeit they showed a cuboctahedral shape (Figure 4.7a). The change from truncated octahedron

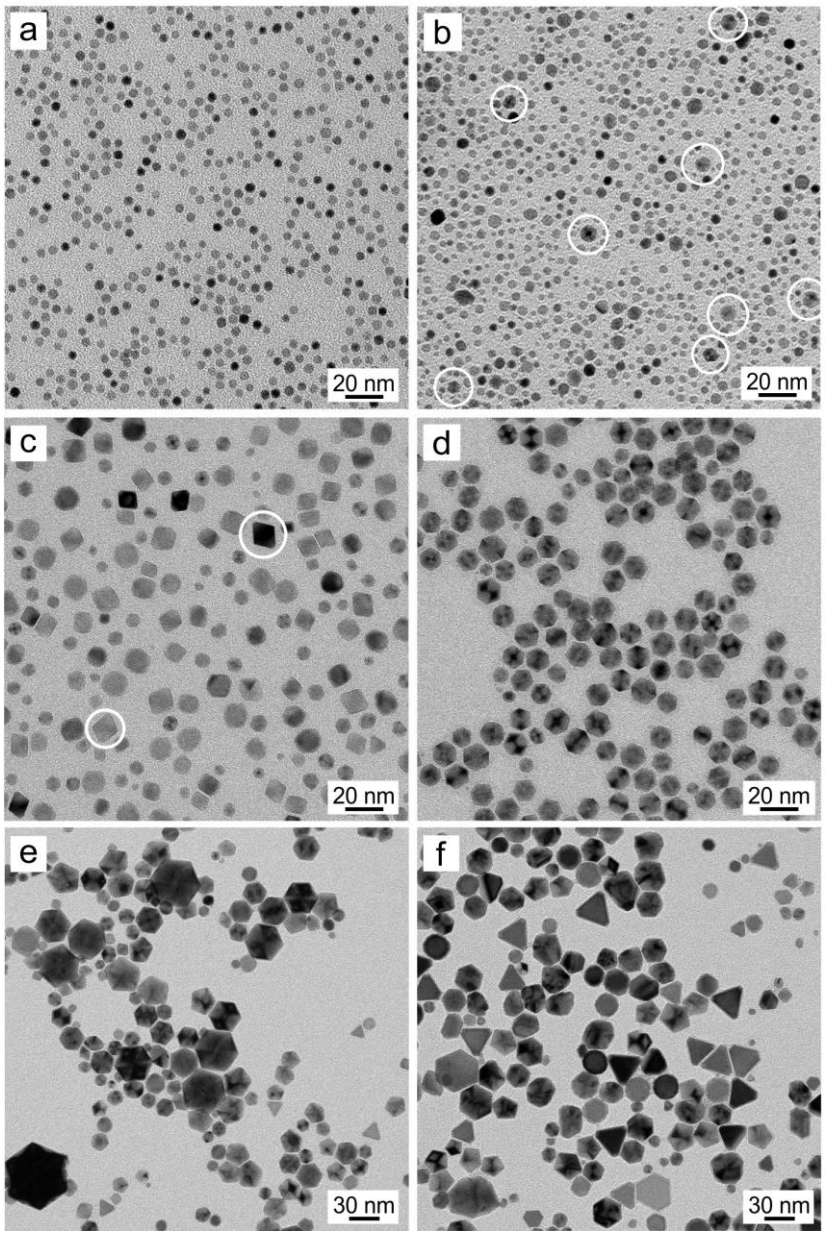

Figure 4.7. TEM images of Pd nanocrystals prepared using the standard procedure except for the variation in the type of polyol and reaction temperature at different initial reduction rates (r_0): (a) r_0=2.55×10^{-4} M·s^{-1} (in EG, at 160 °C, and k=1.45×10^{-2} s^{-1}); (b) r_0=1.54×10^{-4} M·s^{-1} (in EG, at 130 °C, and k=8.75×10^{-3} s^{-1}); (c) r_0=4.58×10^{-5} M·s^{-1} (in DEG, at 160 °C, and k=2.60×10^{-3} s^{-1}); (d) r_0=5.56×10^{-6} M·s^{-1} (in DEG, at 130 °C, and k=3.16×10^{-4} s^{-1}); (e) r_0=2.76×10^{-7} M·s^{-1} (in DEG, at 95 °C, and k=1.57×10^{-5} s^{-1}); and (f) r_0=1.08×10^{-7} M·s^{-1} (in DEG, at 85 °C, and k=6.11×10^{-6} s^{-1}). The white circles marked in (b) and (c) indicate multiply twinned and single-crystal Pd nanocrystals, respectively. (Reprinted with permission from [25]. Copyright 2015 American Chemical Society.)

to cuboctahedron can be attributed to the enhancement in atom migration on the surface as the temperature is increased [24]. In contrast, multiply twinned icosahedrons started to appear when the synthesis was conducted at 130 °C (Figure 4.7b), implying that the reduction rate associated with EG at 140 °C was very close to the minimum value required for the generation of single-crystal seeds in 100% purity. I also observed a similar transition in internal structure for the seeds when the synthesis was conducted in DEG at different temperatures. Multiply twinned icosahedrons were obtained in 100% purity when the reaction temperature was kept lower than or equal to 140 °C (Figure 4.3c and Figure 4.7d). However, the products became a mix of both single-crystal and multiple-twinned structures if the reaction temperature was raised above 140 °C (Figure 4.7c). When the reaction temperature was reduced below 95 °C, the proportion of icosahedrons in the product was found to gradually decrease, together with an increase in population for nanoplates with stacking faults (Figure 4.7, e and f). Combined together, these results qualitatively indicate that the internal structure developed in the seeds was highly dependent on the reduction kinetics, which can be conveniently manipulated by varying a set of experimental parameters, including the types of precursor and reductant and their initial concentrations, as well as reaction temperature.

To quantitatively understand the effect of reduction kinetics in determining the internal structure of Pd nanocrystals, the proportions of different types of seeds were plotted as a function of the initial reduction rates. The initial reduction rates were, in turn, calculated using the kinetic parameters acquired experimentally along with the initial precursor concentration (see Table 4.2 for details). As shown in Figure 4.8, there is clearly a correlation between the internal structure of seeds and the initial reduction rate. The nanocrystals gradually changed from stacking fault-lined to multiply twinned and then single-crystal as the initial reduction rate was increased from a level of 10^{-8} to 10^{-6} and then 10^{-4} $M \cdot s^{-1}$. The rate that separates the adjacent groups of seeds with different internal structures can be readily determined from this plot. Specifically, single-crystal

Table 4.2. Summary of the experimental parameters for the reactions between $PdCl_4^{2-}$ and various polyols at different conditions, and the corresponding rate constants (k) and initial rates (r_0)

Polyol	Temperature (°C)	Rate constant k (s^{-1})	Initial conc. of $PdCl_4^{2-}$ (M)	Initial rate r_0 ($M \cdot s^{-1}$)	Results (Figure)
EG	160	1.45×10^{-2}	1.76×10^{-2}	2.55×10^{-4}	4.7a
	150	1.28×10^{-2}	1.76×10^{-2}	2.25×10^{-4}	
	140	1.12×10^{-2}	1.76×10^{-2}	1.97×10^{-4}	4.3a
	140	1.12×10^{-2}	1.76×10^{-3}	1.97×10^{-5}	4.10a
	140	1.12×10^{-2}	7.04×10^{-4}	7.89×10^{-6}	4.10b
	130	8.75×10^{-3}	1.76×10^{-2}	1.54×10^{-4}	4.7b
DEG	160	2.60×10^{-3}	1.76×10^{-2}	4.58×10^{-5}	4.7c
	150	1.24×10^{-3}	1.76×10^{-2}	2.18×10^{-5}	
	140	5.57×10^{-4}	1.76×10^{-2}	9.80×10^{-6}	4.3c
	130	3.16×10^{-4}	1.76×10^{-2}	5.56×10^{-6}	4.7d
	130	3.16×10^{-4}	3.52×10^{-4}	1.11×10^{-7}	4.10c
	130	3.16×10^{-4}	1.76×10^{-4}	5.56×10^{-8}	4.10d
	95	1.57×10^{-5}*	1.76×10^{-2}	2.76×10^{-7}	4.7e
	85	6.11×10^{-6}*	1.76×10^{-2}	1.08×10^{-7}	4.7f
	75	2.26×10^{-6}*	1.76×10^{-2}	3.98×10^{-8}	4.3e
TEG	160	1.40×10^{-3}	1.76×10^{-2}	2.46×10^{-5}	4.9a
	150	5.78×10^{-4}	1.76×10^{-2}	1.02×10^{-5}	4.9b
	140	3.15×10^{-4}	1.76×10^{-2}	5.54×10^{-6}	4.9c
	85	2.11×10^{-6}*	1.76×10^{-2}	3.71×10^{-8}	4.9d

*These rate constants were derived from the Arrhenius equation.

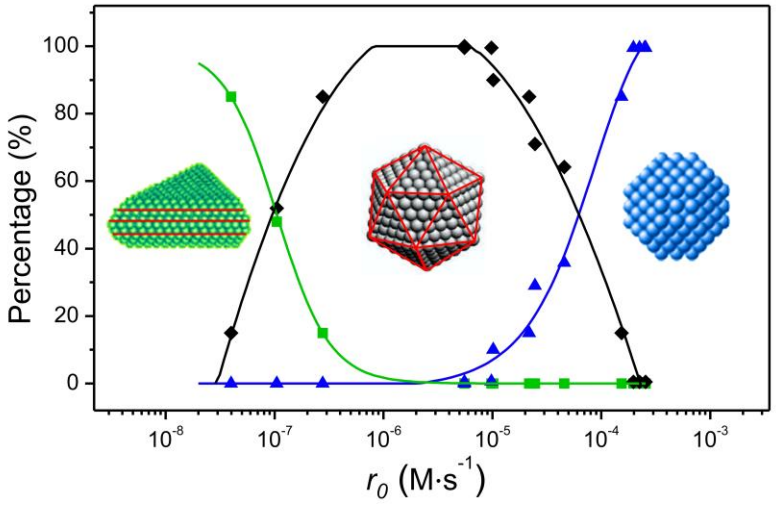

Figure 4.8. A plot showing the relative distribution of Pd nanocrystals with different internal structures as a function of the initial reaction rate (r_0) of a synthesis. The percentages of single-crystal, multiply twinned, and staking fault-lined structures were acquired using TEM imaging and are denoted in blue, black, and green colors, respectively. The twin planes or stacking faults are delineated in red. (Reprinted with permission from [25]. Copyright 2015 American Chemical Society.)

seeds were always obtained in 100% purity when the initial rate was faster than or equal to 1.97×10^{-4} M·s^{-1} whereas the initial rate had to be controlled in the range of 8.70×10^{-6} M·s^{-1} to 4.0×10^{-7} M·s^{-1} in order to generate multiply twinned icosahedrons in 100% purity. When the initial rate was between the thresholds for single-crystal and multiply twinned seeds (8.70×10^{-6} to 1.97×10^{-4} M·s^{-1}), both single-crystal and multiply twinned nanocrystals would appear in the final products. In the same way, the product contained both multiply twinned and stacking fault-lined nanocrystals when the initial rate was further decreased below the lower threshold (4.0×10^{-7} M·s^{-1}) for generating multiply twinned seeds. The correlation between the internal structure of Pd nanocrystals and the reduction kinetics was further validated by extending to polyol syntheses based on triethylene glycol, as documented in Figure 4.9.

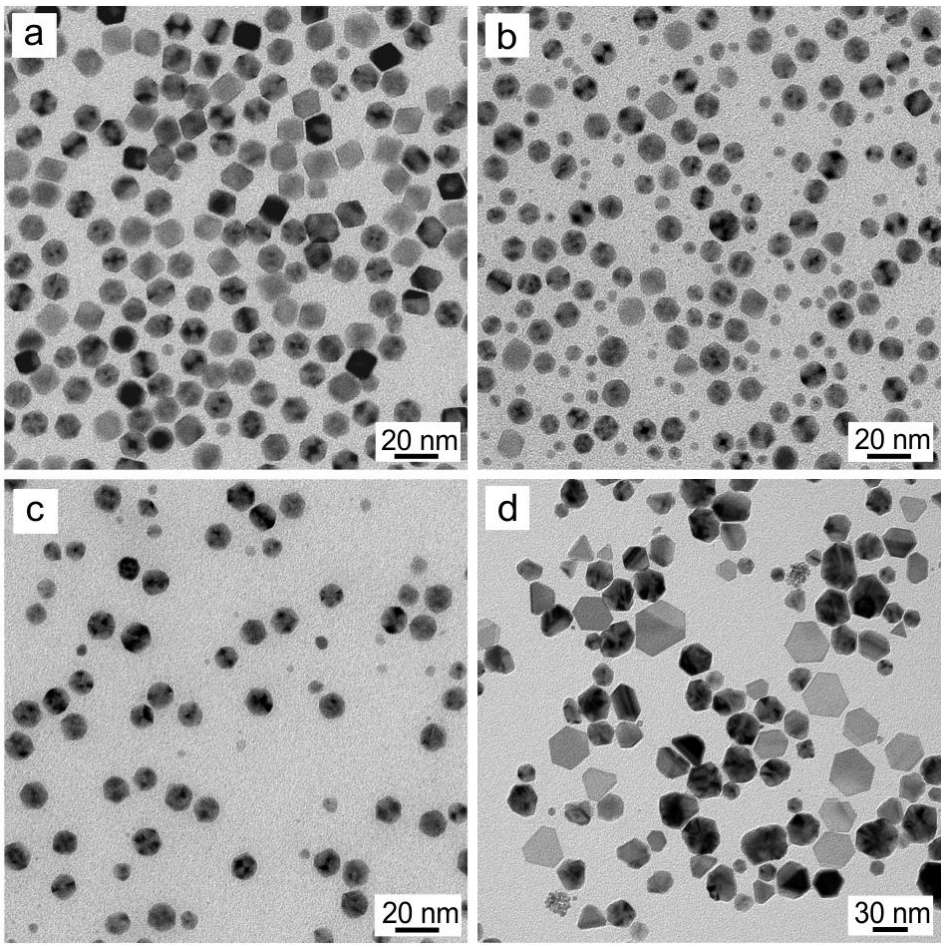

Figure 4.9. TEM images of Pd nanocrystals synthesized using the standard procedure in TEG except the variation in reaction temperature at different initial reduction rates (r_0): (a) r_0=2.46×10^{-5} M·s^{-1} at 160 °C; (b) r_0=1.02×10^{-5} M·s^{-1} at 150 °C; (c) r_0=5.54×10^{-6} M·s^{-1} at 140 °C; and (d) r_0=3.71×10^{-8} M·s^{-1} at 85 °C. (Reprinted with permission from [25]. Copyright 2015 American Chemical Society.)

A set of experiments were also designed to demonstrate how the internal structure of the product in a given synthesis can be controlled by manipulating reduction kinetics and be predicted based on the quantitative correlation shown in Figure 4.8. Specifically, for a synthesis with a known rate constant determined experimentally (or derived from the Arrhenius equation), the critical precursor concentration required for the formation of nanocrystals with a desired internal structure can be readily estimated from the first-order

rate law. For example, when the reaction was conducted in EG at 140 °C with a relatively large rate constant, icosahedrons could still be prepared as long as the concentration of Pd precursor was low enough to ensure that the initial reduction rate was in the range required for the formation of multiply twinned nanocrystals (Figure 4.10, a–b). This

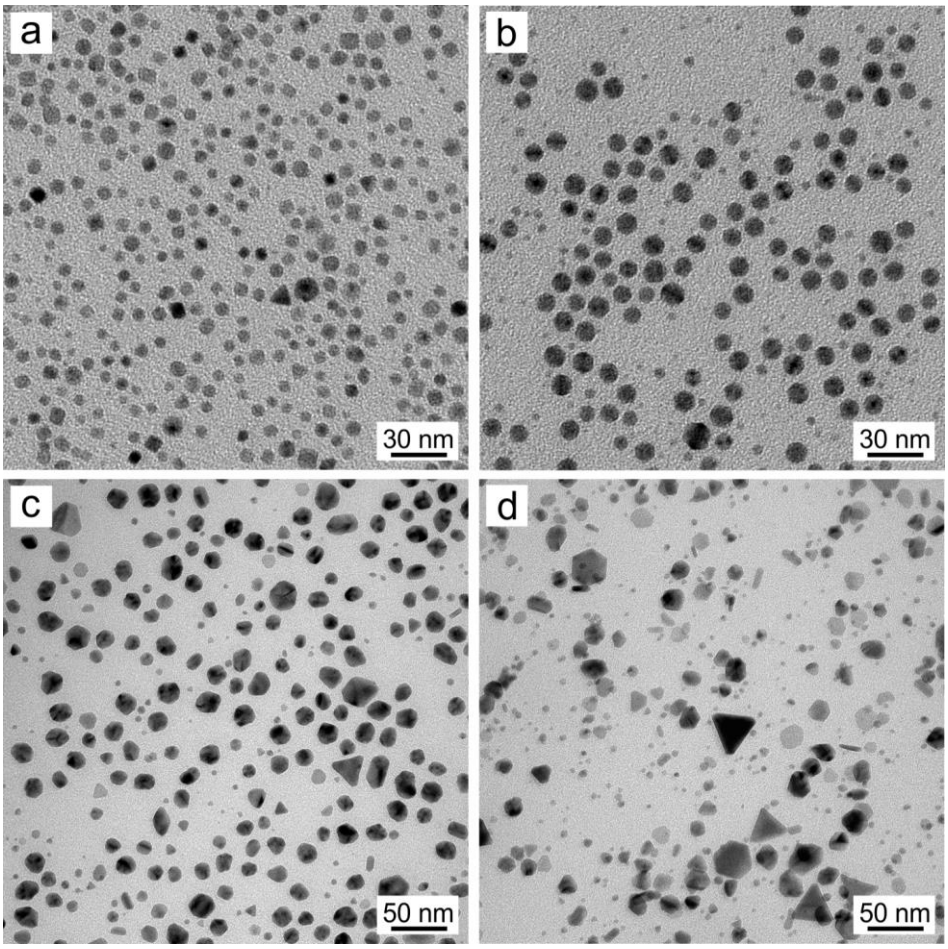

Figure 4.10. TEM images of Pd nanocrystals synthesized using the standard procedure except for the variation in the type of polyol and initial precursor concentration (c_0), and thus different initial reduction rates (r_0): (a) r_0=1.97×10^{-5} M·s^{-1} (in EG, at 140 °C, and c_0=1.76×10^{-3} M); (b) r_0=7.89×10^{-6} M·s^{-1} (in EG, at 140 °C, and c_0=7.04×10^{-4} M); (c) r_0=1.11×10^{-7} M·s^{-1} (in DEG, at 130 °C, and c_0=3.52×10^{-4} M); and (d) r_0=5.56×10^{-8} M·s^{-1} (in DEG, at 130 °C, and c_0=1.76×10^{-4} M). (Reprinted with permission from [25]. Copyright 2015 American Chemical Society.)

strategy was also applicable to the preparation of stacking fault-lined nanoplates in DEG at 130 °C, where the proportions of nanoplates gradually increased when the precursor concentration was reduced from 1.76×10^{-2} M to 3.52×10^{-4} M and 1.76×10^{-4} M, corresponding to initial reduction rates of 1.11×10^{-7} $M\cdot s^{-1}$ and 5.56×10^{-8} $M\cdot s^{-1}$, respectively (Figure 4.10, c−d).

4.3 Summary

In summary, I and my collaborator have developed an effective method for quantitatively analyzing the reaction kinetics involved in a polyol synthesis of noble-metal nanocrystals and further revealed a quantitative correlation between the initial reduction rate and the internal structure taken by seeds and nanocrystals. Such a quantitative correlation allows one to easily control the internal structure and thus shape taken by nanocrystals in a synthesis without trial-and-error modification. With Pd as an example, we have shown that simple spectroscopic measurements could give kinetic parameters involved in the reduction of $PdCl_4^{2-}$ by a polyol, including the rate constant, activation energy, and initial rate. By simply manipulating the initial reduction rate, Pd nanocrystals with distinctive internal structures, including single-crystal, multiply twinned, and stacking fault-lined, could be deterministically obtained in high purity. Despite being unfavorable by thermodynamics, seeds with specific internal structures can still be prepared as kinetically controlled products by manipulating the reaction kinetics. There is a subtle balance between thermodynamic and kinetic controls during the formation of seeds and whichever is in dominance under a given condition will be expressed as the final product. The interplay between thermodynamic and kinetic controls in determining the internal structure and shape of seeds remains to be an actively studied but still poorly understood subject of research. It should be noted that the present approach might not be suitable for syntheses involving complicated or step-by-step

reactions. Nevertheless, this work represents the first attempt to analyze the reaction kinetics involved in a synthesis of noble-metal nanocrystals and to quantitatively correlate the initial reduction rate with the internal structure and shape taken by nanocrystals. Overall, this approach not only greatly advances the understanding of the nucleation and growth of nanocrystals but also paves the way for rational design and deterministic synthesis of nanocrystals with desired and controlled internal structures and shapes.

4.4 Experimental Methods

Polyol syntheses of Pd nanocrystals with different internal structures. The Pd nanocrystals with distinctive internal structures and shapes were prepared using the same procedure, except for the use of different polyols and temperatures to manipulate the reduction rate. Specifically, single-crystal, truncated octahedrons and multiply twinned icosahedrons of Pd, respectively, were obtained in EG (J. T. Baker) and DEG (Aldrich) at 140 °C. Stacking fault-lined nanoplates were prepared in DEG at 75 °C. In a standard procedure, 30 mg of PVP ($M_W \approx 55{,}000$, Aldrich) and 2 mL of EG (or DEG) were added into a glass vial, and heated to the desired temperature in an oil bath under magnetic stirring. Meanwhile, 15.5 mg of Na_2PdCl_4 (98%, Aldrich) was dissolved and preheated in 1 mL of EG (or DEG) at 60 °C. Afterwards, the solution containing Na_2PdCl_4 was quickly injected into the glass vial using a pipette. The reaction times for the synthesis of truncated octahedrons (or icosahedrons) and nanoplates were 3 h and 30 h, respectively. The vial was taken out of the oil bath after the synthesis and cooled down to room temperature. After centrifugation and washing with acetone and water three times, the product was collected and stored in water for further characterization.

Quantitative analysis of reaction kinetics for the synthesis of Pd nanocrystals. The reaction rates between Pd precursor and different polyols were measured by monitoring the absorbance of the reaction solution at different times through UV-vis

spectroscopy. In detail, 2 mL of polyol were added into a glass vial and heated to a certain temperature in an oil bath under magnetic stirring. Na_2PdCl_4 (15.5 mg) was dissolved in 1.0 mL of polyol at 60 °C, and was quickly injected into the vial using a pipette. Meanwhile, the timer started running. An aliquot of 0.3 mL was sampled from the reaction solution at different times using a glass pipette and immediately injected into 2.7 mL of aqueous HCl solution (0.1 M, diluted from 37% HCl, Aldrich) at 0 °C. Then, the solution was centrifuged at 10,000 rpm for 10 min, and the supernatant was diluted into an appropriate concentration with the same aqueous HCl solution (0.1 M) for UV-vis measurement. The time-dependent concentrations of $PdCl_4^{2-}$ ions remaining in the solution could be calculated by comparing the obtained UV-vis spectrum with the standard curve of Na_2PdCl_4. Based on the concentrations of $PdCl_4^{2-}$ ions remaining in the solution as a function of reaction time, the kinetic parameters including the rate constant, initial rate, and activation energy of the reduction of $PdCl_4^{2-}$ by a polyol, could be further acquired.

Characterizations. TEM images were taken using a Hitachi HT7700 microscope operated at 120 kV by drop casting the dispersions of nanocrystals on carbon-coated Cu grids and drying under ambient conditions. HAADF-STEM images were acquired with a JEOL 2200FS STEM/TEM microscope equipped with a CEOS GmbH probe corrector. UV-vis absorption spectra were recorded using a Perkin-Elmer Lambda 750 UV-vis-NIR spectrometer. The concentrations of $PdCl_4^{2-}$ remaining in the reaction solution and thus the conversions of $PdCl_4^{2-}$ into Pd atoms were calculated based on the absorbance at 279 nm from the UV-vis spectra.

4.5 Notes to Chapter 4

Part of this chapter is adapted from the paper “Use of reduction rate as a quantitative knob for controlling the twin structure and shape of palladium nanocrystals” co-authored by Yi Wang and myself and published in *Nano Letters* [25]. As the co-first author of this

paper, I analyzed the kinetic parameters that were derived from the spectroscopic measurement method established by Yi Wang, and carried out the comprehensive study of the correlation between reduction kinetics and the internal structure of Pd nanocrystals.

4.6 References

[1] Xia, Y.; Xiong, Y.; Lim, B.; Skrabalak, S. E. *Angew. Chem., Int. Ed.* **2009**, *48*, 60−103.

[2] Zeng, J.; Zheng, Y.; Rycenga, M.; Tao, J.; Li, Z.-Y.; Zhang, Q.; Zhu, Y.; Xia, Y. *J. Am. Chem. Soc.* **2010**, *132*, 8552−8553.

[3] Chiu, C.-Y.; Li, Y.; Ruan, L.; Ye, X.; Murray, C. B.; Huang, Y. *Nat. Chem.* **2011**, *3*, 393−399.

[4] Wiley, B.; Sun, Y.; Xia, Y. *Acc. Chem. Res.* **2007**, *40*, 1067−1076.

[5] Murphy, C. J.; Sau, T. K.; Gole, A. M.; Orendorff, C. J.; Gao, J.; Guo, L.; Hunyadi, S. E.; Li, T. *J. Phys. Chem. B* **2005**, *109*, 13857−13870.

[6] Xiong, Y.; Xia, Y. *Adv. Mater.* **2007**, *19*, 3385-3391.

[7] Maksimuk, S.; Teng, X.; Yang, H. *J. Phys. Chem. C* **2007**, *111*, 14312−14319.

[8] Barnard, A. S. *J. Phys. Chem. B* **2006**, *110*, 24498−24504.

[9] Sneed, B. T.; Young, A. P.; Tsung, C.-K. *Nanoscale* **2015**, *7*, 12248−12265.

[10] Baletto, F.; Ferrando, R.; Fortunelli, A.; Montalenti, F. *J. Chem.Phys.* **2002**, *116*, 3586−3863.

[11] Barnard, A. S.; Young, N. P.; Kirkland, A. I.; van Huis, M. A.; Xu, F. *ACS Nano* **2009**, *3*, 1431−1436.

[12] Hansen, P. L.; Wagner, J. B.; Helveg, S.; Rostrup-Nielsen, H. R.; Clausen, B. S.; Topsøe, H. *Science* **2002**, *295*, 2053−2055.

[13] Kim, F.; Connor, S.; Song, H.; Kuykendall, T.; Yang, P. *Angew. Chem., Int. Ed.* **2004**, *43*, 3673−3677.

[14] Seo, D.; Yoo, C. I.; Chung, I. S.; Park, S. M.; Ryu, S.; Song, H. *J. Phsy. Chem. C*

2008, *112*, 2469−2475.

[15] Baletto, F.; Ferrando, R. *Rev. Mod. Phys.* **2005**, *77*, 371−423.

[16] Wang, Y.; He, J.; Liu, C.; Chong, W. H.; Chen, H. *Angew. Chem., Int. Ed.* **2015**, *54*, 2022−2051.

[17] Zheng, Y.; Zeng, J.; Ruditskiy, A.; Liu, M.; Xia, Y. *Chem. Mater.* **2014**, *26*, 22−33.

[18] Lv, T.; Wang, Y.; Choi, S.-I.; Chi, M.; Tao, J.; Pan, L.; Huang, C. Z.; Zhu, Y.; Xia, Y. *ChemSusChem* **2013**, *6*, 1923−1930.

[19] Huang, H.; Wang, Y.; Ruditskiy, A; Peng, H.-C.; Zhao, X.; Zhang, L.; Liu, J.; Ye, Z.; Xia, Y. *ACS Nano* **2014**, *8*, 7041−7050.

[20] Timoshkin, A. Y.; Kudrev, A. G. *Russ. J. Inorg. Chem.* **2012**, *57*, 1362−1370.

[21] Wojnicki, M.; Pacławski, K.; Rudnik, E.; Fitzner, K. *Hydrometallurgy* **2011**, *110*, 56−61.

[22] Luty-Błocho, M.; Pacławski, K.; Wojnicki, M.; Fitzner, K. *Inorg. Chim. Acta* **2013**, *395*, 189–196.

[23] Besson, C.; Finney, E. E.; Finke, R. G. *Chem. Mater.* **2005**, *17*, 4925−4938.

[24] Xia, X.; Xie, S.; Liu, M.; Peng, H.-C.; Lu, N.; Wang, J.; Kim, M. J.; Xia, Y. *Proc. Natl. Acad. Sci. USA* **2013**, *110*, 6669−6673.

[25] Wang, Y.[†]; Peng, H.-C.[†];([†]equal contribution) Liu, J.; Huang, C. Z.; Xia, Y. *Nano Lett.* **2015**, *15*, 1445−1450.

CHAPTER 5

TOWARD A QUANTITATIVE UNDERSTANDING OF SYMMETRY BREAKING INVOLVED IN THE SEED-MEDIATED GROWTH OF PALLADIUM NANOCRYSTALS

5.1 Introduction

Although notable progress has been made in recent years with regard to the development of methods for controlling the shapes of noble-metal nanocrystals [1-4], as discussed in Chapter 1, it is still a challenge to generate nanocrystals with less symmetric shapes relative to the cubic lattice of a noble metal. When reduced in symmetry, the nanocrystals are anticipated with new properties to enrich fundamental studies and enable new applications. Notable examples include Au nanorods with tunable surface plasmon resonance peaks in the near-infrared region for photothermal treatment [5−8]; Ag nanowires with high transparency in the visible region for the fabrication of touchscreens, energy-efficient solar cells, smart windows, and flexible electronic devices [9−12]; and Pt icosahedrons with high catalytic activity toward the oxygen reduction reaction [13, 14]. These and other examples clearly demonstrate the critical importance of understanding the phenomenon of symmetry breaking in engineering the properties of nanocrystals for various applications.

In contrast to an inorganic compound such as ZnO [15, 16], the crystal seeds of a noble metal often have multiple facets equivalent to each other in terms of spatial arrangement and coordination number for the surface atoms. The high symmetry makes it inherently challenging to obtain noble-metal nanocrystals with shapes lower in symmetry than a cubic lattice. As a result, for noble-metal nanocrystals with a single-crystal structure, they often take a polyhedral (*e.g.*, cubic, cuboctahedral, or octahedral) shape as confined by the cubic symmetry of the crystal lattice [1−4]. There are also reports for a

number of noble metals, including Au [17−19], Pd [20, 21], and Ag [22, 23], in which single-crystal nanostructures with a one-dimensional morphology (*e.g.*, nanorods and nanobars) could be synthesized in the presence of Br^- or other halide ions. In spite of extensive research, the exact mechanism responsible for the anisotropic, one-dimensional growth is still under debate. It is generally believed that the halide ions could somehow induce a faster growth rate along one of the three directions, leading to symmetry breaking and thus the formation of nanostructures with reduced symmetry relative to the cubic lattice.

With the use of a syringe pump to introduce the precursor solution, our group recently demonstrated an alternative strategy for breaking the cubic symmetry by manipulating the reaction kinetics involved in a seed-mediated growth process [24−26]. This strategy is effective not only for the generation of nanocrystals with reduced symmetry relative to the cubic lattice but also in avoiding self-nucleation [27−30]. In addition to the deposition on a seed, the newly formed atoms can self-nucleate and grow into nanocrystals concurrently if the concentration of atoms exceeds the threshold for self-nucleation, leading to the formation of nanocrystals with poorly controlled sizes and shapes. By using a syringe pump to introduce the precursor dropwise into a growth solution, the concentration of the newly formed atoms could be maintained at a level lower than the threshold to effectively suppress self-nucleation. More significantly, when the atoms initially formed in the growth solution are smaller in number than the seed particles, heterogeneous nucleation can only occur at a limited number of the equivalent sites on a seed to trigger a growth pattern deviated from the cubic symmetry. For example, by controlling the injection rate of the precursor solution, Zeng and coworkers demonstrated that Ag or Au could be selectively deposited on different numbers of side faces (from one to six) of a Pd cubic seed to generate a nanocrystal with an asymmetric distribution for the deposited element [24, 25]. When a similar strategy was applied to the growth of Ag on Ag cubic seeds, Ag nanocrystals with reduced symmetry relative to its cubic lattice,

including rectangular bars and semitruncated octahedrons, were obtained [26]. Despite these successful demonstrations, it should be pointed out that all these studies were based on trial-and-error manipulation of the experimental parameters due to the lack of a mechanistic understanding and quantitative control. It is highly desired to have a quantitative understanding of the symmetry breaking phenomenon, especially, with regard to the relationship between the growth mode and the reaction kinetics involved in seed-mediated growth.

Herein, I report a quantitative study of the symmetry breaking phenomenon involved in the seed-mediated growth of Pd nanocrystals. As discussed in Chapter 3, through the use of seeds with a well-defined internal structure, one could systematically examine the roles of various thermodynamic and kinetic parameters in controlling the evolution of seeds into nanocrystals exhibiting distinctive shapes. The experimental approach in this study relies on the use of a syringe pump to introduce precursor ions dropwise into a growth solution containing well-defined seeds at a controllable rate to achieve a steady state for the number of precursor ions in the solution. Based on the reduction rate constant determined experimentally, the number of precursor ions in each drop (or the stock solution), and the duration of time between adjacent drops, I was able to obtain the kinetic information about a given synthesis, including the number of precursor ions in the growth solution as a function of the reaction time, as well as the lower and upper limits for the steady state. My results indicate that the lower limit of precursor ions for the steady state plays a deterministic role in inducing symmetry breaking in a seed-mediated growth process. The lower limit has to be kept below a critical value in order to achieve asymmetric nucleation on a seed. At the same time, the lower limit has to be sufficiently high to ensure that the atoms are deposited at a rate faster than surface diffusion during the entire growth process. Otherwise, the surface diffusion of adatoms will eventually lead to the formation of a nanocrystal with symmetry similar to that of the seed. It should be noted that previous studies only reported that a relatively slow atom deposition rate is

critical to the induction of asymmetric growth [24−26]. The present work indicates that the atom deposition rate for asymmetric growth needs to be kept in a narrow range in order to induce and sustain the asymmetric growth mode. Most importantly, with the availability of reduction rate constant, it is possible to predict the experimental conditions (*e.g.*, the injection rate and the precursor concentration) under which the growth mode will be switched from symmetric to asymmetric, and vice versa.

5.2 Results and Discussion

Kinetic Parameters for the Reduction of a Pd(II) Precursor by AA. To quantitatively understand the effects of reaction kinetics on the transition from a symmetric to an asymmetric growth mode, it is necessary to tightly control the reduction rate for the Pd(II) precursor and thus the deposition rate for the resultant atoms. As discussed in Chapter 4, because of the involvement of collision and electron transfer between the Pd(II) precursor and AA, the reduction rate is expected to follow a second-order rate law and thus directly proportional to the concentrations of both reagents [31]. Herein, I further achieved a pseudo-first-order rate law by supplying the concentration of AA in great excess relative to the Pd(II) precursor. The excess amount of reducing agent in the system not only ensures a pseudo-first-order rate but also enables quick reduction of the Pd(II) precursor ions into Pd(0) atoms. Under this assumption, the rate law can be expressed as

$$r = k' [\mathrm{AA}] [\mathrm{Pd(II)}] = k [\mathrm{Pd(II)}] \qquad (5.1)$$

where k is the combined rate constant.

The combined rate constant can be obtained by plotting the instantaneous concentration of the Pd(II) precursor remaining in the reaction solution as a function of the reaction time [32]. Unlike a polyol synthesis conducted at an elevated temperature

(See Chapter 4), the strong reducing power of AA at room temperature makes it difficult to quench the reduction reaction in the current study by quickly cooling down the reaction solution. Thanks to the high stability of $PdBr_4^{2-}$ [33−35], the Pd(II) precursor can be prevented from being reduced by AA at room temperature for a relatively long period of time up to at least 60 min by adding a highly concentrated KBr solution (500 mg/mL) into the reaction solution. To validate the effectiveness of this quenching procedure, I conducted a control experiment, in which an aqueous Na_2PdCl_4 solution (1.0 mg/mL) was injected into another aqueous solution containing both AA (33.3 mg/mL) and KBr (500 mg/mL) at 40 ℃. Aliquots were then sampled from the solution for measuring the concentrations of Pd(II) ions by ICP-MS analysis. Figure 5.1a shows a plot of the concentration of Pd(II) ions remaining in the solution as a function of time, indicating that essentially no Pd(II) was reduced by AA when there were excess Br^- ions in the solution even after they had been mixed for 60 min. I then applied this method to measure the reaction kinetics involving the reduction of the Pd(II) precursor by AA at 40 ℃ in an aqueous solution. Figure 5.1b shows a plot of $\ln[Pd(II)]_t$ as a function of reaction time, indicating that the reduction indeed occurred as a first-order reaction with respect to the Pd(II) precursor. From the linear plot, I obtained a combined rate constant of 0.635 s^{-1} for the reduction of the Pd(II) precursor by AA at 40 ℃. It should be pointed out that the actual Pd(II) precursor involved in the reduction could be a mixed-ligand complex (*i.e.*, $PdCl_xBr_{4-x}^{2-}$, x=1, 2, and 3) due to the rapid ligand exchange between $PdCl_4^{2-}$ and Br^- and that the exact composition is determined by the relative molar ratio of Cl^- to Br^- in the reaction solution [35]. In the present work, I added an excess amount of KBr into the reaction solution to ensure that the Pd(II) ions were essentially in the form of $PdBr_4^{2-}$ due to a complete ligand exchange and a fixed composition for the Pd(II) precursor for all the seed-mediated syntheses described below.

It should be pointed out that some species other than Pd(II) ions, such as ultrafine particles and clusters (*i.e.*, the nuclei), might remain in the supernatant because it might

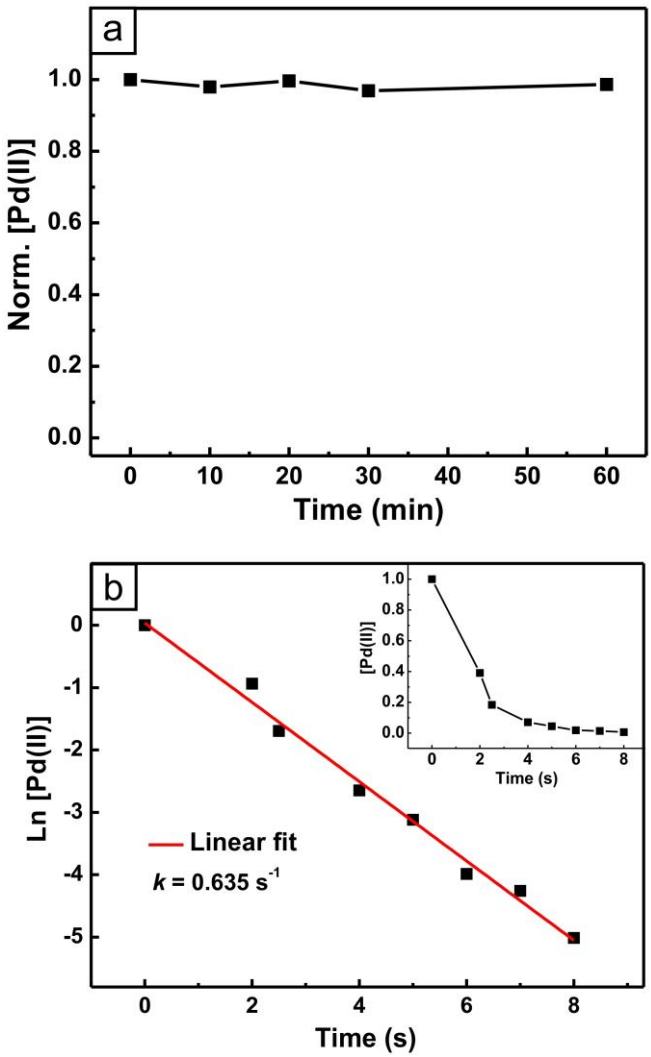

Figure 5.1. (a) ICP-MS analysis of the concentration of Pd(II) ions remaining in the reaction solution at different time points of a control experiment, indicating that the reduction of Pd(II) ions could be effectively quenched in the presence of Br^- ions at a concentration of 4.2 M (or 500 mg/mL in terms of KBr). (b) A plot of ln[Pd(II)] as a function of reaction time, giving a straight line with a slope that equals $-k$. The inset shows the concentration of Pd(II) ions remaining in the reaction solution as a function of reaction time. Note that the concentrations used in the plot were normalized to the initial concentration. (Reprinted with permission from [43]. Copyright 2015 American Chemical Society.)

be difficult to precipitate them out by centrifugation. As a consequence, ICP-MS analysis of the supernatant might not reflect the true concentration of the precursor. However, giving their high activity and the absence of a colloidal stabilizer (e.g., PVP) in the kinetic measurements, the concentration of Pd ultrafine particles or clusters should be extremely low in the reaction solution. Otherwise, they would readily grow or aggregate into larger particles. To address this potential issue, I conducted UV-vis and XPS analysis to confirm the actual species in the supernatant. As shown in Figure 5.2, the UV-vis spectrum of the supernatant exhibits the same absorption features as the precursor solution, confirming that the supernatant only contained the unreacted precursor ions.

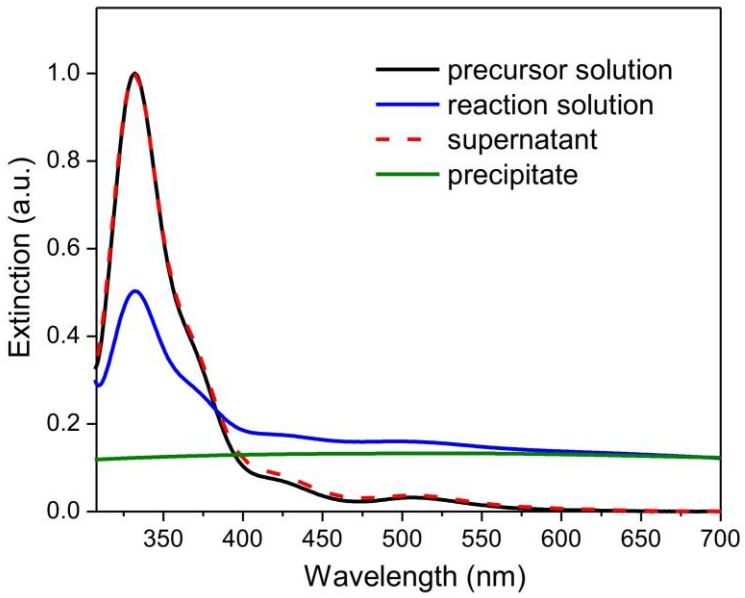

Figure 5.2. UV-vis spectra of the Na_2PdCl_4 precursor dissolved in KBr solution, the reaction solution of a standard synthesis before centrifugation, and the supernatant and precipitate after separation through centrifugation. For the purpose of comparison, UV-vis spectra of the precursor and supernatant were normalized against the peak extinction. (Reprinted with permission from [43]. Copyright 2015 American Chemical Society.)

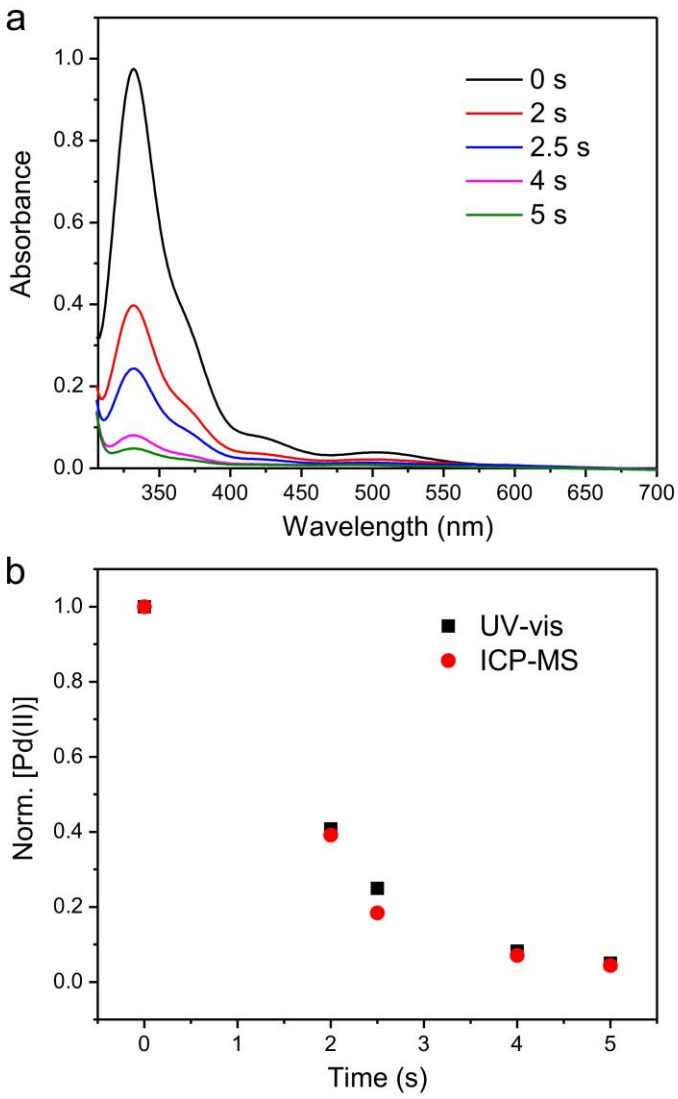

Figure 5.3. (a) UV-vis spectra of the supernatants obtained at different reaction stages of a standard synthesis. (b) A plot showing the concentration of Pd(II) ions remaining in the reaction solution, measured using UV-vis (from the absorbance at 332 nm) and ICP-MS methods, as a function of reaction time. (Reprinted with permission from [43]. Copyright 2015 American Chemical Society.)

The absence of a continuous band in the visible region, which is typically associated with the absorption/scattering of Pd nanocrystals, also suggests that there was essentially no detectable amount of Pd ultrafine particles or clusters in the supernatant. I also used the UV-vis method to derive the reduction kinetics by recording the absorption spectra of the supernatants obtained at different stages of a standard synthesis and determine the concentration of Pd(II) ions using a calibration curve. As shown in Figure 5.3, there is good agreement between the data obtained using the UV-vis and ICP-MS methods. The absence of Pd(0) species in the supernatant was further confirmed by XPS analysis (Figure 5.4). At least, it can be claimed that the concentration of Pd(0) species was below the detection limit of XPS and can thus be neglected in analyzing the reduction kinetics. Taken together, I believe that it is reasonable to exclude the possible errors arising from the negligible amount of Pd(0) species present in the supernatant during the measurement of reduction kinetics by ICP-MS.

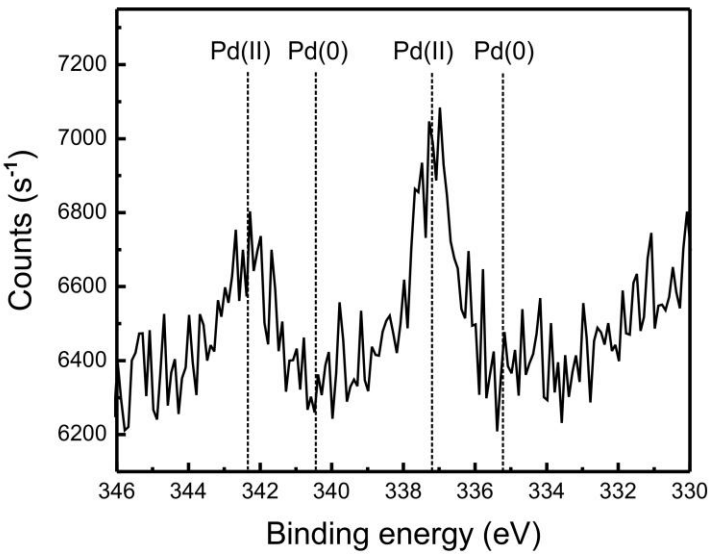

Figure 5.4. High-resolution Pd 3d XPS spectrum of the supernatant of a standard synthesis, indicating that there was only Pd(II) species in the supernatant. The sample for XPS measurement was prepared by freeze-drying. (Reprinted with permission from [43]. Copyright 2015 American Chemical Society.)

Kinetic Analysis of Seed-Mediated Growth under the Dropwise Addition of a Precursor. Figure 5.5a shows a schematic illustration of the experimental approach used in the present study, where two aqueous solutions containing the Pd(II) precursor and AA (a reducing agent), respectively, are simultaneously injected at a controlled rate from two syringe pumps into an aqueous suspension containing the seeds, KBr (a capping agent), and PVP (a colloidal stabilizer). Several experimental parameters, including the number of the Pd(II) precursor ions in each drop and the duration of time between adjacent drops, can be manipulated by changing the precursor concentration and tuning the injection rate, respectively, to tailor the reaction kinetics.

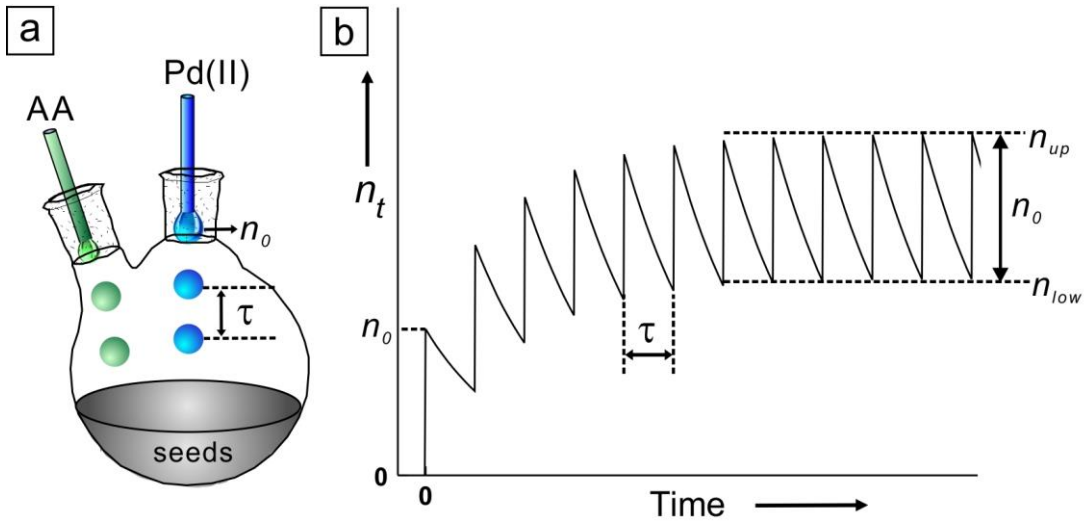

Figure 5.5. (a) A schematic illustration of the experimental setup used for seed-mediated growth with the dropwise addition of a precursor solution. (b) A plot showing the instantaneous number of Pd(II) ions (the precursor) in the growth solution (n_t) as a function of the reaction time (t), the duration of time between adjacent drops (τ), and the number of precursor ions contained in each drop (n_0). After the introduction of the first few drops, n_t will reach a steady state defined by an upper-limit (n_{up}) and a lower-limit (n_{low}). Note that the values of n_t, n_0, n_{up}, and n_{low} are all normalized to the number of seeds in the growth solution. (Reprinted with permission from [43]. Copyright 2015 American Chemical Society.)

Given that the fraction of the total amount of precursor ions that will be reduced per unit time is independent of the initial precursor amount (or concentration) for a first-order reaction, the consumption of precursor from each drop can be derived separately. Mathematically, the total number of Pd(II) precursor ions remaining in the growth solution at time *t* can be expressed as a sum of contributions from all drops added up to this time point:

$$n_t = n_0 e^{-kt} + n_0 e^{-k(t-\tau)} + n_0 e^{-k(t-2\tau)} + \cdots + n_0 e^{-k(t-N\tau)} = \frac{n_0 e^{-kt} \times \left(1-\left(e^{k\tau}\right)^{N+1}\right)}{1-e^{k\tau}} \qquad (5.2)$$

where n_t represents the instantaneous number of the Pd(II) precursor ions in the reaction solution; n_0 is the number of the Pd(II) precursor ions in each drop (*i.e.*, in the stock solution); k is the combined rate constant derived from the ICP-MS analysis; t is the reaction time; τ is the duration of time between adjacent drops, and N is the total number of drops added into the solution up to time t. For the purpose of simplicity, here I normalized the numbers of the Pd(II) ions, both n_0 and n_t, to the number of seed particles in the growth solution, which was determined through a combination of TEM imaging and ICP-MS analysis.

When the precursor and the reducing agent for a seed-mediated growth process are fixed, the instantaneous number of the Pd(II) ions at different time points can be calculated using Eq. (5.2) for any pair of n_0 and τ. Figure 5.5b shows a generic plot for the instantaneous number of the Pd(II) ions in the growth solution as a function of the reaction time. If the duration of time between adjacent drops is sufficiently long, most of the Pd(II) ions will have been reduced to Pd(0) atoms and thus depleted from the growth solution before the next drop is introduced. In comparison, if the duration of time is relatively short, not all of the Pd(II) ions will be reduced before the next drop is introduced, and the precursor ions will be gradually accumulated in the growth solution

as the number of drops is increased. In this case, after a few drops, the instantaneous number of the precursor ions will reach a steady state, in which it only oscillates between a lower limit (n_{low}) and a upper limit (n_{up}). Specifically, each time a drop of the precursor solution is introduced during the steady state, the number of the precursor ions will quickly increase from n_{low} to n_{up}, followed by an exponential decay from n_{up} to n_{low} until the next drop is introduced. The difference between n_{up} and n_{low} simply equals n_0. The values of n_{up} and n_{low} can be easily calculated using Eqs. (5.3) and (5.4):

$$n_{up} = \frac{n_0}{1-e^{-k\tau}} \tag{5.3}$$

$$n_{low} = \frac{n_0 \cdot e^{-k\tau}}{1-e^{-k\tau}} \tag{5.4}$$

For the seed-mediated growth involving one-shot injection of the precursor solution [36−39], the number of the precursor ions typically shows a drastic decrease during the course of growth. In comparison, the use of a syringe pump provides an opportunity to add the precursor solution dropwise and thereby enable one to maintain the precursor concentration in a steady state. Since the reduction rate is directly proportional to the number of precursor ions in a pseudo-first-order reaction, the steady state enabled by the dropwise injection of precursor ions allows one for a tight control over the reduction rate and thereby the atom deposition rate within a narrow range. In this way, I was able to achieve a quantitative understanding of the correlation between the growth mode and the reaction kinetics in a seed-mediated growth process.

The Role Played by the Number of Pd(II) Precursor Ions in Each Drop (n_0). To understand the role of n_0 in controlling the shape of Pd nanocrystals derived from seed-mediated growth, I conducted a set of experiments with different precursor concentrations. As reported in previous studies, a relatively low concentration for the

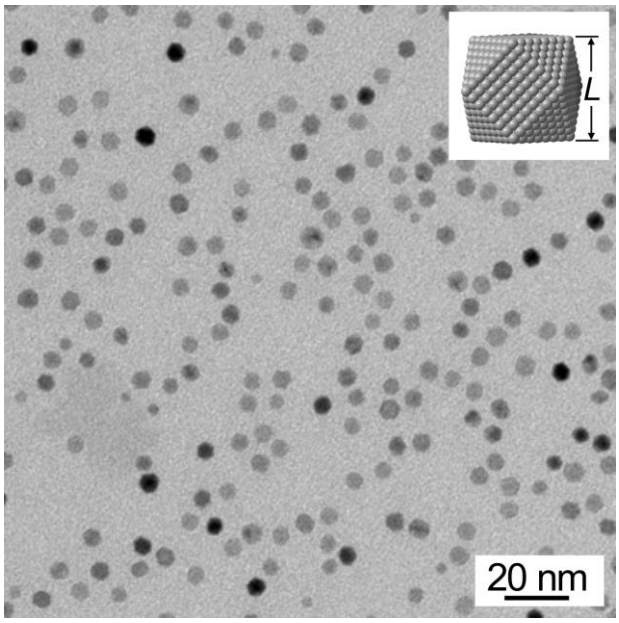

Figure 5.6. TEM image of Pd cuboctahedrons with an average size (L) of 4.5 nm that served as the seeds for most of the syntheses described in this chapter. The inset shows an atomic model of a cuboctahedron and the definition of size. (Reprinted with permission from [43]. Copyright 2015 American Chemical Society.)

precursor was required in order to induce asymmetric growth [24−26]. Unlike conventional seed-mediated growth, where thousands of precursor ions per seed particle are introduced into the growth solution for each drop (*i.e.*, $n_0 > 10^3$) [40], I set n_0 to a much smaller number between 4.7 and 70.5 in the present work to achieve asymmetric growth. Initially, I focused on the growth of Pd on single-crystal Pd cuboctahedral seeds with an average size of 4.5 nm (Figure 5.6) in the presence of Br^- ions. Owing to the preferential capping of Pd(100) surface by the Br^- ions as discussed in Chapter 2 [41], it is expected that the introduction of Br^- ions will alter the order of surface free energies between different facets and thus facilitate the formation of Pd nanocubes enclosed by {100} facets. Figure 5.7 shows TEM images of the resultant Pd nanocrystals. In addition

to perfect nanocubes, the products also contained nanobars where one of the directions was elongated and thus the cubic symmetry was reduced. Since the degree of symmetry of the resultant Pd nanocrystals reflects the mode of growth during a seed-mediated growth process, I used TEM images to analyze the shape of particles in the product (see Figures 5.8 and 5.9 for details). Specifically, the proportion of cubic structures showed a negative correlation with n_0. For example, when n_0 was an extremely small number (4.7), the majority (78%) of nanocrystals in the final product was perfect nanocubes with symmetry consistent with the lattice (Figure 5.7a). With the increase of n_0, the products were gradually transformed from perfect nanocubes to less symmetric, elongated nanocubes (*e.g.*, nanobars). As shown in Figure 5.7, b−d, the percentage of perfect nanocubes in the products decreased from 78% to 54%, 27%, and 16% as n_0 was increased from 4.7 to 11.7, 23.5, and 70.5, demonstrating a transition of the growth mode. In addition, I note that there were a few particles with uncommonly small sizes compared to the others in the TEM images, indicating that self-nucleation was not completely suppressed, possibly due to the transient, local high concentration of precursor ions when each drop of precursor is added into the growth solution. However, considering that the majority of particles in the product still grew from the seeds, I believe that it was mostly based on heterogeneous nucleation and thus the minor self-nucleation process should have no impact on the overall growth mode of a synthesis.

Because the value of n_0 will affect the reaction kinetics, I hypothesize that the change in growth mode can be attributed to the variation of instantaneous precursor ion number in the steady state. In order to quantitatively study the effect of the number of precursor ions supplied by each drop on the growth mode, I simulated the reaction kinetics under different values of n_o using Eq. (5.2). As shown in Figure 5.7e, the number of precursor ions in the growth solution reached a steady state after the first few drops. Specifically, different values of n_0 resulted in steady states characterized by different ranges of n_{up} and n_{low}. For example, in the case of n_0=4.7, the oscillation was confined to the range of 2.2

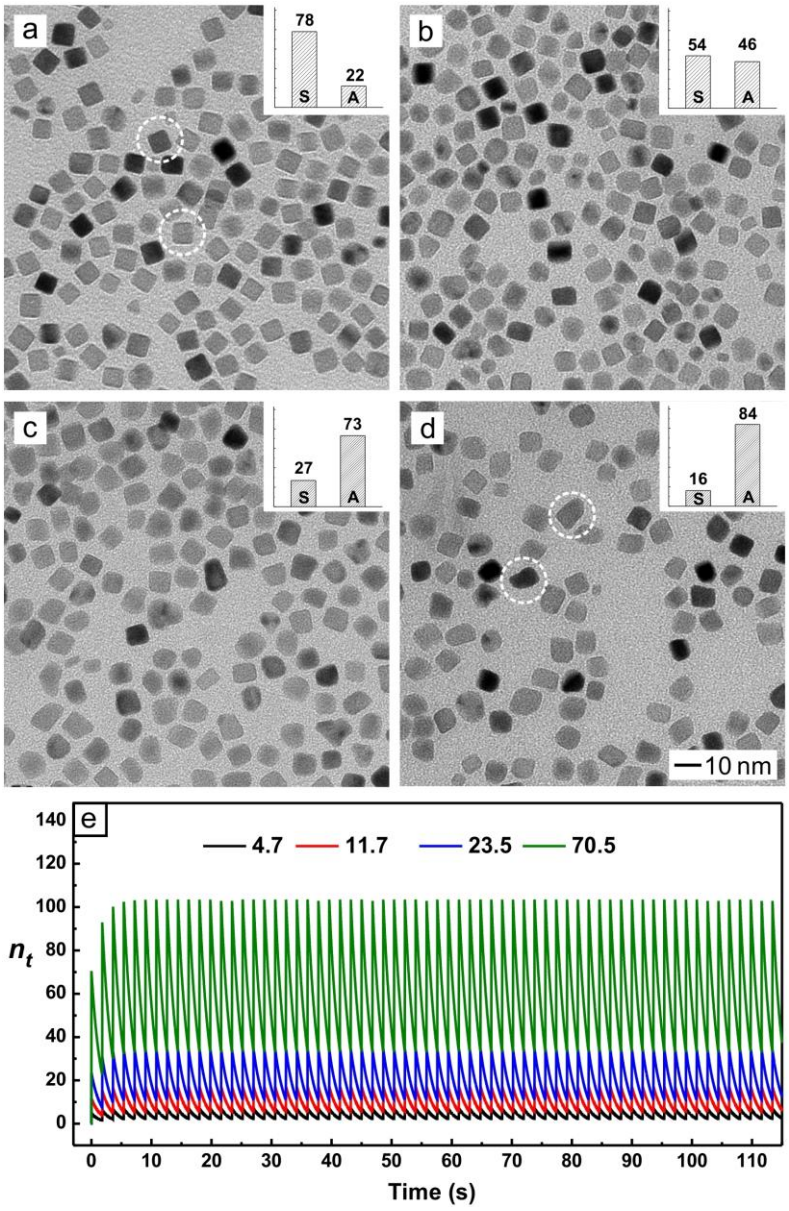

Figure 5.7. Controlling the mode of growth by changing the initial concentration of the precursor: (a−d) TEM images of Pd nanocrystals obtained by introducing the Pd(II) precursor solutions with different concentrations at an injection rate of 30 mL/h (τ=1.8 s). The numbers of Pd(II) precursor ions contained in each drop (n_0, normalized to the number of seeds in the growth solution) were (a) 4.7, (b) 11.7, (c) 23.5, and (d) 70.5, respectively. The inset in each panel shows a histogram distribution of the nanocrystals with symmetric (S) and asymmetric (A) structures, respectively. (e) The simulated numbers of precursor ions as a function of the reaction time. The circles in (a) indicate the products of *symmetric growth* and the circles in (d) mark the products of *asymmetric growth*. (Reprinted with permission from [43]. Copyright 2015 American Chemical Society.)

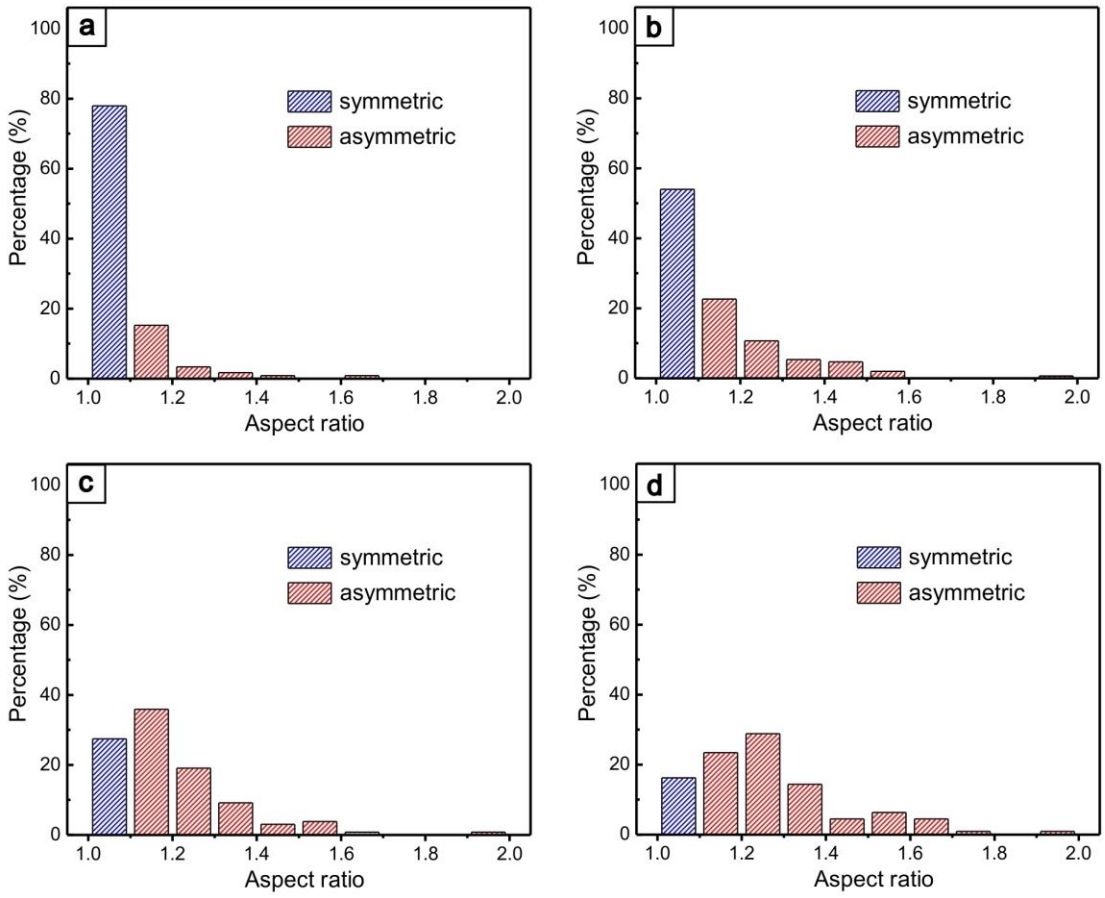

Figure 5.8. Histograms showing the distribution of aspect ratio for the particles in the four samples shown in Figure 5.7. Note that an aspect ratio of 1.1 was defined as the borderline between symmetric and asymmetric growth. (Reprinted with permission from [43]. Copyright 2015 American Chemical Society.)

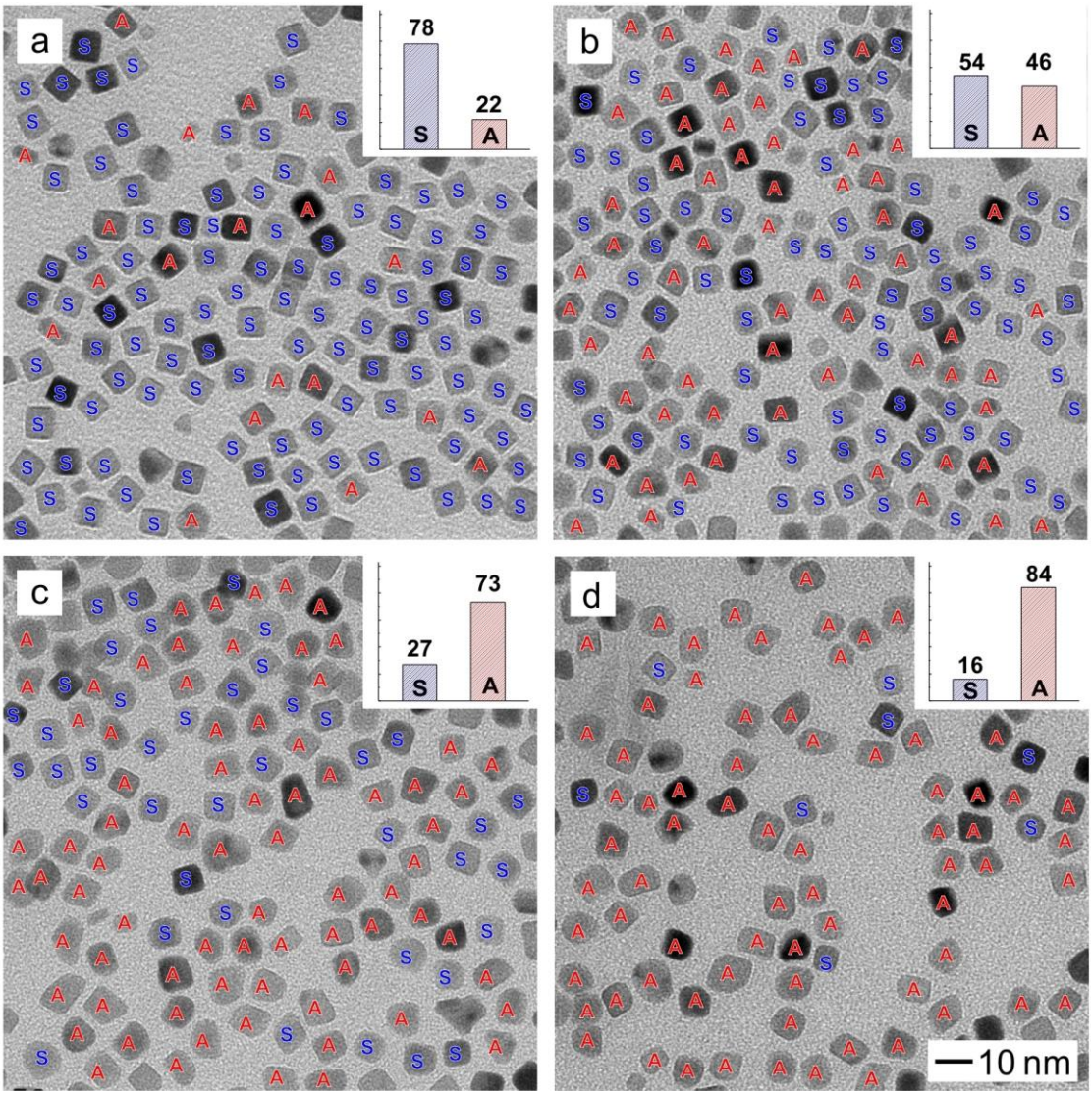

Figure 5.9. TEM images of samples shown in Figure 5.7 with all particles labeled as symmetric(S) or asymmetric (A). Note that the twinned particles were excluded in the analysis and not labeled. (Reprinted with permission from [43]. Copyright 2015 American Chemical Society.)

(n_{low}) to 6.9 (n_{up}). In contrast, when n_0 was increased to 70.5, the values of n_{low} and n_{up} increased to 33 and 103.5, respectively. These results indicate that there was a transition from symmetric growth to asymmetric growth when the numbers of the precursor ions involved in the steady state were increased.

The Role Played by the Duration of Time between Adjacent Drops. In the second set of experiments, I adjusted τ by tuning the injection rate of precursor solution while keeping all other experimental parameters, including n_0 and reaction temperature, the same as the standard procedure. Based on Eq. (5.2), the value of n_t in the growth solution has a negative correlation with τ. Therefore, it is expected that shortening the duration of time between adjacent drops will increase the values of n_{up} and n_{low} in the steady state. Figures 5.10, a and b, shows TEM images of Pd nanocrystals synthesized using the protocol with n_0=4.7, the same as in Figure 5.7a except that the durations of time between adjacent drops were shortened from 1.8 s to 0.9 s and 0.45 s, respectively. The majority of product gradually changed from perfect cubes to elongated cubes with reduction in symmetry as the duration of time was decreased. Specifically, an analysis of the corresponding products indicate that the percentage of perfect nanocubes dropped from 78% to 36% as the duration of time was shortened from 1.8 s to 0.9 s, and eventually reached 18% when a very short duration of 0.45 s was involved. The simulation of reaction kinetics given in Figure 5.10c confirms the increase in n_{up} and n_{low} for the steady state as the duration of time between adjacent drops was shortened.

I also applied a similar analysis to the synthesis shown in Figure 5.7c, where n_0 was set to 23.5 and the product was dominated by elongated cubes with reduced symmetry relative to the cubic lattice. As shown in Figure 5.10d, when the duration of time between adjacent drops was increased from 1.8 s to 3.6 s, the proportion of cubic structures increased from 27% to 76%. Finally, it reached 88% when the duration was increased to 10.5 s, and the product mainly contained perfect cubes (Figure 5.10e). Due to the relatively long duration of time in the case of τ=10.5 s, most of the precursor should have

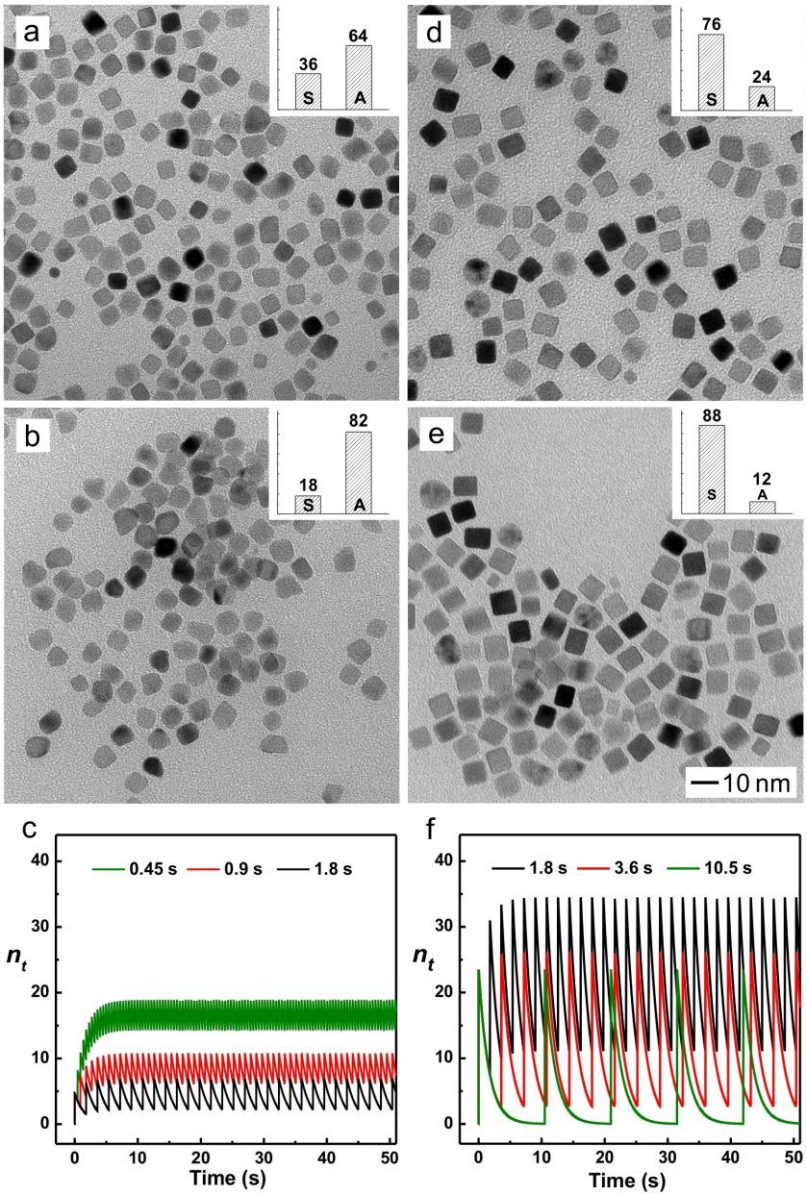

Figure 5.10. Controlling the mode of growth by varying the precursor injection rate to change the duration of time between adjacent drops: (a, b) TEM images of Pd nanocrystals prepared by injecting a Na_2PdCl_4 solution of 0.1 mg/mL, where the number of Pd(II) precursor ions in each drop (n_0, normalized to the number of seeds) was 4.7. The durations of time between adjacent drops (τ) were: (a) 0.9 s and (b) 0.45 s, respectively. (d, e) TEM images of Pd nanocrystals obtained by injecting a Na_2PdCl_4 solution of 0.5 mg/mL, corresponding to a value of 23.5 for n_0. The values of τ were: (d) 3.6 s and (e) 10.5 s, respectively. The inset in each TEM image shows a histogram distribution of the symmetric and asymmetric structures. (c, f) The simulated numbers of precursor ions as a function of the reaction time. (Reprinted with permission from [43]. Copyright 2015 American Chemical Society.)

been depleted before the next drop was introduced, resulting in an extremely low value of 0.03 for the n_{low} in the steady state. This significant change to the morphology of the resultant nanocrystals can also be attributed to the change in reaction kinetics, as documented in Figure 5.10f, where the increase in τ effectively decreased the values of n_{up} and n_{low} and thereby slowed down the overall atom deposition rate.

The Correlation between Growth Mode and n_{low}. It is now clear that the switching of seed-mediated growth from a symmetric to an asymmetric mode can be achieved using two different methods that involve variations to the number of precursor ions in each drop and/or the duration of time between adjacent drops. To achieve a better understanding toward the explicit mechanism, I made a side-by-side comparison of the results and the reaction kinetics from the aforementioned two methods in an effort to single out a key factor responsible for the switching of the growth mode. Interestingly, both methods show a common transition point around n_{low}=8 that separates the two distinctive growth modes in the current system.

Because n_{low} is a function of both n_0 and τ, a curve representing a specific value of n_{low} can be made in a plot of n_0 *versus* τ. As shown in Figure 5.11a, the solid line indicates the boundary of n_{low}=8, with the left side being greater than 8 and the rest being less than 8. By correlating the values of n_{low} and the proportions of symmetrically reduced particles under different conditions, a transition between the two growth modes can be clearly observed along the boundary (Figure 5.11b). Specifically, when n_{low} was greater than 8 in a given synthesis, the majority of nanocrystals in the product would be characterized as elongated nanocubes with reduced symmetry, indicating that asymmetric growth dominated in this region. In comparison, when n_{low} was less than 8, the growth would be switched to symmetric mode, together with the formation of perfect cubes. For the region close to the boundary, the resultant product would be a mixture of nanocrystals with symmetric and asymmetric structures at approximately equal proportions, demonstrating the coexistence of both growth modes under these conditions.

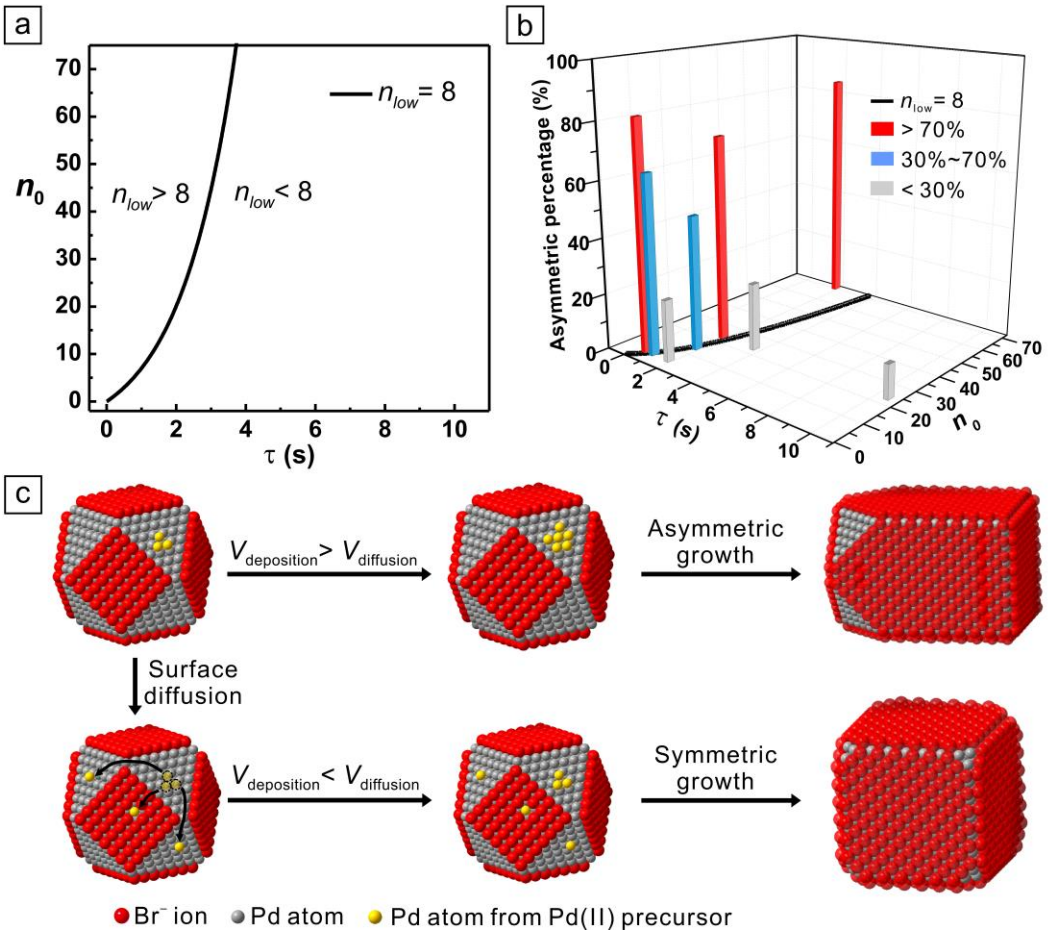

Figure 5.11. (a) A plot showing n_{low} (the lower limit of the number of precursor ions in the steady state of a synthesis) as a function of n_0 (the number of precursor ions contained in each drop) and τ (the duration of time between adjacent drops). (b) A bar chart showing the percentages of asymmetric structures formed under different reaction conditions, suggesting a transition of growth from an asymmetric mode to a symmetric mode when n_{low} was reduced to pass a critical value around 8. Note that the values of both n_{low} and n_o are all normalized to the number of seeds in the growth solution. (c) A schematic illustration showing the effect of reaction kinetics and surface diffusion on the growth mode of a Pd cuboctahedral seed. (Reprinted with permission from [43]. Copyright 2015 American Chemical Society.)

Figure 5.11c schematically illustrates a plausible mechanism responsible for the growth modes and the two possible overgrowth patterns for a cuboctahedral seed. Since the {100} facets of a Pd cuboctahedral seed are blocked by Br^- ions through chemisorption, as discussed in Chapter 3, the initially formed Pd atoms should be preferentially deposited onto the Pd{111} facets to generate kinks on these surfaces with a relatively higher surface energy that can serve as the active sites to promote the following atom deposition. However, the limited number of resultant Pd atoms supplied from the first few drops can only activate some of the eight {111} facets on each seed. Upon the subsequent introduction of more precursor solution, the deposition of the newly formed atoms will be largely limited to these activated sites, resulting in asymmetric growth for the cuboctahedral seed. Once deposited, there is a probability for the adatoms to migrate to adjacent {111} facets of the same seed through surface diffusion. As such, the initially deposited atoms at the kink sites will be able to migrate to other {111} facets through surface diffusion once the diffusion rate becomes comparable to the atom deposition rate, eventually generating active sites on all of the eight {111} facets.

Combined together, I believe that the growth mode (or pattern) of a seed is governed by the ratio between the atom deposition rate and the surface diffusion rate. In order to limit the number of activated sites on the seed and achieve asymmetric growth, the atom deposition rate needs to be greater than the surface diffusion rate (*i.e.*, $V_{deposition} > V_{diffusion}$). In contrast, if $V_{diffusion}$ is greater than $V_{deposition}$, all of the eight {111} facets can be activated to induce symmetric growth. When $V_{diffusion}$ and $V_{deposition}$ become comparable, the two growth modes will coexist and compete with each other. Consequently, some of the seeds will undergo symmetric growth while the other will follow asymmetric growth, resulting in a mixture of nanocrystals with different degrees of symmetry.

Based on the proposed mechanism, the correlation between growth mode and n_{low} can be understood from the following aspects. According to the pseudo-first-order rate law in Eq. (5.1), the reduction rate and thus the atom deposition rate are proportional to the

instantaneous number of precursor ions in the growth solution. Because n_t constantly varied in the range of n_{up} and n_{low} during a steady-state growth process, the corresponding atom deposition rate should oscillate between a maximum value and a minimum value. In this case, as long as the minimum value is above the threshold required for inducing asymmetric growth, the entire seed-mediated growth process will be exclusively locked in the asymmetric mode.

The Influence of Reaction Temperature on Surface Diffusion. Because surface diffusion is a thermally promoted process, it can be suppressed or enhanced by decreasing or increasing the reaction temperature, respectively [40]. Owing to the strong reducing power of AA, the reduction rate of the Pd(II) precursor and $V_{deposition}$ for a given precursor concentration over the temperature ranging from 20 to 80 ℃ can be assumed to be more or less on the same level as in the standard procedure (40 ℃). As such, manipulating the reaction temperature allows me to easily adjust the $V_{diffusion}$ involved in the growth process. Based on the proposed mechanism, any variation to $V_{diffusion}$ as caused by reaction temperature should provide another way to reverse the order of $V_{diffusion}$ and $V_{deposition}$ and thus to switch the growth mode.

I conducted an experiment by decreasing the reaction temperature to 20 ℃ while keeping other reaction parameters the same as in Figure 5.7a. Different from the perfect nanocubes obtained at 40 ℃ (see Figure 5.7a), elongated cubes with reduced symmetry became the major product, as shown in Figure 5.12a, when the temperature was reduced to 20 ℃, implying that the reduced $V_{diffusion}$ promoted the switching of growth mode. A similar transition was also observed in another experiment conducted under the same condition as in Figure 5.7d, except that the temperature was raised from 40 ℃ to 80 ℃. As expected, the significant increase in surface diffusion at 80 ℃ changed the order of rates to $V_{diffusion} > V_{deposition}$, thus switching the growth from an asymmetric mode to a symmetric mode, as confirmed by the formation of perfect nanocubes in Figure 5.12b. Taken together, these results suggest that, in addition to the manipulation of atom

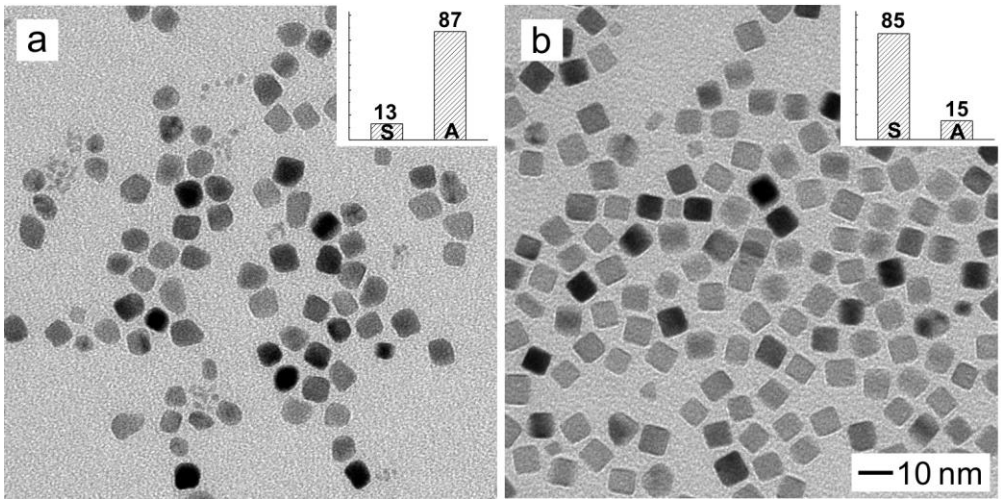

Figure 5.12. (a) TEM image of Pd nanocrystals prepared under the same conditions as in Figure 5.7a, except that the reaction temperature was set to 20 ℃. (b) TEM image of Pd nanocrystals prepared using the same conditions as in Figure 5.7d, except that the reaction temperature was set to 80 ℃. The inset in each TEM image shows a histogram distribution of the symmetric and asymmetric structures. (Reprinted with permission from [43]. Copyright 2015 American Chemical Society.)

deposition rate, the growth mode of a seed can also be controlled by varying the surface diffusion rate.

Extension from 4.5-nm Cuboctahedral Seeds to 10-nm Cubic Seeds. I also extended the strategy to another type of seeds by replacing the 4.5-nm cuboctahedrons used in the standard procedure with 10-nm Pd nanocubes as the seeds. It should be pointed out that the Pd cubic seeds with an average side length of 10 nm had a slightly reduced cubic shape as one of the directions was slightly elongated, as shown by the rectangular projection in the TEM image (Figure 5.13). For the purpose of simplicity, I refer to them as 10-nm cubic seeds. Based on the quantitative analysis, I conducted a set of experiments to demonstrate how the growth mode of such cubic seeds can be switched between symmetric and asymmetric modes. Figure 5.14a shows a TEM image of the

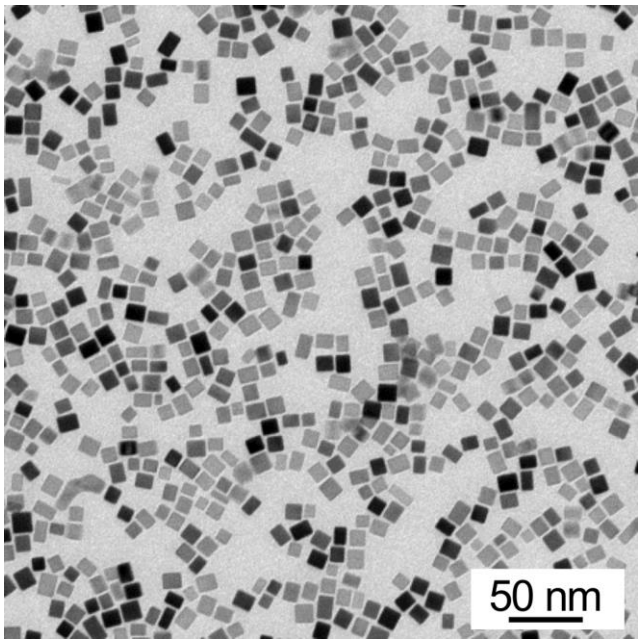

Figure 5.13. TEM image of Pd nanocubes with an average side length of 10 nm that served as seeds for the synthesis described in Figure 5.14. (Reprinted with permission from [43]. Copyright 2015 American Chemical Society.)

resultant Pd nanocrystals synthesized under the condition where the growth was dominated by asymmetric mode (*i.e.*, with $V_{deposition}>V_{diffusion}$). It can be seen that the cubic seeds underwent asymmetric growth and the newly formed Pd atoms were largely deposited on some of the corners on a cubic seed. Basically, the Pd atoms were supposed to be deposited on the eight corners of a cubic seed because their side {100} faces were blocked by Br^- ions. However, owing to the relatively small number of precursor ions, the initially formed Pd atoms were only deposited on a limited number of the corners upon the introduction of the first few drops. When the deposition rate was greater than the diffusion rate, the subsequently introduced atoms would be continuously deposited on the activated corners, leading to the formation of nanocrystals with a less symmetric structure relative to the cubic lattice. In comparison, when the duration of time between

adjacent drops was extended to enable the switching of growth from asymmetric to symmetric modes, enlarged Pd nanocubes were obtained as the product. As shown in Figure 5.14b, the cubic symmetry of nanocubes was more or less retained during the overgrowth. In this case, $V_{diffusion}$ became greater than $V_{deposition}$ and thus the initially deposited atoms could migrate to other corners and even the side {100} facets through surface diffusion, leading to symmetric growth.

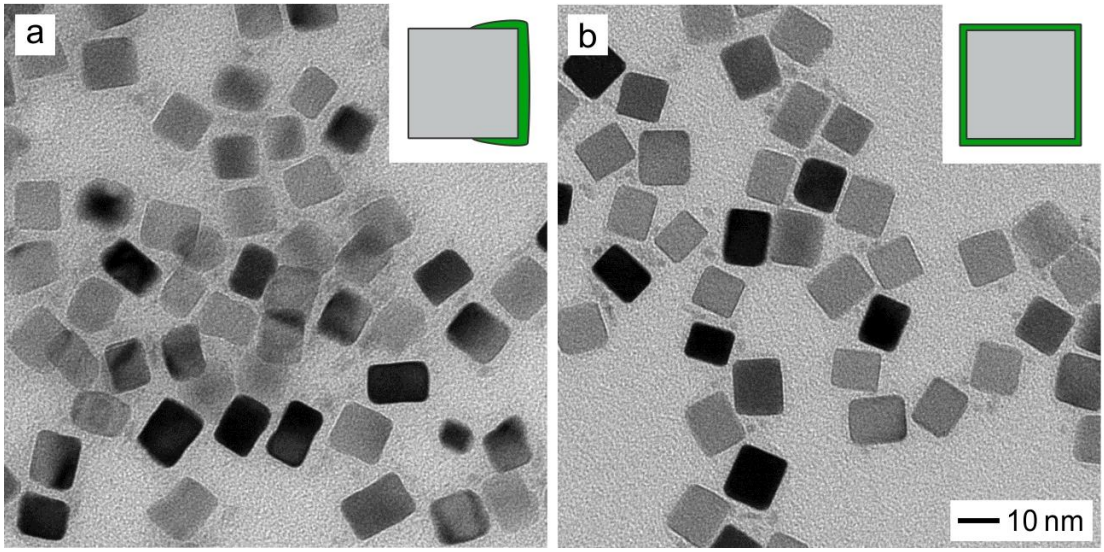

Figure 5.14. TEM images of the two distinctive types of Pd nanocrystals that were obtained *via* the overgrowth of 10-nm cubic seeds under (a) asymmetric and (b) symmetric modes, respectively. The number of Pd(II) precursor ions (n_0, normalized to the number of seeds) in each drop was 26 and the durations between adjacent drops (τ) were 1.8 s and 10.5 s for asymmetric and symmetric modes, respectively. The insets show 2-D projection models of the nanocrystals corresponding to the TEM images, where the grey and green colors represent the seed and the newly deposited Pd, respectively. (Reprinted with permission from [43]. Copyright 2015 American Chemical Society.)

5.3 Summary

In summary, I have quantitatively analyzed the symmetry breaking phenomenon involved in the seed-mediated growth of Pd nanocrystals under the dropwise introduction of a precursor solution with the use of a syringe pump. The dropwise approach allowed for a tight control over the reduction rate and thus the achievement of a steady state (as defined by the upper- and lower limits) for the number of precursor ions in the solution and a narrow range for the variations of atom deposition rate. Based on the reduction rate constant determined experimentally, I could predict the kinetics of a given synthesis, including the number of precursor ions in the growth solution as a function of time, as well as the upper- and lower limits of the steady state. Using Pd cuboctahedral seeds as an example, I have demonstrated the ability to switch the growth of a seed between symmetric and asymmetric modes by quantitatively tuning the experimental parameters such as the initial concentration of the precursor solution and the injection rate. My analysis suggested that the switching of the growth mode was determined by the lower-limit number of precursor ions in the steady state, which controlled the minimum rate responsible for the deposition of atoms onto a seed. When the first few drops of precursor solution were introduced, the resultant atoms could only be deposited on a limited number of equivalent sites on the surface of a seed to induce asymmetric growth if n_{low} was kept below a critical value. In order to maintain the asymmetric growth, the deposition of atoms needed to be kept at a faster pace than surface diffusion by controlling n_{low} above a value of eight for the Pd cuboctahedral seeds. In contrast, the seeds would take a symmetric growth mode when n_{low} was reduced to a level below eight by decreasing n_0 and/or extending τ. In this case, the migration of adatoms through surface diffusion could access other sites on the surface, switching the growth from asymmetric to symmetric mode. In addition to the manipulation of atom deposition rate, the growth mode of a seed could be switched by varying the reaction temperature to alter the surface diffusion rate. I believe that this work would greatly advance the mechanistic

understanding of the symmetry breaking phenomenon commonly involved in the seed-mediated growth of nanocrystals and provide a guideline for rational design and synthesis of nanocrystals with less symmetric shapes than a cubic lattice.

5.4 Experimental Methods

Measurement of the Kinetic Parameters. The rate constant was derived by analyzing the concentration of Pd(II) ions remaining in the reaction solution at different time points through ICP-MS. Specifically, 2.0 mL of an aqueous solution containing 100.0 mg of AA and 1.2 mg of KBr was mixed in a 20 mL glass vial and heated to 40 ℃ in an oil bath for 20 min under magnetic stirring. Next, 1.0 mL of an aqueous Na_2PdCl_4 solution (1.0 mg/mL) was quickly injected into the vial in one shot. An aliquot of 0.1 mL was sampled from the reaction solution at different time points using a glass pipette and immediately injected into 0.9 mL of aqueous KBr solution (500 mg/mL) to quench the reduction reaction. The solution was then centrifuged at 55,000 rpm for 40 min to precipitate out all the Pd nanocrystals, leaving behind Pd(II) ions in the supernatant. Subsequently, the supernatant was collected and further diluted with 1% (v/v) aqueous HNO_3 solution to a level of 100 ppb for ICP-MS analysis. The concentrations of Pd(II) ions obtained at different time points were then used to determine the rate constant by performing a linear regression fit to the plot of ln[Pd(II)] *versus* reaction time, with the slope of the regression line equal to $-k$. When the temperature was fixed, the rate constant could be used to calculate the instantaneous concentrations of the Pd(II) ions as a function of reaction time for all the seed-mediated growth experiments conducted in the present work.

Synthesis of the 4.5-nm Pd Cuboctahedral Seeds. The Pd cuboctahedrons to be used as seeds for overgrowth were prepared using a recently reported protocol based on polyol reduction [39]. In a typical synthesis, 30 mg of PVP and 2.0 mL of EG were mixed in a 20 mL glass vial, and the mixture was heated to 160 ℃ under magnetic

stirring. Next, 15.5 mg of Na_2PdCl_4 was dissolved in 1.0 mL of EG and added into the above mixture in one shot using a pipette. The reaction was allowed to proceed for 2 h. After centrifugation at 55,000 rpm and washing with ethanol and water three times, the Pd cuboctahedral seeds were re-dispersed in 3 mL water.

Synthesis of the 10-nm Pd Cubic Seeds. The 10-nm Pd cubic seeds were prepared using a previously reported protocol [42]. In a typical synthesis, 8 mL aqueous solution containing 105 mg of PVP, 60 mg of AA, and 300 mg of KBr was added into a 20 mL glass vial and heated at 80 ℃ for 5 min. Next, 3 mL aqueous solution containing 57 mg of Na_2PdCl_4 was added in one shot under magnetic stirring. The reaction was allowed to proceed at 80 ℃ for 3 h. The product was collected by centrifugation at 16,000 rpm, washed with water three times, and re-dispersed in 11 mL water.

Seed-mediated Growth of Pd Nanocrystals. Table 5.1 shows a summary of the parameters used for the syntheses of Pd nanocrystals by seed-mediated growth. In a standard synthesis, an aqueous solution containing Na_2PdCl_4 (1.5 mg) and KBr (0.4 mg/mL) and another aqueous solution containing KBr (0.4 mg/mL) and AA (66.7 mg/mL) were introduced simultaneously using two syringe pumps into 3 mL of the growth solution - an aqueous suspension containing the seeds (0.1 mL for the 4.5-nm cuboctahedral seeds or 0.2 mL for the 10-nm cubic seeds), 100 mg of AA, 10 mg of PVP, and 1.2 mg of KBr in a 50 mL two-neck, round flask heated at 40 ℃ under magnetic stirring. For each drop of the precursor solution generated using a syringe pump at an injection rate of 30 mL/h, it had a volume of 0.015 mL. The concentration of the precursor solution was varied between syntheses to access a broad range of values for the initial number of the Pd(II) ions contained in each drop (see Table 5.1). After a specific amount of the precursor solution had been introduced, the growth was allowed to proceed for another 5 min and the product was then collected by centrifugation at 13,200 rpm, followed by washing with water three times.

Table 5.1. Summary of the parameters used for the syntheses of Pd nanocrystals *via* seed-mediated growth

n_0	τ (s)	Cuboctahedral seeds (μL)	Cubic seeds (μL)	[Na_2PdCl_4] (mg/mL)	$Na_2PdCl_{4(aq)}$ vol. (mL)	Injection rate (mL/h)	Results (Figure)
4.7	0.45	100	-	0.05	30.0	120.0	5.10b
4.7	0.9	100	-	0.05	30.0	60.0	5.10a
4.7	1.8	100	-	0.05	30.0	30.0	5.7a
11.7	1.8	100	-	0.125	12.0	30.0	5.7b
23.5	1.8	100	-	0.25	6.0	30.0	5.7c
23.5	3.6	100	-	0.25	6.0	15.0	5.10d
23.5	10.5	100	-	0.25	6.0	5.0	5.10e
70.5	1.8	100	-	0.75	2.0	30.0	5.7d
26.2	1.8	-	200	0.02	50.0	30.0	5.14a
26.2	10.5	-	200	0.02	50.0	5.0	5.14b

Analysis of the Growth Mode. The classification of the growth mode is based on the degree of symmetry for the resultant Pd nanocrystals. In analyzing the Pd nanocrystals by TEM imaging, I defined the perfect nanocubes with O_h symmetry as the products of *symmetric growth*. In comparison, those nanocrystals with elongation along one or more directions (*e.g.*, nanobars) and thus reduction in symmetry relative to a perfect cube were defined as the products of *asymmetric growth*. Specifically, the aspect ratio (length divided by width) of each particle was derived from TEM images. I then defined an aspect ratio of 1.1 as the borderline between *symmetric* and *asymmetric* growth. The histogram distributions of symmetric and asymmetric structures were obtained by counting 150 single-crystal particles in each sample, with the twinned particles being excluded from the analysis. It should be noted that TEM image is a 2-D projection of particle morphology and may lead to a potential underestimate of the number of asymmetric particles.

Characterizations. TEM images were taken using a Hitachi HT7700 microscope operated at 120 kV. The sample for TEM analysis was prepared by drying a drop of the nanocrystal suspension on a carbon-coated copper grid under ambient conditions. The concentration of Pd(II) precursor in the reaction solution was measured using an inductively coupled plasma mass spectrometer (NexION 300Q, Perkin-Elmer).

5.5 Notes to Chapter 5

Part of this chapter is adapted from the paper "Toward a quantitative understanding of symmetry reduction involved in the seed-mediated growth of palladium nanocrystals" published in *Journal of the American Chemical Society* [43].

5.6 References

[1] L Ahmadi, T. S.; Wang, Z. L.; Green, T. C.; Henglein, A.; El-Sayed, M. A. *Science*

1996, *272*, 1924−1926.

[2] Park, J.; Joo, J.; Kwon, S. G.; Jang, Y.; Hyeon, T. *Angew. Chem., Int. Ed.* **2007**, *46*, 4630−4660.

[3] Tao, A. R.; Habas, S.; Yang, P. *Small* **2008**, *3*, 310−325.

[4] Xia, Y.; Xiong, Y.; Lim, B.; Skrabalak, S. E. *Angew. Chem., Int. Ed.* **2009**, *48*, 60−103.

[5] Yang, X.; Yang, M.; Pang, B.; Vara, M.; Xia, Y. *Chem. Rev.* **2015**, DOI: 10.1021/acs.chemrev.5b00193.

[6] Dreaden, E. C.; Alkilany, A. M.; Huang, X., Murphy; C. J.; El-Sayed, M. A. *Chem. Soc. Rev.* **2012**, *41*, 2740−2779.

[7] Huang, X.; Neretina, S.; El-Sayed, M. A. *Adv. Mater.* **2009**, *21*, 4880−4910.

[8] Chen, H.; Shao, L.; Li, Q.; Wang, J. *Chem. Soc. Rev.* **2013**, *42*, 2679−2724.

[9] Sun, Y.; Gates, B.; Mayers, B.; Xia, Y., *Nano Lett.* **2002**, *2*, 165−168.

[10] De, S.; Higgins, T. M.; Lyons, P. E.; Doherty, E. M.; Nirmalraj, P. N.; Blau, W. J.; Boland, J. J.; Coleman, J. N. *ACS Nano* **2009**, *3*, 1767−1774.

[11] Sun, Y. *Nanoscale* **2010**, *2*, 1626−1642.

[12] Rycenga, M.; Cobley, C. M.; Zeng, J.; Li, W.; Moran, C. H.; Zhang, Q.; Qin, D.; Xia, Y. *Chem. Rev.* **2011**, *111*, 3669−3712.

[13] Zhou, W.; Wu, J.; Yang, H. *Nano Lett.* **2013**, *13*, 2870−2874.

[14] Wang, X.; Choi, S.-I.; Roling, L. T.; Luo, M.; Ma, C.; Zhang, L.; Chi, M.; Liu, J.; Xie, Z.; Herron, J. A.; Mavrikakis, M.; Xia, Y. *Nat. Commun.* **2015**, *6*, 7594.

[15] Kong, X. Y.; Ding, Y.; Yang, R.; Wang, Z. L. *Science* **2004**, *303*, 1348−1351.

[16] Wang, Z. L.; Kong, X. Y.; Zuo, J. M. *Phys. Rev. Lett.* **2003**, *91*, 185502.

[17] Nikoobakht, B.; El-Sayed, M. A. *Chem. Mater.* **2003**, *15*, 1957−1962.

[18] Pérez-Juste, J.; Liz-Marzán, L. M.; Carnie, S.; Chan, D. Y. C.; Mulvaney, P. *Adv. Funct. Mater.* **2004**, *14*, 571−579.

[19] Orendorff, C. J.; Murphy, C. J. *J. Phys. Chem. B* **2006**, *110*, 3990−3994.

[20] Xiong, Y.; Cai, H.; Wiley, B. J.; Wang, J.; Kim, M. J.; Xia, Y. *J. Am. Chem. Soc.* **2007**, *129*, 3665−3675.

[21] Sun, Y.; Zhang, L.; Zhou, H.; Zhu, Y.; Sutter, E.; Ji, Y.; Rafailovich, M. H.; Sokolov, J. C. *Chem. Mater.* **2007**, *19*, 2065−2070.

[22] Wiley, B. J.; Chen, Y.; McLellan, J. M.; Xiong, Y.; Li, Z.-Y.; Ginger, D.; Xia, Y. *Nano Lett.* **2007**, *7*, 1032−1036.

[23] Zhang, Q.; Moran, C. H.; Xia, X.; Rycenga, M.; Li, N.; Xia, Y. *Langmuir* **2012**, *28*, 9047−9054.

[24] Zeng, J.; Zhu, C.; Tao, J.; Jin, M.; Zhang, H.; Li, Z.-Y.; Zhu, Y.; Xia, Y. *Angew. Chem., Int. Ed.* **2012**, *51*, 2354−2358.

[25] Zhu, C.; Zeng, J.; Tao, J.; Johnson, M. C.; Schmidt-Krey, I.; Blubaugh, L.; Zhu, Y.; Gu, Z.; Xia, Y. *J. Am. Chem. Soc.* **2012**, *134*, 15822−15831.

[26] Xia, X.; Xia, Y. *Nano Lett.* **2012**, *12*, 6038−6042.

[27] Habas, S. E.; Lee, H.; Radmilovic, V.; Somorjai, G. A.; Yang, P. *Nat. Mater.* **2007**, *6*, 692−697.

[28] Zhang, H.; Li, W.; Jin, M.; Zeng, J.; Yu, T.; Yang, D.; Xia, Y. *Nano Lett.* **2011**, *11*, 898−903.

[29] Wang, D.; Li, Y. *Adv. Mater.* **2011**, *23*, 1044−1060.

[30] Langille, M. R.; Zhang, J.; Personick, M. L.; Li, S.; Mirkin, C. A. *Science* **2012**, *337*, 954−957.

[31] Luty-Błocho, M.; Pacławski, K.; Wojnicki, M.; Fitzner, K. *Inorg. Chim. Acta* **2013**, *395*, 189−196.

[32] Wang, Y.; Peng, H.-C.; Liu, J.; Huang, C. Z.; Xia, Y. *Nano Lett.* **2015**, *15*, 1445−1450.

[33] Feldberg, S.; Klotz, P.; Newman, L. *Inorg. Chem.* **1972**, *11*, 2860−2865.

[34] Dean, J. A. *Lange's Chemistry Handbook*, 15th ed.; McGraw-Hill Professional: New York, 1998.

[35] Timoshkin, A. Y.; Kudrev, A. G. *Russ. J. Inorg. Chem.* **2012**, *57*, 1362−1970.

[36] Niu, W.; Zhang, L., Xu, G. *ACS Nano* **2010**, *4*, 1987−1996.

[37] Jin, M.; Zhang, H.; Xie, Z.; Xia, Y. *Energy Environ. Sci.* **2012**, *5*, 6352−6357.

[38] Gao, C.; Vuong, J.; Zhang, Q.; Liu, Y.; Yin, Y. *Nanoscale* **2012**, *4*, 2875−2878.

[39] Wang, Y.; Xie, S.; Liu, J.; Park, J.; Huang, C. Z.; Xia, Y. *Nano Lett.* **2013**, *13*, 2276−2281.

[40] Xia, X.; Xie, S.; Liu, M.; Peng, H.-C.; Lu, N.; Wang, J.; Kim, M. J.; Xia, Y. *Proc. Natl. Acad. Sci. U.S.A.* **2013**, *110*, 6669−6673.

[41] Peng, H.-C.; Xie, S.; Park, J.; Xia, X.; Xia, Y. *J. Am. Chem. Soc.* **2013**, *135*, 3780−3783.

[42] Jin, M.; Liu, H.; Zhang, H.; Xie, Z.; Liu, J.; Xia, Y. *Nano Res.* **2011**, *4*, 83−91.

[43] Peng, H.-C.; Park, J.; Zhang, L.; Xia, Y. *J. Am. Chem. Soc.* **2015**, *137*, 6673−6652.

CHAPTER 6

CONCLUSIONS AND FUTURE DIRECTIONS

6.1 Conclusions

This dissertation provides a quantitative understanding of the shape-controlled synthesis of colloidal noble-metal nanocrystals, with a focus on the thermodynamic and kinetic factors responsible for the shape evolution of nanocrystals. I started with a quantitative analysis of the role played by Br^- ions in the synthesis of Pd nanocrystals. The strategy was based on a combination of XPS and ICP-MS analysis to acquire both the elemental and chemical information about the Pd nanocrystals. According to the ratio of Br^- ions to Pd atoms as obtained from ICP-MS analysis, the Br^- ions were found to chemisorb onto Pd{100} facets selectively with a coverage density of *ca*. 10 ions/nm^2 for Pd nanocubes with three different sizes. The chemisorbed Br^- ions could be removed from the surface via desorption at an elevated temperature under reductive conditions. The adsorbed Br^- ions could also be released from the surface by decreasing the proportion of {100} facets during the growth of Pd nanocubes. Most significantly, I was able to estimate the minimum amount of Br^- ions needed for capping the entire surface of Pd nanocubes with a certain size in advance during the design of an experiment. With the introduction of an adequate amount of Br^- ions, well-defined Pd nanocubes enclosed by {100} were obtained as the thermodynamic product.

To understand the role of a surface capping agent in determining the deposition probability of atoms and thus the growth pattern of a seed, I further conducted a set of experiments on seed-mediated growth by using Pd nanocubes with or without chemisorbed Br^- ions as the seeds. From the collision model that has been established in surface science, the deposition probability of atoms on the surface and thus the distinctive growth patterns of the seeds in the presence or absence of chemisorbed Br^- ions could be

readily explained. The deposition of atoms would only occur at the corners and edges of a cubic seed when its {100} side facets were passivated by Br^- ions. In comparison, the atoms were found to be randomly deposited on the entire surface of a seed in the absence of chemisorbed Br^- ions.

Complementary to thermodynamic control, kinetic control provides a route to the preparation of nanocrystals with shapes deviating from the thermodynamic product by manipulating the reaction kinetics. With the polyol synthesis of Pd nanocrystals as an example, I discovered that the initial reduction rate could serve as a quantitative knob for controlling the internal structure of seeds and thus the shape of nanocrystals. Seeds with a specific internal structure including single-crystal, multiply twinned, and stacking fault-lined could all be prepared as almost pure samples by controlling the initial reduction rate, which could be conveniently manipulated by adjusting a set of experimental parameters, including the reaction temperature, types of precursor and reducing agent, as well as their concentrations. From the kinetic parameters of a synthesis obtained from spectroscopic measurement, including rate constant and activation energy, I quantitatively determined the range of initial reduction rates corresponding to the formation of seeds with a specific internal structure.

I also quantitatively analyzed the symmetry breaking phenomenon involved in the seed-mediated growth of Pd nanocrystals under the dropwise addition of a precursor solution. The dropwise approach allows for the formation of a steady state for the number of precursor ions in the growth solution, which only oscillates in a narrow range defined by experimental parameters such as the initial concentration of precursor solution and the injection rate. I demonstrated that the growth mode of a seed can be deterministically controlled by tuning these parameters to quantitatively manipulate the reaction kinetics and thus the lower and upper limits that define the steady state. There exists a correlation between the growth mode and the lower limit of precursor ions, a factor that determines the minimum value of atom deposition rate in the steady state. In order to induce and

sustain the asymmetric growth mode, the atom deposition needs to be kept at a rate slow enough to limit the number of initial nucleation sites on a seed but fast enough to ensure that the deposition is faster than surface diffusion during the entire growth process.

My research has greatly advanced the understanding of the shape-controlled synthesis of nanocrystals on a quantitative basis, thus representing a major step forward toward the rational design and deterministic synthesis of colloidal noble-metal nanocrystals.

6.2 Future Directions

The quantitative understanding achieved in my dissertation work about the nucleation and growth of colloidal noble-metal nanocrystals lays a foundation for the rational design and deterministic synthesis of nanocrystals with desired and controlled internal structures, shapes, and properties. In order to reach the ultimate goal, further development and extension of the current synthetic and characterization strategies still need to be made.

One of the major remaining challenges in the thermodynamically controlled synthesis of colloidal noble-metal nanocrystals is the lack of capping agents capable of preferentially stabilizing high-index facets. Because of their high densities of low-coordination sites, high-index facets are generally considered to have better performance in many catalytic reactions [1−5]. In this regard, a facile protocol for preparing colloidal metal nanocrystals enclosed by high-index facets would be highly desirable. Crystallographic planes with high Miller indices are not flat on an atomic scale. They are typically comprised of narrow, low-index planes separated by steps of one atomic high. Some of the capping agents developed for low-index facets may still be applicable to high-index facets, as long as the atomic steps can be somehow stabilized. Future effort needs to be directed toward the identification of capping agents for high-index facets based on a combination of both experimental screening and computational modeling.

Another challenge in this field is the frequent lack of agreement between the data

obtained by computational simulations and experimental observations. Integration of additional physical details, such as the diffusion of atoms along the surface of a nanocrystal and the collisions between solvent molecules and seeds, would provide a far more truthful picture of the growth dynamics and pathway. Accurate simulations would allow one to avoid trial-and-error approaches that are currently necessary to produce a holistic understanding of a synthesis.

The nucleation process also requires an extensive study to unveil the underlying mechanisms. In particular, there is very little knowledge of the exact mechanism responsible for the homogeneous nucleation step in a one-pot synthesis. As such, it remains a significant challenge to elucidate the explicit roles played by various thermodynamic and kinetic factors in a one-pot synthesis. In addition, it is still unclear about the exact pathway of heterogeneous nucleation in a seed-mediated synthesis. The generally accepted argument is that the metal precursor is firstly reduced into atoms, which are then deposited onto the seeds. Alternatively, it is also possible that the precursor compounds (or ions) adsorb onto the seed surface and then reduced into atoms [6, 7]. The challenges in investigating the corresponding mechanisms are mainly imposed by the shortage of instruments capable of capturing, identifying, and monitoring the intermediate species instantaneously during nucleation with satisfying resolution. In this regard, alternative approaches based on computational simulations offer an opportunity to decipher the secret in the black box of nucleation.

Another area that deserves closer study is a systematic analysis of the various pathways for the symmetry breaking phenomenon. Currently, the developed mechanisms mostly depend on reconciling chemical and physical principles with the finally collected nanocrystal products. Direct experimental observations gathered during nanocrystal growth, especially at the very early stage when asymmetric growth is initially triggered, would provide concrete evidence for, or against, the proposed mechanisms. However, due to the involvement of a solution phase and the Brownian motion of a growing seed, it is

extremely difficult to directly follow the deposition of atoms on a seed and their subsequent diffusion in real space despite the remarkable advancement in *in situ* electron microscopy [8−10] and synchrotron diffraction [11, 12]. Further advancements in characterization tools are needed to make this approach robust enough for widespread use. An alternative approaches based on computational simulations may also greatly advance the understanding of this subject.

6.3 References

[1] Zhang, H.; Jin, M.; Xia, Y. *Angew. Chem., Int. Ed.* **2012**, *51*, 7656−7673.

[2] Ma, Y.; Kuang, Q.; Jiang, Z.; Xie, Z.; Huang, R.; Zheng, L. *Angew. Chem., Int. Ed.* **2008**, *47*, 8901−8904.

[3] Huang, Z.; Zhao, Z.; Fan, J.; Tan, Y.; Zheng, N. *J. Am. Chem. Soc.* **2011**, *133*, 4718−4721.

[4] Tian, N.; Zhou, Z.-Y.; Yu, N.-F.; Wang, L.-Y.; Sun, S.-G. *J. Am. Chem. Soc.* **2010**, *133*, 7580−7581.

[5] DeSantis, C. J.; Poverly, A. A.; Peters, D. G.; Skrabalak, S. E. *Nano Lett.* **2011**, *11*, 2164−2168.

[6] Xia, Y.; Xiong, Y.; Lim, B.; Skrabalak, S. E. *Angew. Chem., Int. Ed.* **2009**, *48*, 60−103.

[7] Tao, A. R.; Habas, S.; Yang, P. *Small* **2008**, *4*, 310−325.

[8] Zheng, H.; Smith, R. K.; Jun, Y.-W.; Kisielowski, C.; Dahmen, U.; Alivisatos, A. P. *Science* **2009**, *324*, 1309−1312.

[9] Sun, Y.; Wang, Y. *Nano Lett.* **2011**, *11*, 4386−4392.

[10] Sutter, E.; Jungjohann, K.; Bliznakov, S.; Courty, A.; Maisonhaute, E.; Tenney, S.; Sutter, P. *Nat. Commun.* **2014**, *5*, 4946.

[11] Natter, H.; Schmelzer, M.; Löffler, M.-S.; Krill, C. E.; Fitch, A.; Hempelmann, R. *J.*

Phys. Chem. B **2000**, *104*, 2467−2476.

[12] Gardea-Torresdey, J. L.; Parson, J. G.; Gomez, E.; Peralta-Videa, J.; Troiani, H. E.; Santiago, P.; Yacaman, M. J. *Nano Lett.* **2002**, *2*, 397−401.